Calcium isotopes in high-temperature terrestrial processes

Michael Antonelli, Justin Simon

Calcium isotopes in high-temperature terrestrial processes

Authors: Michael A. Antonelli[a,1,*], Justin I. Simon[b]

Affiliations: [a]Institut de Physique du Globe de Paris, University de Paris, 1 rue Jussieu, 75005 Paris, France. [b]Center for Isotope Cosmochemistry and Geochronology, Astromaterials Research & Exploration Science, NASA Johnson Space Center, Houston, USA. [1]Corresponding author. E-mail address: mantonelli@berkeley.edu (M.A. Antonelli). [*]Current address: Department of Earth Sciences, Institute of Geochemistry and Petrology, ETH Zurich, Clausiusstrasse 25, CH-8092, Zurich, Switzerland.

Abstract: This chapter explores the growing body of stable and radiogenic Ca isotope measurements in high temperature terrestrial materials and covers the emerging applications for Ca isotope variability in igneous and metamorphic rocks and minerals. Calcium isotope fractionation at high temperature has been found to lead to larger effects than initially theorized, sometimes even exceeding those found in low temperature near-surface environments, yet many of the underlying fractionation mechanisms still remain poorly understood. Igneous whole-rocks span a $\delta^{44}Ca$ range of ~2‰ (-0.9 to +0.9‰, relative to bulk-silicate Earth) and their constituent minerals have a range of ~2.5‰ (-1.2 to +1.3‰). Metamorphic whole rocks span a larger $\delta^{44}Ca$ range of ~6‰ (-2.5 to +3.3‰), while metamorphic mineral separates span ~8‰ (-2.2 to +5.8‰). Observed Ca isotope variations can stem from a variety of sources including: (i) isolation of isotopically-distinct mineral components, such as during melting or crystallization, (ii) mixing of isotopically-distinct reservoirs into magmatic sources, such as during mantle metasomatism or

assimilation of distinct crustal components, and (iii) isotopic rate differences (kinetic effects) during melting, crystallization, transport, and metamorphism, which are often governed by Ca diffusion. The emerging picture is that Ca isotopes are sensitive to a large number of high-temperature processes and can be used to understand the evolution of crust and mantle reservoirs, along with mechanisms leading to the formation of igneous, metamorphic, and hydrothermal rocks and minerals through geologic time.

Table of Contents

1. Introduction

Over the last two decades it has become increasingly clear that Ca isotopes can be used to trace a wide variety of high-temperature solid Earth processes. Ca isotopes have been used to gain insight into diverse topics relevant to high-temperature geochemistry, including crustal recycling and contamination, rates and mechanisms of metamorphic and igneous processes (such as mantle metasomatism, metamorphic mineral paragenesis, and igneous crystal growth), and Ca transport in otherwise inaccessible regions of the solid Earth. The increasing body of work that has investigated Ca isotope fractionation has also yielded fundamental information on the behavior of redox-insensitive cations in high-temperature systems. In this fashion, understanding Ca isotope fractionation serves as a baseline for understanding the behavior of more complex, redox-sensitive, isotopic systems that undergo changes in oxidation-state (*e.g.* Fe, Cr, S, Ce), but which must also succumb to similar fractionation effects during chemical reaction and diffusive transport.

There are six stable isotopes of calcium with a total relative mass range of ~20%: ^{40}Ca (96.94%), ^{42}Ca (0.65%), ^{43}Ca (0.14%), ^{44}Ca (2.09%), ^{46}Ca (~40 ppm), and ^{48}Ca (0.19%). Due to the higher abundances of ^{40}Ca and ^{44}Ca, stable Ca isotope variations are commonly reported as $\delta^{44}Ca$:

$$\delta^{44}Ca = \frac{\left(^{44}Ca/_{40}Ca\right)_{sample}}{\left(^{44}Ca/_{40}Ca\right)_{standard}} - 1 \qquad \text{(Eq.}$$

1)

This formalism results in positive $\delta^{44}Ca$ values when a sample is enriched in ^{44}Ca relative to a known standard, and negative values when a sample is depleted in ^{44}Ca. It is important to note, however, that the most abundant isotope, ^{40}Ca, can also be produced by the radioactive decay of

76 ^{40}K (half-life of ~1.25 Ga). Stable Ca isotope variations (δ^{44}Ca) must therefore be corrected for

77 the potential radiogenic ingrowth of ^{40}Ca in analyzed samples. This is commonly accomplished

78 by either measuring ^{44}Ca/^{42}Ca and then converting to ^{44}Ca/^{40}Ca by multiplying by 2.05 (Fantle

79 and Tipper, 2014), which is the canonical mass-law for kinetic Ca isotope fractionation (the

80 equilibrium mass law is ~2.10), or by measuring ^{44}Ca/^{40}Ca directly and then correcting for

81 radiogenic ^{40}Ca ingrowth using additional (unspiked) measurements. Reporting Ca isotope data

82 as $\delta^{44/42}$Ca instead of δ^{44}Ca would serve to separate stable from radiogenic isotope variations, but

83 double-spike techniques used to correct for instrumental mass fractionation (IMF) during thermal

84 ionization mass spectrometry (TIMS) often include ^{42}Ca and ^{48}Ca (or ^{43}Ca) spikes. Although

85 ^{43}Ca-^{46}Ca double spikes would be the most useful to explore variations in ^{40}Ca, ^{42}Ca, ^{44}Ca, and

86 ^{48}Ca simultaneously, the rarity of these isotopes greatly increases the cost of analysis, rendering

87 this combination much less common.

88 The application of δ^{44}Ca measurements to high-temperature systems began to flourish starting

89 with the observation that large δ^{44}Ca fractionations (up to ~10‰) were possible during chemical

90 diffusion in silicate liquids (Richter et al., 2003, 1999). For the next decade, research focused

91 mainly on exploring the various mechanisms responsible for diffusive Ca isotope fractionations

92 in silicate liquids, which were shown to depend on: (i) the magnitude of Ca concentration

93 gradients, (ii) the direction and magnitude of chemical gradients for other species, relative to

94 those of Ca, (iii) the strength of imposed temperature gradients, and (iv) the degree of melt

95 polymerization (F. Huang et al., 2010; Richter et al., 2009, 2003, 1999; Watkins et al., 2017,

96 2014, 2011, 2009).

97 The first δ^{44}Ca measurements in natural igneous rocks served as a baseline for ecological studies

98 [where food-chain δ^{44}Ca variations were found to depend on trophic levels (Skulan et al., 1997)],

99 and were not further explored until the late 2000's (Amini et al., 2009; Jochum et al., 2006;

100 Simon and DePaolo, 2010; Wombacher et al., 2009). In the last ten years, however, there have

101 been an increasing number of Ca isotope studies in natural high-temperature rocks and minerals,

102 partially motivated by the initial observation that coexisting orthopyroxene and clinopyroxene in

103 mantle xenoliths have significant $\delta^{44}Ca$ variations (up to ~1 ‰) and that $\delta^{44}Ca$ variations in

104 Hawaiian basalts could be related to subduction of carbonates with low $\delta^{44}Ca$ (Huang et al.,

105 2011; S. Huang et al., 2010). Subsequent studies have mainly focused on understanding $\delta^{44}Ca$

106 variations in mantle whole-rock samples (and rock standards) but have also explored $\delta^{44}Ca$

107 variations in whole-rocks and mineral separates from mafic, silicic, metamorphic, and

108 hydrothermal samples. These studies highlight the potential for Ca isotopes to be used as proxies

109 for mantle metasomatism, carbonate recycling, crustal contamination, Ca diffusion

110 rates/mechanisms in the continental crust, partial melting, equilibration temperature,

111 metamorphic mineral paragenesis, K-loss during anatexis and high-temperature metamorphism,

112 mineral precipitation rates in hydrothermal systems, and crystal growth rates in magmatic

113 systems. Here, we present an overview of available Ca isotope data in high-temperature samples

114 and explore the potential strengths and limitations of their use as constraints for natural high-

115 temperature processes.

116 **1.1. Ca isotope nomenclature**

117 Similar to many other stable isotope systems, Ca isotope values are generally reported relative to

118 a known standard in lowercase delta-notation ($\delta^{44}Ca$, Eq. 1) and followed by a per mil symbol

119 (‰), which indicates that the value has been multiplied by 1,000. Although it is redundant (and

120 technically incorrect) to include both a per mil symbol after reported values and a factor of 1,000

121 in the definition of $\delta^{44}Ca$, many authors and peer-reviewers still push for both, which

122   unfortunately renders isotope nomenclature more complex than it needs to be, especially for

123   students and scientists outside of our community. IUPAC has suggested to either (i) remove the

124   factor of 1,000 from the definition (as we have done in Equation 1) if using a per mil symbol

125   after reported values, or (ii) to omit the per mil symbol after values, if including a factor of

126   1,000 in the definition of $\delta^{44}Ca$ (Coplen, 2011). Other than common delta-notation, formalisms

127   typically used in the isotope community include (i) epsilon (ε) notation, which reports deviations

128   from the standard in parts per ten-thousand (commonly used for radiogenic ^{40}Ca variations), and

129   (ii) mu (μ) notation, which reports values as parts per million (often used for particularly small

130   variations).

131   In this review, we have chosen to include either per mil symbols (‰, for delta-notation) or

132   indicate parts-per-million (ppm, for μ-notation) after reported values, in order to omit the factors

133   of 1,000 and 1,000,000 from our definitions. For epsilon notation, we could potentially omit the

134   factor of 10,000 from our definition of ε_{Ca} by reporting values with a per myriad (‱) or parts-

135   per-ten-thousand (pptt) symbol, but to our knowledge, neither have been previously used. We

136   therefore include the multiplicative factor in our definition of ε_{Ca} (in Section 7) and do not use

137   any symbols after reporting ε-values. When comparing two related samples, isotopic differences

138   are generally reported using capital delta notation (*e.g.* $\Delta^{44}Ca_{a-b,} = \delta^{44}Ca_a - \delta^{44}Ca_b$, for samples a

139   and b), which can also be used to report deviations from an expected value [*e.g.* $\Delta^{48}Ca' =$

140      $\mu^{48}Ca_{measured} - \mu^{48}Ca_{equilibrium}$]. All these notations, however, are further introduced and discussed

141   in the most pertinent sections of this review.

142   **2. Observations of mass-dependent Ca isotope variations in igneous and metamorphic**

143   **rocks**

144   Since the first measurements of stable Ca isotope distributions in volcanic rocks, there have been

145   over 60 studies measuring $\delta^{44}Ca$ in natural high-temperature samples. One of the common goals

146   for many of these studies is the definition of $\delta^{44}Ca$ for the bulk silicate Earth (BSE). Although

147   analytical uncertainties and potential sample-biases initially hindered the precise definition of

148   BSE $\delta^{44}Ca$, a growing number of studies based on mantle rocks and meteorites are converging

149   towards a relatively well-constrained $\delta^{44}Ca$ value of $+0.95‰$ relative to carbonate standard

150   SRM915a, which is approximately the same as initially estimated from early studies. The use of

151   BSE as a reference value for Ca isotope measurements [which comes from the first exploration

152   of stable Ca isotope variations in terrestrial/biological materials (Skulan et al., 1997)], however,

153   predates the use of SRM915a. Nevertheless, the analyzed igneous rocks and minerals in this

154   early study gave the same values (within uncertainty, ~3-4 times larger than today) as the most

155   up-to-date high-precision estimates *e.g.* (Kang et al., 2019). In order to best illustrate potential

156   differences and complementarity between Earth reservoirs, therefore, $\delta^{44}Ca$ data from UC-

157   Berkeley have since been reported relative to an estimated BSE value (which has corresponded

158   to $+0.95‰$ relative to SRM915a for the last decade, but was slightly higher in earlier studies).

159   More than four different reference materials, however, are commonly used to define $\delta^{44}Ca$

160   (including SRM915a, SRM915b, BSE, and modern seawater) and they must be converted to a

161   common scale in order to allow for comparison between studies. Although SRM915a is no

162   longer commercially available and seawater $\delta^{44}Ca$ is, on average, controlled by the extent of

163   carbonate precipitation in the oceans (which may have changed over geologic time) and can also

164   vary based on collection depth and location (Chakrabarti et al., 2018), it is hard to argue for the

165   use of one standard over another. In Table 1, we present inter-conversion factors for commonly

166   used Ca isotope standards. To use these factors and report Ca isotope data to different reference

167 materials, it is sufficient to add the listed value from Table 1 to the measured delta value [*e.g.*

168 $\delta^{44}Ca_{BSE} = \delta^{44}Ca_{915a} + (-0.95)$]. Note that for very large values, it is more accurate to recast the

169 delta values into isotopic ratios and then re-calculate new delta values using the $^{44}Ca/^{40}Ca$ of

170 desired reference materials, but terrestrial Ca isotope fractionations are not generally large

171 enough to warrant this additional step. To convert $\delta^{44/42}Ca$ values to $\delta^{44}Ca$, one can simply

172 multiply by 2.05 (or divide $\delta^{44}Ca$ by 2.05 to arrive at $\delta^{44/42}Ca$). In this study, we chose to report

173 $\delta^{44}Ca$ data relative to BSE in order to more clearly represent potential complementarity between

174 various solid-Earth reservoirs and have converted published data using the values listed in Table

175 1.

176 **Table 1.** Values for inter-conversion of $\delta^{44}Ca$ results using common standard materials.

<div align="center">Measured Ca reference</div>

		BSE	SRM915A	SRM915B	Seawater	BSE 44/42	SRM915A 44/42	SRM915B 44/42	Seawater 44/42
	BSE		-0.95	-0.23	0.90	x2.05			
	SRM915A	0.95		0.72	1.85		x2.05		
	SRM915B	0.23	-0.72		1.13			x2.05	
	Seawater	-0.90	-1.85	-1.13					x2.05
	BSE 44/42	÷2.05							
	SRM915A 44/42		÷2.05						
	SRM915B 44/42			÷2.05					
	Seawater 44/42				÷2.05				

Desired Ca reference (row label spanning rows 1-8)

The conversion factors listed above are additive (columns/rows 1-4), while conversions between 42/44 and 44/40 are multiplicative.

The delta values can be related to isotopic ratios by the accepted 42/44= 0.31221 and 40/44 BSE = 47.162.

177 Additional complications result from small radiogenic ^{40}Ca enrichments in standard SRM915a

178 [and in modern carbonates/seawater (Antonelli et al., 2018)] relative to basaltic igneous rocks

179 (Antonelli et al., 2019a; He et al., 2017; Mills et al., 2018; Simon et al., 2009; Zhao et al., 2017),

180 meteorites (Simon et al., 2009; Yokoyama et al., 2017), and modern hydrothermal fluids

181   (Antonelli et al., 2019a). These radiogenic enrichments can lead to small discrepancies in

182   reported δ^{44}Ca values depending on the analytical technique. TIMS measurements are sensitive

183   to radiogenic ^{40}Ca variations, whereas multi-collector inductively-coupled plasma mass

184   spectrometry (MC-ICP-MS) analyses (which do not commonly measure ^{40}Ca due to isobaric

185   interferences from ^{40}Ar) are not affected by radiogenic Ca variations. The difficulty of achieving

186   a stable signal for ^{42}Ca using MC-ICP-MS (which requires high-resolution slits in order to

187   separate ^{42}Ca from a large isobaric interference at mass 42), however, stifles the potential

188   dominance of this method over TIMS. The radiogenic ^{40}Ca enrichments in SRM915a and

189   seawater (^{40}Ca/^{44}Ca of 47.162 *vs.* ~47.156 for BSE, at a normalizing ^{42}Ca/^{44}Ca ratio of 0.31221)

190   are just barely resolvable with current analytical precisions (~0.1‰) and still await further

191   confirmation before renormalization of all TIMS data (Antonelli et al., 2019a, 2018; Mills et al.,

192   2018). The apparent radiogenic enrichments in SRM915a and seawater, however, would require

193   a negative shift of ~0.1‰ for TIMS δ^{44}Ca data from samples with lesser amounts of radiogenic

194   ^{40}Ca than the normalizing standards.

195   **2.1. Bulk silicate Earth composition: measurements and models**

196   Early literature data for oceanic basalts suggest relatively large (>0.5‰) variations in δ^{44}Ca

197   (DePaolo, 2004; Skulan et al., 1997; Zhu and Macdougall, 1998). Likewise, measurement of

198   igneous minerals, especially the principal Ca-bearing minerals found in mantle peridotites

199   (clinopyroxene, orthopyroxene), exhibit significant isotopic heterogeneity (*e.g.* S. Huang et al.,

200   2010). Based on these observations and the upper mantle mineral assemblage, Huang et al.

201   (2010) estimated that the upper mantle and thus Bulk Silicate Earth (BSE) δ^{44}Ca is 1.05±0.04‰,

202   relative to Ca isotope standard SRM915a. This mantle estimate is slightly higher (by ~0.1) than

203   the average δ^{44}Ca of the basalt samples measured by Huang et al. (2010), and the average value

204 reported by Amini et al. (2009) and more recent studies. Using the published data on igneous

205 rocks from Skulan et al. (1997) and DePaolo (2004) the approach of Huang et al. (2010) would

206 indicate that δ^{44}Ca of BSE should be close to ~1.00±0.15‰, relative to standard SRM915a. The

207 work of Simon and DePaolo (2010) found that the average δ^{44}Ca value representing a large

208 diversity of differentiated materials and ordinary chondritic meteorites (n=12), including samples

209 from the Moon and Mars, is indistinguishable from terrestrial basalts and mantle peridotites

210 (n=5) and used this value to define both the Ca isotopic composition of BSE as well as the

211 terrestrial planets and planetary bodies that formed within the inner Solar System (their value for

212 BSE is 0.97±0.07‰ after re-normalization to the δ^{44}Ca of SRM915a). More recently, Kang et al.

213 (2017) reported that a subset of 28 peridotites xenoliths, those which experienced little or no

214 melting and metasomatism (n=14) exhibited limited δ^{44}Ca variation from 0.90 to 0.99‰ yielding

215 an average value of 0.94±0.05‰ (relative to SRM915a). Following a similar approach to Simon

216 and DePaolo (2010), Kang et al. (2017) used their new data and a compilation of available Ca

217 isotope literature data to define the Ca isotopic composition of BSE (δ^{44}Ca = +0.95 ± 0.05‰,

218 relative to SRM915a). Given the precision and accuracy of Ca isotope measurements in the

219 published literature it appears that both approaches, those that compute BSE values from mineral

220 compositions and those who define BSE from representative whole rock samples (from Earth

221 and other planetary bodies) yield similar values. As more studies of carefully selected mantle-

222 derived samples are analyzed, the Ca isotopic composition of the upper mantle will be more fully

223 characterized.

224 **2.2. Observations from igneous rocks**

225 Since the first observation of systematic δ^{44}Ca variations in Hawaiian basalts (Huang et al.,

226 2011) there have been well over 40 studies focused on exploring Ca isotope variations in

227 igneous rocks. A dominant proportion of these studies have measured $\delta^{44}Ca$ in different types of

228 mantle (ultramafic) whole rocks, while a more limited number of studies explore $\delta^{44}Ca$ in

229 intermediate to felsic igneous rocks. Ultramafic samples are generally defined by their modal

230 mineralogies, falling into two main categories, pyroxenites (orthopyroxenites, websterites, and

231 clinopyroxenites, with or without olivine) and peridotites (lherzolites, harzburgites, wehrlites,

232 and dunites). In a general sense, starting from fertile mantle and extracting basaltic melt, one is

233 left with residual lherzolite (> 5% Cpx), and with greater melt extraction, residual harzburgite (<

234 5% Cpx). Reactions between percolating pyroxene-undersaturated basaltic melts and lherzolites

235 can then lead to formation of replacive dunites (> 90% olivine), while simultaneous melt-

236 percolation and crystallization can lead to formation of websterites (< 5% olivine),

237 clinopyroxenites (> 90% Cpx), orthopyroxenites (> 90% Opx), and wehrlites (<5% Opx),

238 depending on the saturation state of the percolating melt with respect to the various minerals

239 (*e.g.* Chen et al., 2019b). Further classification of major ultramafic rock types depends on the

240 presence of either spinel or garnet as an aluminous phase, with garnet-bearing rocks indicative of

241 higher pressures. Mafic to felsic rocks are also distinguished through modal mineralogy but are

242 more commonly classified by their SiO_2 and associated alkali element concentrations (Na_2O and

243 K_2O).

244 In Fig. 1, we have compiled >650 igneous whole rock $\delta^{44}Ca$ measurements and have grouped

245 them by major rock type, increasing from ultramafic (bottom) to felsic compositions (top).

246 Within each major group the categories are further broken down by whether they are intrusive or

247 extrusive, and then by their dominant mineralogies (if originally described).

248 Although there is scatter in the data, the first observation is that there is a rough inverse

249 relationship between SiO_2 content and $\delta^{44}Ca$, where increasingly felsic rocks have decreasing

250    $\delta^{44}Ca$ (Fig. 1). This observation is in agreement with recent work regarding the average $\delta^{44}Ca_{BSE}$

251   compositions of mid-ocean ridge basalts (MORB, ~ -0.1‰) (Chen et al., 2019a) and estimated

252   average continental crust (~ -0.2‰) (Wang et al., 2019) relative to non-metasomatized peridotite

253   samples, *e.g.* (Chen et al., 2019b). By combining data from different labs, figure 1 compensates

254   for potential inter-lab biases (*e.g.* ~0.2‰ variation in published values for BHVO and BCR-2

255   standards), but additional work is necessary in order to reach agreement between labs and move

256   forward with higher precision Ca isotope measurements as a community.

257
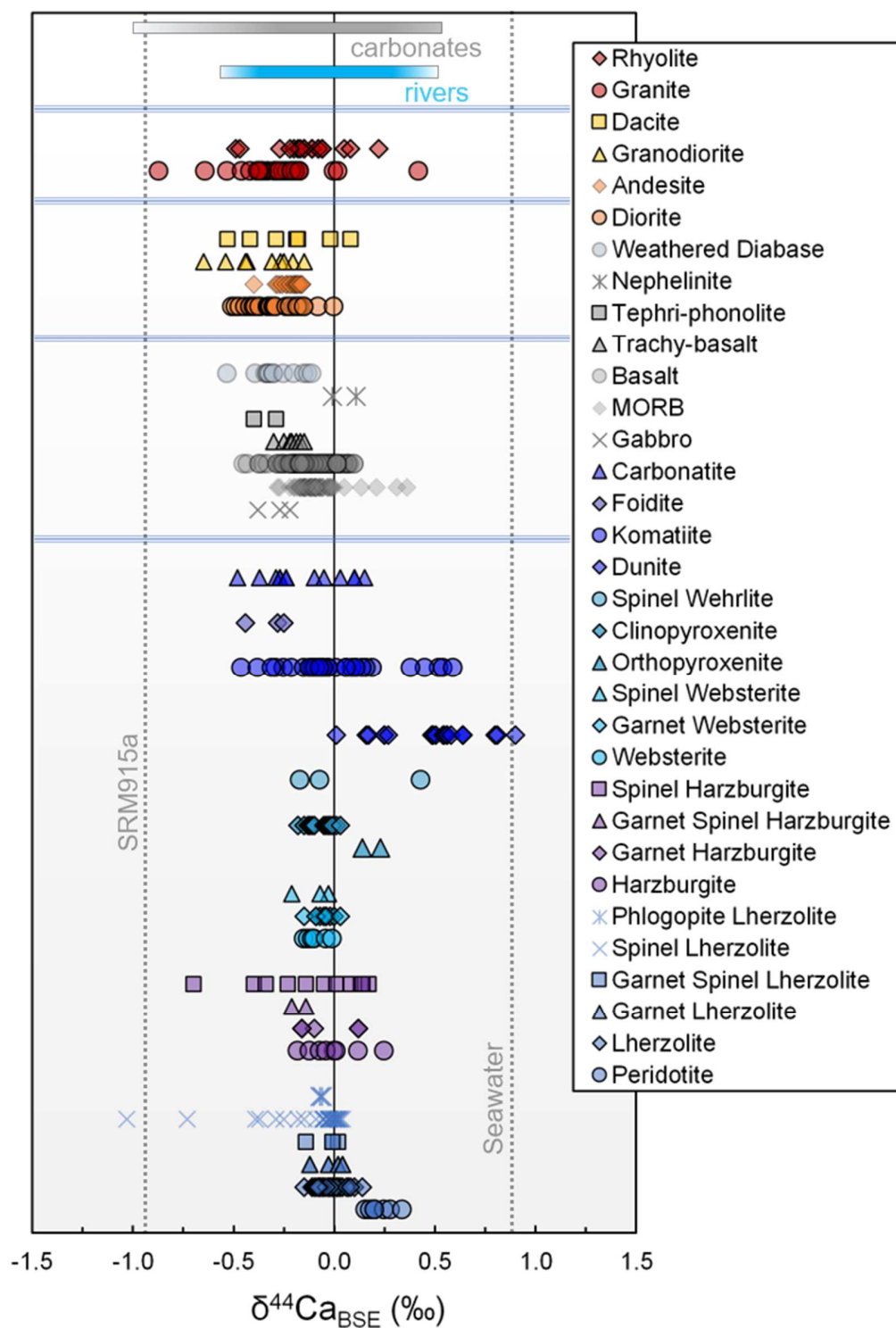
Fig. 1. Compilation of $\delta^{44}Ca_{BSE}$ in igneous whole rocks (n = 655) grouped by major sample type. All TIMS data

have been corrected for radiogenic ^{40}Ca variations, when applicable, and all data are normalized to Bulk-silicate

260 Earth (BSE). $\delta^{44}Ca_{BSE}$ is +0.95‰ relative to standard SRM915a, +0.23‰ relative to SRM915b, and -0.90‰ relative

261 to seawater (see Table 1). Igneous rock data are from (Amini et al., 2009; Amsellem et al., 2019, 2017; Antonelli et

262 al., 2019b; Banerjee and Chakrabarti, 2019, 2018; Chen et al., 2019a, 2019b, 2018; Colla et al., 2013; Dai et al.,

263 2020; DePaolo, 2004; Feng et al., 2018, 2016; He et al., 2017; Holmden and Bélanger, 2010; Huang et al., 2011; S.

264 Huang et al., 2010; Ionov et al., 2019; Jacobson et al., 2015; Jochum et al., 2006; John et al., 2012; Kang et al.,

265 2017; Lehn and Jacobson, 2015; Liu et al., 2017b, 2017a; Lu et al., 2019; Magna et al., 2015; Peterson, 2013;

266 Richter et al., 2003; Ryu et al., 2011; Schiller et al., 2012; Simon et al., 2017; Simon and DePaolo, 2010; Skulan et

267 al., 1997; Valdes et al., 2014; Wang et al., 2017b, 2019; Wombacher et al., 2009; Zhang et al., 2018; Zhao et al.,

268 2017; Zhu et al., 2020, 2018; Zhu and Macdougall, 1998). The approximate ranges for 95% of carbonates and rivers

269 come from (Fantle and Tipper, 2014).

270 Ultramafic samples have the highest $\delta^{44}Ca$ variability of all analyzed igneous rocks, though this

271 may be partially due to the greater number of analyzed samples (Fig. 1). The ultramafic samples

272 with the highest $\delta^{44}Ca$ are dunites, which is likely due to their high percentages of olivine (which

273 is predicted to favor heavy isotopes at equilibrium, discussed in Section 3). The lightest

274 ultramafic $\delta^{44}Ca$ values are found in komatiites, foidites, carbonatites, and spinel lherzolites and

275 harzburgites. The spinel-facies sub-types of lherzolites, harzburgites, and websterites tend to

276 have more negative $\delta^{44}Ca$ than their garnet-facies counterparts. This observation may be

277 explained by the presence of garnet as an isotopically heavy residual phase (discussed in Section

278 3) but requires further exploration. Heavy $\delta^{44}Ca$ compositions in certain komatiites have been

279 argued to reflect mantle-heterogeneities inherited from Ca-perovskite crystallization during the

280 early magma ocean period of Earth history, while light $\delta^{44}Ca$ may reflect incorporation of

281 serpentinized oceanic crust into komatiite sources (Amsellem et al., 2019); only one study,

282 however, suggests that subducting slabs preferentially lose fluids enriched in heavy Ca isotopes

283 (John et al., 2012). This conclusion was reached primarily because blueschists adjacent to

284 eclogites in Western Tianshan had slightly heavier Ca isotopic compositions (suggesting the

14

285   influx of fluids enriched in heavy Ca isotopes), but it is uncertain whether this reflects (i) a

286   primary signature of the fluids lost from the eclogites or (ii) that these fluids were subsequently

287   enriched due to precipitation of isotopically light carbonates (John et al., 2012). A recent study

288   suggests that prograde dehydration metamorphism in subduction zones does not lead to

289   significant Ca isotope fractionation (Lu et al., 2019), which lends weight to the second

290   interpretation. Much more work is needed, however, to understand Ca isotope fractionations in

291   subduction zones. The lowest $\delta^{44}Ca$ values in ultramafic rocks are suggested to stem from kinetic

292   effects during metasomatism (Zhao et al., 2017), which is further discussed in Section 6.2. Rarer

293   igneous rocks, such as carbonatites, are rich in carbonate minerals, which may potentially

294   explain their isotopically light compositions, while low $\delta^{44}Ca$ in alkali-rich groups (foidites)

295   require further exploration. Trachy-basalts, like foidites, also have slightly lower $\delta^{44}Ca$ compared

296   to basalts, which may suggest a role for increasing alkali element concentrations.

297   Although there is significantly less data for intermediate to felsic rocks, the largest variations are

298   observed in granites (Fig. 1). Granites, along with intermediate igneous rocks, have $\delta^{44}Ca$ almost

299   exclusively more negative than bulk silicate Earth, but their higher variability (> 1‰) compared

300   to other groups suggests that they are (i) affected by a greater number of (potentially kinetic)

301   processes and/or (ii) that they incorporate a greater variety of isotopically-distinct source

302   materials. A larger number of studies on intermediate to felsic rocks is required to understand

303   this variability.

304   Given the greater number of data for ultramafic samples, partial melting and fractional

305   crystallization processes (as shown in Fig. 2) are better understood in mantle rocks. The general

306   observation is that partial melting of fertile mantle generally leaves behind isotopically heavier

307   mafic minerals (*e.g.* Opx, Ol) and higher Mg#, defined $10^2[Mg/(Mg+Fe)]$, as isotopically lighter

308   phases (*e.g.* Cpx) are preferentially lost to the melt. Fractional crystallization of mafic phases

309   leads to decreasing Mg# in the residual liquid, but the isotopic effects are negligible as a

310   probable consequence of their low Ca concentrations (*e.g.* olivine, orthopyroxene). Zhang et al.

311   (2018) modeled melting of spinel facies peridotite (Fig. 2c,d) at pressures between 1 and 2 GPa

312   using the pMELTS program. They found that isotopic variations generated from both primitive

313   and depleted mantle compositions lead to less than ~0.1‰ variation in the melt fractions.

314   Residual material, on the other hand, can show larger variations, as isotopically-heavy

315   orthopyroxene becomes the dominant Ca bearing phase, with potential δ^{44}Ca increases of the

316   order ~0.2 to 0.3‰ [at a corresponding melt-fraction (F) of 0.3] when using a fractional melting

317   model (Zhang et al., 2018). Mantle melting at higher-pressure, amenable to the stabilization of

318   garnet as a residual phase, leads to larger effects (up to ~0.4‰) for the generated melts (Kang et

319   al., 2019), while generation of adakitic melts may succumb to similar processes (Wang et al.,

320   2019). Fractionation factors still remain poorly constrained, however, and the large δ^{44}Ca

321   variations observed in metasomatized mantle samples, along with their relationships to a wide

322   variety of percolating mantle fluids [potentially causing kinetic isotope fractionations (*e.g.* Zhao

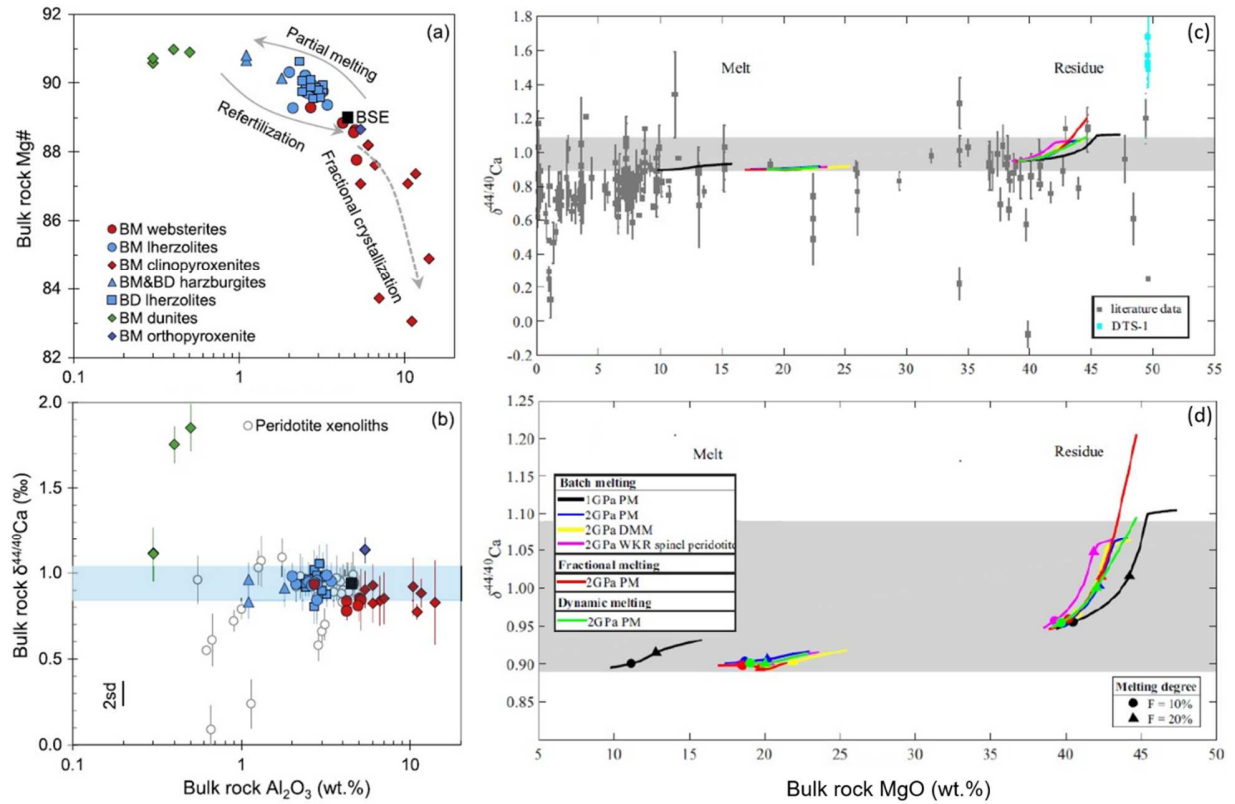323   et al., 2017)], still merit further study.

Fig. 2a-d. (a,b) Bulk chemical and δ⁴⁴Ca data for ultramafic rocks from the Balmuccia (BM) and Baldissero (BD) orogenic massifs, showing predicted effects of partial melting, crystallization, and mantle refertilization after (Chen et al., 2019b). Fertile lherzolite and harzburgite xenoliths are shown for comparison (hollow symbols) (Kang et al., 2017; Zhao et al., 2017). δ⁴⁴Ca data are relative to SRM915a, and the blue horizontal band represents the estimated δ⁴⁴Ca of the Earth's upper mantle (0.94 ± 0.10‰). The long-term external precision from Chen et al. (2019b), ~0.14‰ (2sd) is shown at the bottom left. **(c)** Plot of whole rock δ⁴⁴Ca versus MgO for igneous rocks with model predictions for partial melting of the mantle at 1 and 2 GPa. Horizontal grey band represents BSE composition estimates with uncertainty, after Zhang et al. (2018). **(d)** same as (c) but with expanded y-axis and without data, to more clearly show predicted effects of partial melting [model details can be found in Zhang et al. (2018)]. Data come from studies published before 2019 (Amini et al., 2009; Colla et al., 2013; DePaolo, 2004; Fantle and Tipper, 2014; Feng et al., 2016; He et al., 2017; Holmden and Bélanger, 2010; S. Huang et al., 2010; Huang et al., 2011; Jacobson et al., 2015; Jochum et al., 2006; John et al., 2012; Kang et al., 2017, 2016; Lehn and Jacobson, 2015; Liu et al., 2017a, 2017b; Magna et al., 2015; Richter et al., 2003; Ryu et al., 2011; Schiller et al., 2012; Simon et al.,

338 2017; Simon and DePaolo, 2010; Skulan et al., 1997; Valdes et al., 2014; Wombacher et al., 2009; Zhang et al.,

339 2018; Zhao et al., 2017; Zhu et al., 2018; Zhu and Macdougall, 1998).

340 **2.3. Observations from metamorphic rocks**

341 Metamorphic rocks are typically classified based on mineral compositions and modal

342 mineralogy, which are related to the starting materials (either igneous or sedimentary protoliths)

343 and to the temperature and pressure conditions of metamorphism. In a general sense, high

344 temperature metamorphism (*e.g.* granulite-facies, T > ~750°C, ~0.4-1.4 GPa) favors the

345 transformation of hydrous minerals to anhydrous assemblages, whereas high-pressure

346 metamorphism [*e.g.* blueschist-facies (< ~500°C, ~0.5-1.5 GPa) and eclogite-facies (> ~400°C, >

347 ~1.5 GPa)] favors the formation of high-density mineral assemblages, though dehydration can

348 also occur. Metamorphic facies intermediate to the others (*e.g.* greenschist and amphibolite-

349 facies) are also defined by their mineral assemblages and result from the variable influences of

350 metasomatic fluids, temperature (300-700°C), and pressure (~0.2 to ~1 GPa).

351 Although Ca isotopes in metamorphic rocks are not as extensively studied as in igneous rocks,

352 the limited number of studies (Antonelli et al., 2019c; John et al., 2012; Kang et al., 2019; Liu et

353 al., 2017b; Lu et al., 2019; Peterson, 2013; Valdes et al., 2019; Wang et al., 2019; Wombacher et

354 al., 2009) suggest that large fractionation effects occur during metamorphism. Whole rocks span

355 a $\delta^{44}Ca$ range of ~6‰ (-2.5 to +3.3‰ relative to BSE, Fig. 3). The $\delta^{44}Ca$ variations appear to get

356 larger with increasing metamorphic grade, with the largest fractionations in rocks that have

357 experienced upper amphibolite-facies (Peterson, 2013) and granulite-facies metamorphism

358 (Antonelli et al., 2019c; Valdes et al., 2019).

Fig. 3. $\delta^{44}Ca_{BSE}$ for metamorphic whole rocks grouped by principal metamorphic facies and protolith-type (n = 72). Data are from (Antonelli et al., 2019c; John et al., 2012; Kang et al., 2019; Liu et al., 2017b; Lu et al., 2019; Peterson, 2013; Valdes et al., 2019; Wombacher et al., 2009), retrograde greenschist data are from Valdes et al. (2018).

Given that inter-mineral fractionations in a closed system should not result in whole rock $\delta^{44}Ca$ variations, the observed variability indicates that Ca isotope fractionations occur in open systems and require either addition or removal of isotopically distinct components during metamorphism. The larger fractionations at higher temperatures suggest that the $\delta^{44}Ca$ effects are likely to be the result of kinetic fractionation effects during Ca diffusion, melting, and/or dehydration reactions, which are further discussed in Section 6.

3. Equilibrium Ca isotope fractionation

As with many isotopic systems, the initial goal for inter-mineral Ca isotope analyses was to use them as constraints on equilibration temperature ('Ca isotope geothermometry'). Using Ca isotopes as a proxy for temperature in natural samples, however, requires (i) knowledge of equilibrium isotope fractionations between minerals at different temperatures, and (ii) that isotopic equilibrium was reached between minerals. The following sections evaluate the potential use of Ca isotopes for geothermometry and describe current constraints on equilibrium $\Delta^{44}Ca_{a-b}$, defined:

$$\Delta^{44}Ca_{a-b} = \delta^{44}Ca_a - \delta^{44}Ca_b \qquad \text{(Eq. 2)}$$

Where subscripts 'a' and 'b' denote two minerals 'a' and 'b'.

3.1. General background principles

Isotope partitioning between mineral phases at equilibrium depends mainly on vibrational frequency differences for heavy *vs.* light isotopes in mineral structures. Tighter bonds (with higher vibrational frequencies) are preferentially stabilized by substitution of a heavy isotope. This effect is a consequence of quantum mechanical factors, where tighter bonds have greater relative decreases in zero-point energy (ZPE, the quantized vibrational energy of a chemical bond at absolute zero), which stems from the Heisenberg uncertainty principle, and in higher-level vibrational frequencies upon substitution of a heavier isotope (Bigeleisen and Mayer, 1947; Chacko et al., 2001; Urey, 1947; Young et al., 2002). Consequently, heavier isotopes are preferentially placed into mineral sites with stronger bonds in order to decrease the Gibbs free energy (ΔG) of a system. For Ca isotopes, this leads to higher $\delta^{44}Ca$ in minerals with stronger/shorter Ca-O bonds. When bond lengths are unknown, a general rule is that sites with

392 higher coordination numbers have longer bonds and therefore have less preference for heavy

393 isotopes than sites with lower coordination numbers [*e.g.* Ca-perovskite has 12-fold coordination

394 and is thus predicted to have low reduced-partition function ratios (RPFR, discussed in Section

395 3.2) and concentrate lighter Ca isotopes (Amsellem et al., 2019)]. At a given Ca-O bond-length,

396 however, it is important to note that sites with higher coordination numbers have stronger overall

397 bonding environments and therefore favor heavier isotopes.

398 Equilibrium constants for isotopic substitution reactions (denoted α, as opposed to K for

399 chemical equilibrium constants) are highly dependent on temperature due to the increasing

400 population of higher quantum vibrational states with increasing temperatures (Chacko et al.,

401 2001). As a result, isotopic differences between mineral pairs are often used as constraints on

402 equilibration temperature ('isotope geothermometry'), where higher temperatures are expected to

403 decrease inter-mineral fractionations.

404 Equilibrium fractionation factors (α), which must be constrained in order to derive temperatures

405 from isotopic data, can be obtained through various methods. These generally include (i) direct

406 measurements from experiments, such as mineral-mineral or mineral-carbonate exchange

407 experiments (Chacko et al., 2001; Shahar et al., 2008), and/or determination of vibrational

408 frequencies through (ii) advanced spectroscopic techniques [*e.g.* nuclear resonant inelastic x-ray

409 scattering (Dauphas et al., 2012)], or (iii) ab-initio simulations (*e.g.* Widanagamage et al., 2014).

410 The determination of vibrational frequencies using spectroscopic methods is not currently

411 possible for Ca because there are no Mossbauer-sensitive isotopes. Common experimental

412 approaches (*e.g.* Kueter et al., 2019; Shahar et al., 2008) would technically allow for the

413 determination of equilibrium Ca isotope fractionation factors, but at present we are not aware of

414 any reliable experimental constraints. Thus, our current understanding of equilibrium Ca isotope
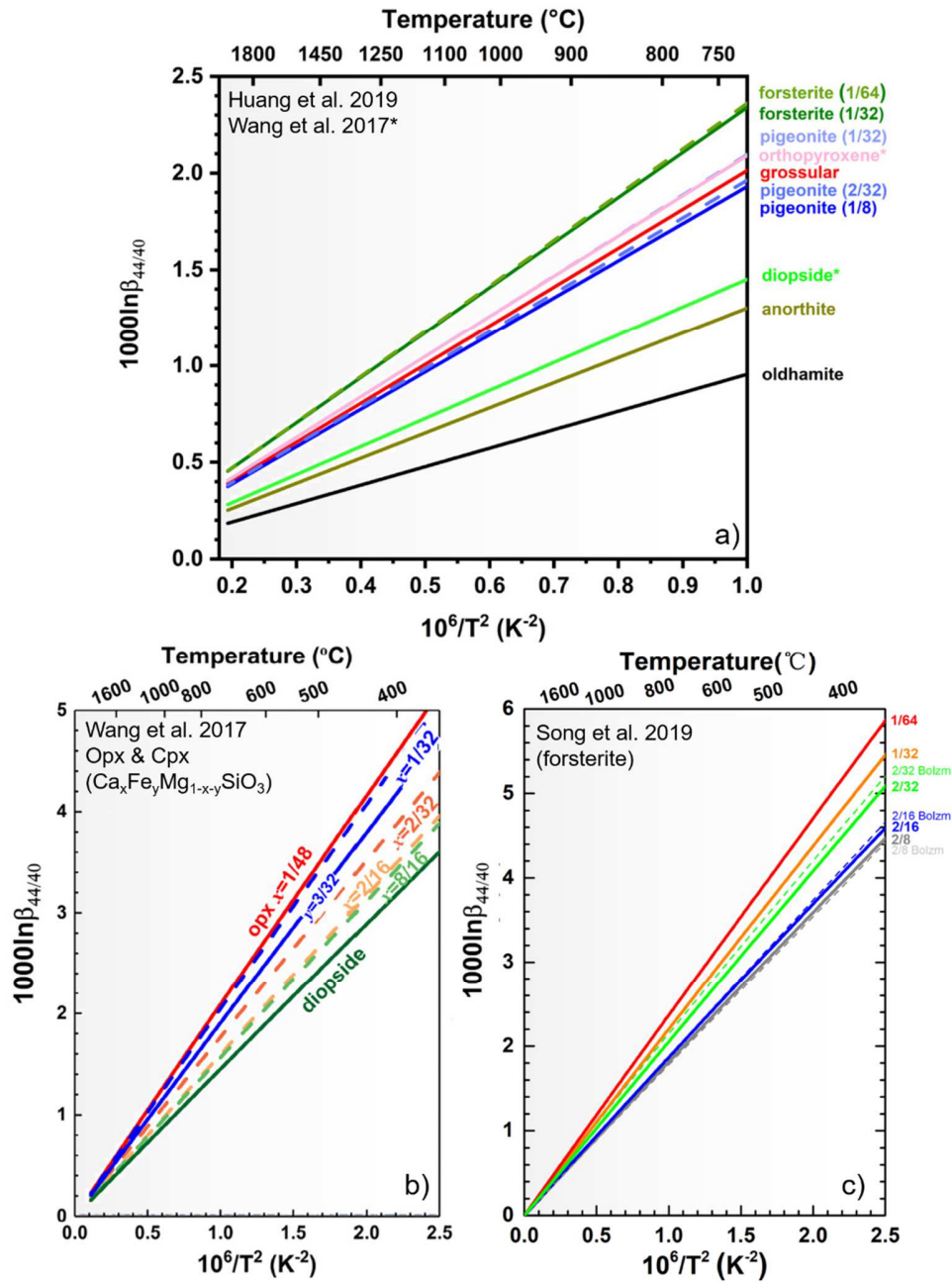
415   fractionation between various minerals relies principally on ab-initio estimates, which are

416   discussed in the following section.

3.2. Ab-initio Predictions

418   The first Ca isotope measurements in mineral separates revealed large $\delta^{44}Ca$ differences (~1 ‰)

419   in orthopyroxene and clinopyroxene from mantle xenoliths (S. Huang et al., 2010), suggesting

420   that Ca isotope fractionations could potentially be used for geothermometry. The first ab-initio

421   estimates for equilibrium Ca isotope fractionation between minerals, published four years later,

422   confirmed the initial observation that orthopyroxene concentrates heavy isotopes of Ca over

423   clinopyroxene at equilibrium. Ab-initio techniques generally rely on advanced computational

424   methods that serve to predict vibrational frequency shifts for different isotopes in a given

425   molecule or crystal lattice, which can then be used to predict equilibrium isotope effects.

426   Predicted equilibrium $\Delta^{44}Ca_{opx-cpx}$ values were found to range from ~0.3‰ at 1200°C to ~1‰ at

427   500°C (Feng et al., 2014), which has also been corroborated by more recent ab-initio studies

428   (Antonelli et al., 2019c; Wang et al., 2017b). Equilibrium predictions for minerals other than

429   pyroxenes have only recently been investigated (Antonelli et al., 2019c; Huang et al., 2019; Song

430   et al., 2019), but find that olivine is expected to have the heaviest Ca isotope compositions,

431   followed by garnet, orthopyroxene, clinopyroxene, apatite, anorthite, labradorite (An_{50}), and

432   oldhamite (CaS).

433   In Fig. 4 we show the reduced partition function ratios (formalized as $1000ln\beta$, which quantifies

434   the preference for heavy *vs.* light isotopes within a single phase) for various minerals *vs.*

435   temperature (Huang et al., 2019; Song et al., 2019; Wang et al., 2017a). Fractionation factors

436   ($1000ln\alpha$), which represent the prediction for $\Delta^{44}Ca_{a-b}$ between two minerals, can be

437 approximated visually from these kinds of figures using $1000\ln\beta_a - 1000\ln\beta_b$, but should be

438 calculated using $\alpha_{a-b} = \beta_a/\beta_b$ (note: $\Delta^{44}Ca_{a-b} \approx 1000\ln\alpha_{a-b} = 1000\ln\beta_a - 1000\ln\beta_b$).

439

440 **Fig. 4a-c.** Equilibrium estimates for reduced partition function ratios (1000lnβ) *vs.* temperature in various minerals,

441 based on DFT models using local-density approximation (LDA) functionals. **(a)** Modified from Huang et al. (2019),

442 orthopyroxene and diopside estimates (*) are from Wang et al. (2017b). **(b)** Orthopyroxene with various solid-

The major-cation compositions of solid-solution minerals are also expected to affect Ca isotope fractionation (Antonelli et al., 2019c; Feng et al., 2014; Huang et al., 2019; Song et al., 2019; Wang et al., 2017b). For example, the preference for heavy Ca isotopes in orthopyroxene decreases with increasing Ca/Mg (Antonelli et al., 2019c; Feng et al., 2014; Huang et al., 2019; Wang et al., 2017b), as depicted in Figs. 4b and 5. This effect is a general manifestation of increasing distortions in the mineral lattice with increasing Ca abundances (due to the relatively large size of Ca compared to Mg). The distortions lead to increased average Ca-O bond lengths and thus decrease the overall affinity for heavy Ca isotopes (Antonelli et al., 2019c; Feng et al., 2014; Wang et al., 2017b). This dilution effect, however, becomes negligible below a Ca/(Ca+Mg) of ~1/32 in orthopyroxene, and larger $\Delta^{44}Ca_{Opx-Cpx}$ are not predicted at lower values (Antonelli et al., 2019c; Wang et al., 2017b). Small dilution effects are also predicted for increasing orthopyroxene Fe/Mg, where increasing Ca-O bond lengths with increasing Fe lead to slightly decreased affinities for heavy Ca isotopes (Wang et al., 2017b). For pigeonite (a high-temperature pyroxene phase that commonly separates into orthopyroxene and clinopyroxene lamellae upon slow-cooling), RPFRs are generally found to be intermediate to clinopyroxene and orthopyroxene and also decrease with increasing pigeonite Ca/Mg (Huang et al., 2019), shown in Fig. 4a.

Ca dilution effects (also known as "Ca concentration effects", depending on the author) have also been investigated in olivine, but have contradictory results. One study suggests that decreasing Ca/Mg in olivine leads to increased RPFRs, Fig. 4c [~0.3‰ difference between 1/16 and 1/64 at 1000 K (Song et al., 2019)], while another study suggests that Ca concentrations in

olivine have no significant effect on its affinity for heavy Ca isotopes [(only ~0.1‰ difference between 1/16 and 1/64 at 1000 K (Antonelli et al., 2019c)]. Future experiments are required to confirm the veracity of dilution effects in olivine.

Garnet solid-solution end-members have decreasing RPFRs when the major cation is changed from Mg to Fe, Mn, and Ca [1000lnβ of pyrope > almandine ≈ spessartine > grossular (Antonelli et al., 2019c)], as shown in Fig. 5. Ca dilution effects in garnet have only been investigated in pyrope, but no significant difference was found between estimates with Ca/(Ca+Mg) of 1/12 and 1/24 (Antonelli et al., 2019c).

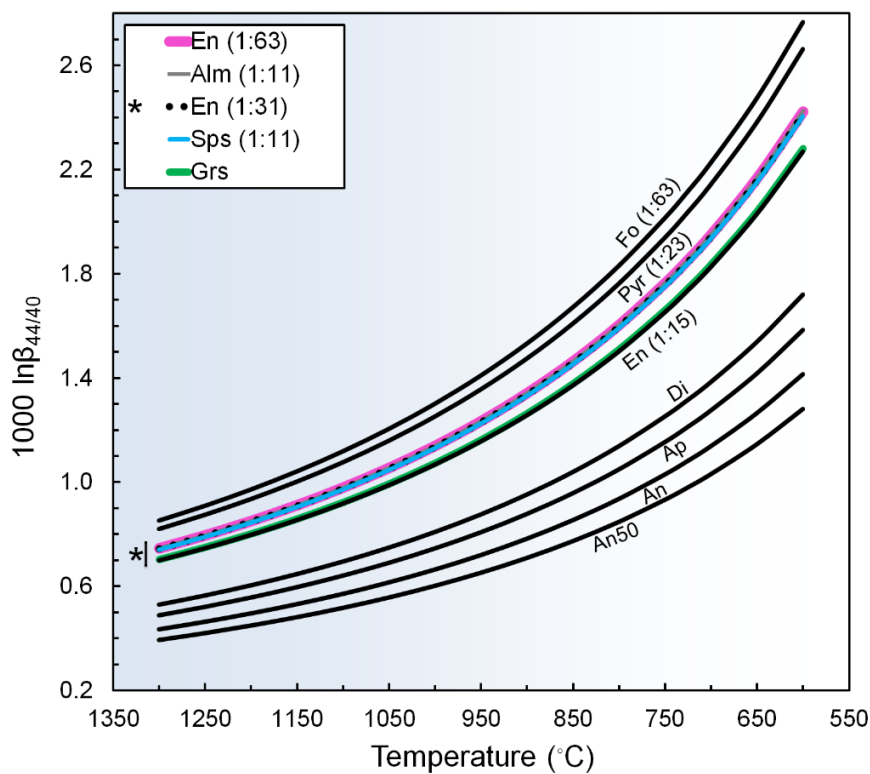**Fig. 5.** Equilibrium estimates for reduced partition function ratios (1000lnβ) for $^{44}Ca/^{40}Ca$ *vs.* temperature for minerals based on DFT models using generalized gradient approximation (GGA) PBE functionals (Perdew, Burke, Ernzerhof), modified from (Antonelli et al., 2019c). As opposed to Fig. 4, the lines are curved due to use of a linear temperature scale.

479   The disagreement between predicted differences for Ca dilution effects in various minerals may

480   be explained by methodological differences between the various studies, which use different

481   approximations for defining the relevant electronic structures. Greater dilution effects due to

482   decreasing Ca concentrations in both orthopyroxene and olivine are generally predicted when

483   using local-density approximation (LDA) functionals (Feng et al., 2014; Huang et al., 2019;

484   Song et al., 2019; Wang et al., 2017b), while smaller effects are predicted when using

485   generalized gradient approximations (GGA) such as PBE (Perdew, Burke, Ernzerhof) functionals

486   (Antonelli et al., 2019c). LDA functionals are the simplest type of density functional, where the

487   exchange-correlation energy density is assumed to be that of a uniform electron gas at a single

488   point; GGA functionals (such as PBE) are formulas that use both the energy density and its

489   gradient at each point, which gives more accurate estimates of bond dissociation energies and

490   transition-state barriers (Rappoport et al., 2011). The slightly smaller $1000\ln\beta$ values and Ca

491   dilution effects in Antonelli et al. (2019c) may thus be due the use of GGA *vs.* LDA exchange-

492   correlation functionals. However, this becomes less important when calculating equilibrium

493   fractionation factors (α) because they depend only on the RPFR *differences* between phases.

494   Nevertheless, some of the differences between predicted equilibrium fractionation factors

495   ($1000\ln\alpha$) are greater than average analytical uncertainties for $\delta^{44}Ca$ (~0.1‰), even at high

496   temperatures, and are worthy of further investigation.

497   Despite the different approaches used in the DFT estimates and small discrepancies between

498   predicted $1000\ln\alpha$ for certain mineral pairs, first-order agreement is reached between the various

499   studies regarding the general effects of mineral Ca concentration and average Ca-O bond length

500   on predicted fractionation factors. In Figure 6, we show a summary of $^{44}Ca/^{40}Ca$ RPFRs from all

501   published ab-initio studies versus (i) Ca concentrations, defined as Ca/(Ca+Mg+Fe+Mn+Na), in

502   various minerals (Fig. 6a) and (ii) average Ca-O bond lengths (Fig. 6b). This figure demonstrates

503   that minerals with less Ca (*e.g.* olivine, orthopyroxene, pyrope) generally have higher affinities

504   for ^{44}Ca, while minerals with higher Ca concentrations (*e.g.* clinopyroxene & plagioclase) have

505   lower affinities for ^{44}Ca. It also illustrates the dependence of 1000lnβ values on average Ca-O

506   bond lengths and coordination numbers, where longer Ca-O bonds lead to lower affinities for

507   ^{44}Ca and greater coordination numbers at a given bond-length lead to increased affinities for ^{44}Ca

508   (Fig. 6b).

510   **Fig. 6a,b.** Summary of available equilibrium estimates for ^{44}Ca/^{40}Ca reduced partition function ratios (1000lnβ) *vs.*

511   (**a**) Ca concentrations relative to other major cations, Ca/(Ca+Mg+Fe+Mn+Na), and (**b**) average Ca-O bond lengths

512   in various minerals. PBE-based estimates (colored symbols) are generally lower than LDA-based estimates. Data are

513   from (Antonelli et al., 2019c; Feng et al., 2014; Huang et al., 2019; Song et al., 2019; Wang et al., 2017b).

514   Despite the general agreement for inter-mineral fractionation factors between studies, absolute

515   values for 1000lnβ in single minerals can be dramatically different based on the approach [*e.g.*

516   ~2.5 (Song et al., 2019) *vs.* ~1.8 (Antonelli et al., 2019c) for forsterite with Ca/(Ca+Mg) of 1/64

517   at 800°C], so it is important to use RPFR values that were derived from the same method when

calculating equilibrium fractionation factors ($\alpha_{a\text{-}b} = \beta_a/\beta_b$) to arrive at internally-consistent predictions for inter-mineral Δ^{44}Ca. We also provide a compilation of RPFRs and fitting parameters for inter-mineral fractionations (Antonelli et al., 2019c; Feng et al., 2014; Huang et al., 2019; Song et al., 2019; Wang et al., 2017b), to serve as a reference for future studies (Table 2).

Table 2. Compilation of *ab-intio* predictions and fitting-factors for equilibrium RPFRs (1000lnβ).

Reference	Type	Mineral		Ca/Ca+Fe+Mg+Mn+Na	1000lnβ (1000 K)	Coord.	Bond-length (Å)	a	b	c
Huang et al., 2019	LDA	Anorthite	-	1.000	1.30	6.75	2.455	6.21E-05	-5.68E-03	1.307
		Forsterite 1/32	Ca/Mg 1/32	0.031	2.34	6	2.269	1.63E-04	-1.51E-02	2.355
		Forsterite 1/64	Ca/Mg 1/64	0.016	2.36	6	2.267	0.00E+00	0.00E+00	2.362
		Grossular	-	1.000	2.01	8	2.393	1.08E-04	-1.08E-02	2.025
		Oldhamite	-	1.000	0.96	6	2.826	4.89E-06	-1.71E-03	0.957
		Pigeonite 1/8	Ca/Mg 1/8	0.125	1.93	7	2.375	1.15E-04	-1.11E-02	1.942
		Pigeonite 1/16	Ca.Mg 1/16	0.063	1.96	7	2.373	0.00E+00	0.00E+00	1.964
		Pigeonite 1/32	Ca/Mg 1/32	0.031	2.10	7	2.361	0.00E+00	0.00E+00	2.097
Song et al., 2019	LDA	Forsterite 1/64	Ca/Mg 1/64	0.016	2.37	6	2.267	2.36E-04	-1.57E-02	2.383
		Forsterite 1/32	Ca/Mg 1/32	0.031	2.20	6	2.284	2.09E-04	-1.41E-02	2.216
		Forsterite 1/16	Ca/Mg 1/16	0.063	2.01	6	2.299	1.74E-04	-1.21E-02	2.021
		Forsterite 1/16a	Ca/Mg 1/16	0.063	2.15	6	2.299	3.27E-03	-5.64E-02	2.202
		Forsterite 1/8	Ca/Mg 1/8	0.125	1.88	6	2.327	1.28E-04	-9.83E-03	1.888
		Forsterite 1/8a	Ca/Mg 1/8	0.125	1.87	6	2.327	1.25E-03	-2.46E-02	1.890
		Forsterite 1/4	Ca/Mg 1/4	0.250	1.78	6	2.333	1.27E-04	-9.12E-03	1.789
		Forsterite 1/4a	Ca/Mg 1/4	0.250	1.81	6	2.333	8.88E-04	-1.95E-02	1.831
Feng et al., 2014	LDA	Opx 1/32	Ca/Mg 1/32	0.031	2.05	6	2.305	1.88E-04	-1.27E-02	2.061
		Opx 1/16	Ca/Mg 1/16	0.063	1.77	6	2.363	1.51E-04	-9.71E-03	1.778
		Opx 1/8	Ca/Mg 1/8	0.125	1.59	6	2.392	1.31E-04	-8.27E-03	1.603
		Opx 1/2	Ca/Mg 1/2	0.500	1.57	6	2.388	1.20E-04	-7.70E-03	1.573
		Cpx 1/2	Ca/Mg 1/2	0.500	1.45	8	2.47	1.18E-04	-6.89E-03	1.458
Wang et al., 2017b	LDA	Opx 1/32 Fe 3/32	Ca/Mg 1/32 Fe 3/32	0.031	1.91	6	2.326	1.59E-04	-1.11E-02	1.918
		Opx 1/48	Ca/Mg 1/48	0.021	2.09	6	2.3	1.94E-04	-1.32E-02	2.104
		Cpx 3/8	Ca/Mg 3/8	0.375	1.54	8	2.459	1.26E-04	-7.61E-03	1.543
		Cpx 7/16	Ca/Mg 7/16	0.438	1.49	8	2.465	1.22E-04	-7.28E-03	1.498
		Cpx 15/32	Ca/Mg 15/32	0.469	1.50	8	2.469	1.23E-04	-7.28E-03	1.503
		Cpx 17/32	Ca/Mg 17/32	0.531	1.51	8	2.467	1.27E-04	-7.59E-03	1.521
		Cpx 9/16	Ca/Mg 9/16	0.563	1.53	8	2.462	1.28E-04	-7.83E-03	1.535
		Cpx 5/8	Ca/Mg 5/8	0.625	1.56	8	2.453	1.26E-04	-8.01E-03	1.571
		Diopside	-	0.500	1.45	8	2.47	1.18E-04	-6.89E-03	1.458
Antonelli et al., 2019c	PBE	Diopside	-	0.500	1.32	8	2.529	-	-	-
		Opx 1/16	Ca/Mg = 1/16	0.063	1.72	6	2.3649	Note: 7th Ca-O bond at 2.66Å		
		Opx 1/16	Ca/Mg = 1/16, 2c	0.063	1.73	6	2.3649	Note: 7th Ca-O bond at 2.66Å		
		Opx 1/32	Ca/Mg = 1/32, 2c	0.031	1.84	6	2.3445	Note: 7th Ca-O bond at 2.67Å		
		Opx 1/64	Ca/Mg = 1/64, 2c	0.016	1.85	6	2.343	Note: 7th Ca-O bond at 2.68Å		
		Forsterite 1/8	Ca/Mg = 1/8, M2	0.125	1.82	6	2.3314	-	-	-
		Forsterite 1/16	Ca/Mg = 1/16, 2a	0.063	2.10	6	2.2975	-	-	-
		Forsterite 1/32	Ca/Mg=1/32, 2ac	0.031	2.08	6	2.3010	-	-	-
		Forsterite 1/64	Ca/Mg=1/64, 4a2c	0.016	2.11	6	2.2977	-	-	-
		Grossular	-	1.000	1.74	8	2.4288	-	-	-
		Pyrope 1/12	Ca/Mg = 1/12	0.083	2.00	8	2.3797	-	-	-
		Pyrope 1/24	Ca/Mg = 1/24 fcc	0.042	2.03	8	2.3784	-	-	-
		Almandine 1/12	Ca/Fe = 1/12 fm	0.083	1.85	8	2.3876	-	-	-
		Spessartine 1/12	Ca/Mn = 1/12 fm	0.083	1.83	8	2.3999	-	-	-
		Anorthite	-	1.000	1.06	6	2.4608	Note: 7th Ca-O bond at ~2.9-3.0Å		
		Labradorite	An50-Ab50 v1	0.500	0.98	6	2.4871	Note: 7th Ca-O bond at 2.97-3.00Å for all Ca sites		
		Labradorite	An50-Ab50 v2	0.500	1.03	6	2.4740	Note: 7th Ca-O bond at 2.84Å for half of Ca sites		
		Labradorite	An50-Ab50 v3	0.500	1.01	6	2.4723	Note: 7th Ca-O bond at 2.92Å for half of Ca sites		
		Apatite	Fluorapatite	1.000	1.21	6	2.4205	Note: Ca1, *7-10th Ca-O neighbors at		

Lime (CaO)	-	1.000	1.51	6	2.4158	-	-	-
Fluorite (CaF₂)	-	1.000	1.34	8	2.3818	-	-	-

Fitting equation: $1000 \ln\beta = ax^3 + bx^2 + cx$, where $x = 10^6/T^2$, The various labradorite structures (v1-v3) used in Antonelli et al. (2019c) are from (Kaercher et al., 2014).

4. Observed inter-mineral Ca isotope fractionations

Unlike whole-rock analyses, $\delta^{44}Ca$ in mineral separates from individual rock samples have only been reported in a limited number of studies (Antonelli et al., 2019c, 2019b; Bessey, 2018; Chen et al., 2019b, 2018; Dai et al., 2020; S. Huang et al., 2010; Kang et al., 2019, 2016; Ryu et al., 2011; Simon and DePaolo, 2010; Skulan et al., 1997; Wang et al., 2019; Zhao et al., 2017) several of which analyze only one or two samples. In the following sections, we compare inter-mineral $\Delta^{44}Ca$ measurements from igneous and metamorphic rocks to those predicted by ab-initio estimates at relevant temperatures.

We generally find that predictions and measurements are often in disagreement. This observation suggests that inter-mineral Ca isotope fractionations are not likely to be reliable for geothermometry. Although experimental confirmation of the *ab-initio* predictions is still required, a recently published triple-isotope approach, which quantifies deviations from an equilibrium mass-law in $^{48}Ca/^{44}Ca$ *vs.* $^{42}Ca/^{44}Ca$ space (discussed in Section 5.2), suggests that they are approximately correct (Antonelli et al., 2019c). Thus, observed deviations from expected Ca isotope equilibrium are likely to be the result of kinetic effects in natural samples.

4.1. Igneous minerals

Mineral separates from ultramafic to felsic igneous rocks have a measured $\delta^{44}Ca_{BSE}$ range of -1.2 to +1.3‰ (Fig. 7a) (Antonelli et al., 2019b; Chen et al., 2019b, 2018; S. Huang et al., 2010; Kang et al., 2016; Ryu et al., 2011; Simon and DePaolo, 2010; Skulan et al., 1997; Zhao et al., 2017) . Orthopyroxene separates from ultramafic rocks tend to have the highest $\delta^{44}Ca$, but are highly variable and span the entire range observed in igneous minerals (~2.5‰). In mafic to

29

felsic rocks there is a smaller δ^{44}Ca range (~1‰), where plagioclase has the lowest δ^{44}Ca (but is

found to vary by ~0.5‰) and where ferromagnesian minerals (*e.g.* clinopyroxene, hornblende,

chlorite, epidote, biotite) are generally heavier than non-ferromagnesian minerals (*e.g.*

plagioclase, K-feldspar, melilite, apatite, titanite). Biotite has the most positive measured δ^{44}Ca

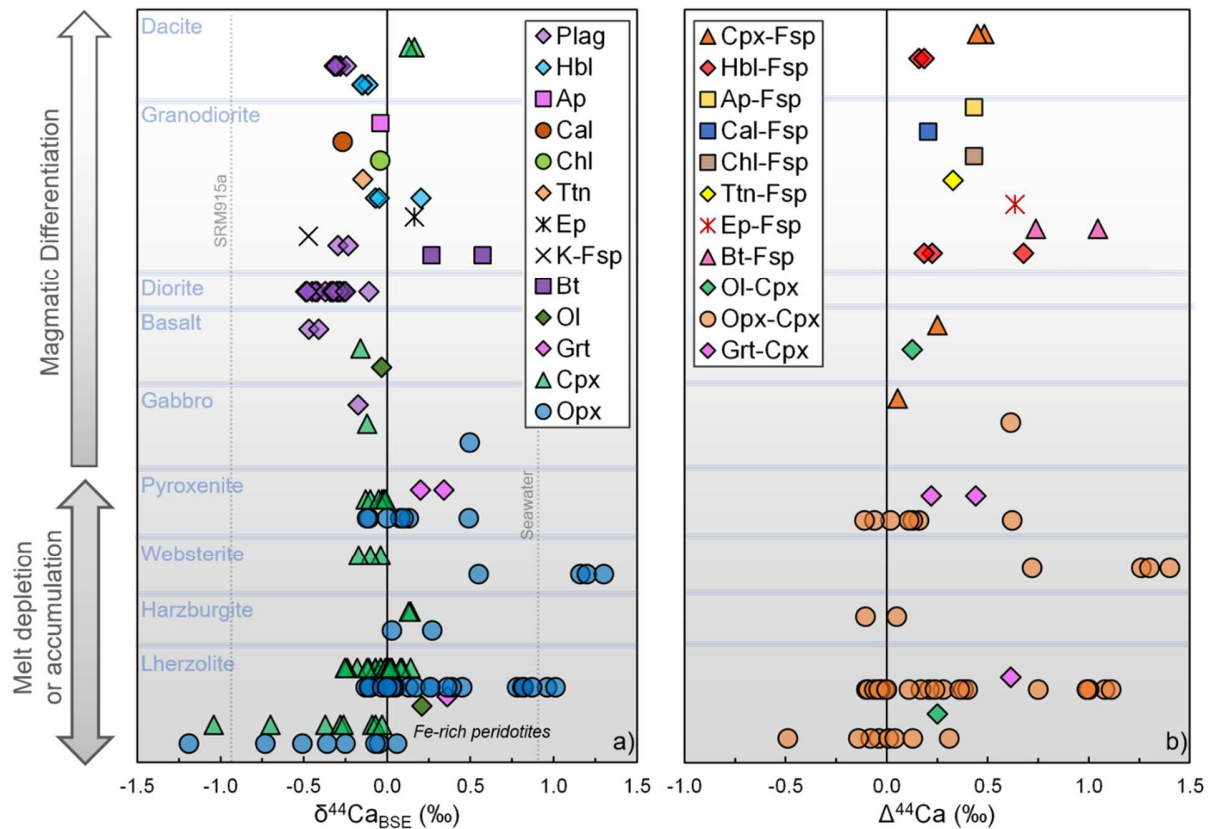out of these minerals, but has only been analyzed in one sample (Ryu et al., 2011).

Fig. 7a,b. Ca isotope compositions in igneous minerals (n = 146), grouped by rock type. **(a)** measured δ^{44}Ca in mineral separates, and **(b)** measured inter-mineral Δ^{44}Ca (n = 69). Data are from (Antonelli et al., 2019b; Chen et al., 2019b, 2018; Dai et al., 2020; S. Huang et al., 2010; Kang et al., 2016; Ryu et al., 2011; Simon and DePaolo, 2010; Skulan et al., 1997; Wang et al., 2019; Zhao et al., 2017), Fe-rich peridotite data, which are especially low in δ^{44}Ca, are from Zhao et al. (2017).

Inter-mineral Δ^{44}Ca values in igneous rocks span a range of ~2‰ (Fig. 7b). In mafic to felsic

rocks, all ferromagnesian minerals have higher δ^{44}Ca than coexisting feldspars (Δ^{44}Ca$_{min-fsp}$ up to

30

560 +1‰). The largest inter-mineral fractionations ($\Delta^{44}Ca_{opx-cpx}$ up to +1.5‰) are observed between

561 orthopyroxene and clinopyroxene. In most rocks $\Delta^{44}Ca_{opx-cpx}$ is positive, but a growing number of

562 samples have negative $\Delta^{44}Ca_{opx-cpx}$ (down to -0.5‰). To date, all analyzed clinopyroxene-

563 orthopyroxene pairs in websterites are out of Ca isotopic equilibrium, with orthopyroxene too

564 heavy, and all analyzed harzburgites, Fe-rich lherzolites, and a significant number of

565 pyroxenites, are out of isotopic equilibrium with orthopyroxene too light (Fig. 8a). Due to the

566 much higher concentration of Ca in clinopyroxene, however, imperfect mineral separations may

567 push orthopyroxene $\delta^{44}Ca$ towards the 1:1 line, and great care should be taken in future studies,

568 including verification of Ca concentrations in mineral separates [which can then be used for

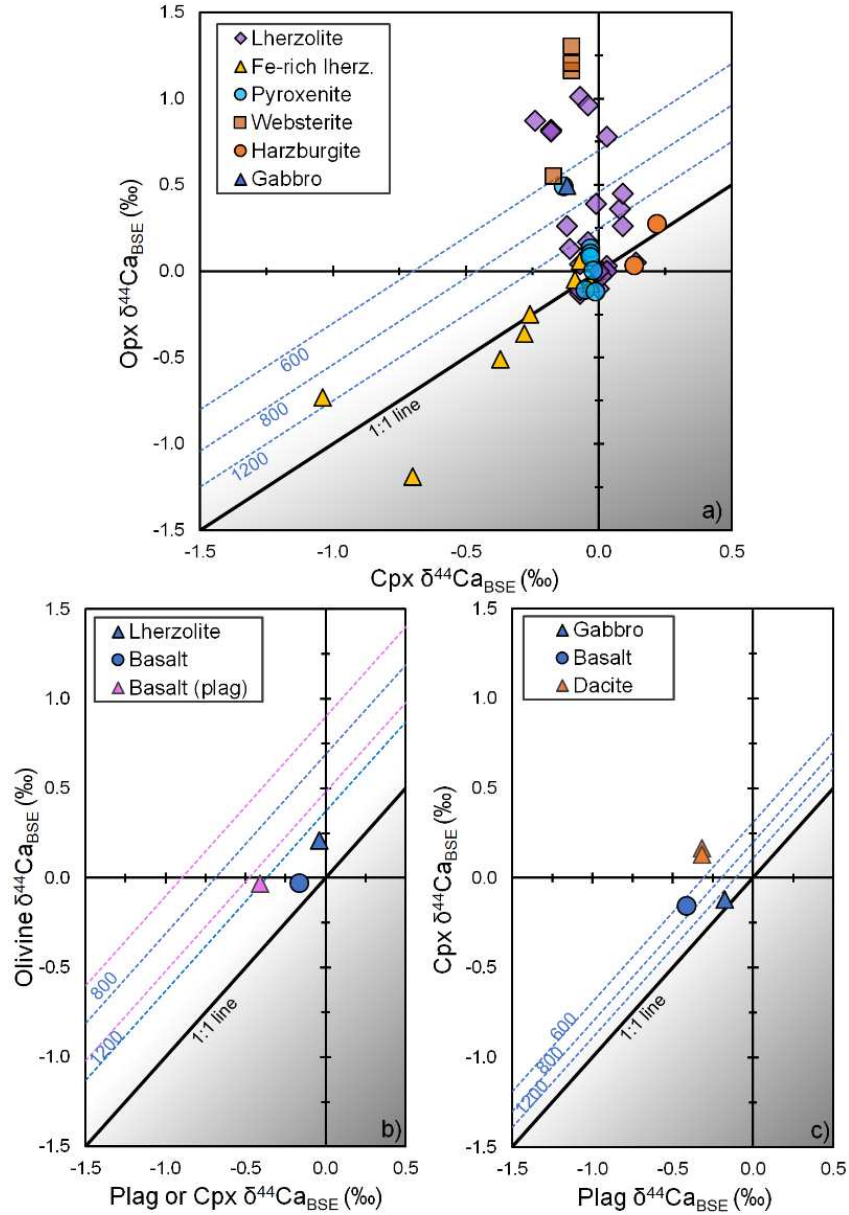569 eventual unmixing calculations *e.g.* (Antonelli et al., 2019c)].

570

Fig. 8a-c. Mineral-specific δ^{44}Ca measurements in igneous rocks (grouped by rock-type) compared with equilibrium ab-inito predictions at various temperatures (in degrees Celsius). **(a)** δ^{44}Ca$_{opx}$ *vs.* δ^{44}Ca$_{cpx}$ (n = 47), **(b)** δ^{44}Ca$_{ol}$ *vs.* δ^{44}Ca$_{cpx}$ (or δ^{44}Ca$_{plag}$) (n = 3), and **(c)** δ^{44}Ca$_{cpx}$ *vs.* δ^{44}Ca$_{plag}$ (n = 4). Data are from (Antonelli et al., 2019b; Chen et al., 2019b, 2018; Dai et al., 2020; S. Huang et al., 2010; Kang et al., 2016; Ryu et al., 2011; Simon and DePaolo, 2010; Skulan et al., 1997; Zhao et al., 2017). Ab-initio estimates for diopside, anorthite, orthopyroxene, and olivine are based on DFT estimates using PBE functionals (Antonelli et al., 2019c) and the lowest-Ca end-members for orthopyroxene and olivine.

578   Comparing the inter-mineral $\Delta^{44}Ca$ data to *ab-initio* predictions, we find that a significant

579   number of analyses do not agree with predictions at relevant temperatures. Additionally, a

580   significant number of samples have negative $\Delta^{44}Ca_{opx-cpx}$ (below the 1:1 line, Fig. 8a) that are not

581   predicted at any temperature. The few analyzed $\Delta^{44}Ca_{ol-plag}$ and $\Delta^{44}Ca_{ol-cpx}$ fractionations are

582   much smaller than expected for relevant temperatures in peridotites and gabbros (Fig. 8b). A

583   small number of $\Delta^{44}Ca_{cpx-plag}$ in basalts and gabbros, however, are in approximate agreement

584   with predictions, but have much larger relative uncertainties (Fig. 8c), while the clinopyroxene-

585   plagioclase fractionation in a dacitic volcanic rock is found to be significantly larger than

586   expected (as a likely consequence of rapid plagioclase growth, discussed in Section 6.3).

587   Although a negative correlation is observed between Ca concentrations in orthopyroxene and

588    $\Delta^{44}Ca_{opx-cpx}$ in igneous rocks (which is in the same direction as expected from dilution effects),

589   the observed effects are greater than equilibrium predictions at relevant temperatures, and Ca

590   dilution effects are negligible for the analyzed range of orthopyroxene Ca/(Ca+Mg).

591   The Ca concentration in orthopyroxene, however, is known to increase with increasing

592   temperature (Brey and Kohler, 1990), and is commonly used as a geothermometer ('Ca-in-Opx

593   thermometry'). Thus, increased Ca contents in orthopyroxene should lead to smaller

594   fractionations not only due to (i) increasing average Ca-O bond lengths with increasing Ca, but

595   also due to (ii) decreasing equilibrium isotope fractionations with increasing temperatures.

596   Neither of these effects, however, can explain the range of observed data, which suggests that

597   orthopyroxene-clinopyroxene mineral pairs are often out of isotopic equilibrium and that the

598   rough inverse correlation between Ca in orthopyroxene and $\Delta^{44}Ca_{opx-cpx}$ (Chen et al., 2019b) is

599   likely due to disequilibrium effects (discussed in Section 6.2).

600   **4.2. Metamorphic minerals**

601   Ca isotope variability in metamorphic minerals is even larger than observed in igneous minerals,

602   with a $\delta^{44}Ca_{BSE}$ range of ~8‰ (-2.2 to +5.8‰, Fig. 9a), but minerals from only three

603   metamorphic-facies (amphibolite, eclogite, and granulite-facies), have been analyzed in a total of

604   only four studies (Antonelli et al., 2019c; Bessey, 2018; Kang et al., 2019; Wang et al., 2019).

605   Mineral $\delta^{44}Ca$ compositions in granulites are the most variable, with a $\delta^{44}Ca$ range of ~3‰ in

606   garnet, ~6‰ in orthopyroxene, ~5‰ in plagioclase, and ~2.5‰ in perthitic K-feldspar. The only

607   mineral with a relatively limited $\delta^{44}Ca$ range (< 0.5‰) is clinopyroxene, which appears to always

608   have Ca isotope compositions close to BSE. In lower temperature metamorphic facies (eclogite

609   and amphibolite), $\delta^{44}Ca$ variability is more limited in all minerals, observed to be within ~1‰ of

610   BSE (Fig. 9a).

611   Inter-mineral $\Delta^{44}Ca$ values are the largest in granulite-facies rocks, ranging from -2 to +2.5‰

612   (Fig.9b), but can be highly variable for a given mineral pair (*e.g.* $\Delta^{44}Ca_{grt-fsp}$ ranges from -1.5 to

613   +1.5 and $\Delta^{44}Ca_{opx-fsp}$ ranges from 0.0 to +2.5‰). In amphibolite- and eclogite-facies rocks, inter-

614   mineral $\Delta^{44}Ca$ values range from -0.5 to +1‰. The most negative $\Delta^{44}Ca$ fractionation in these

615   rocks is for an apatite-clinopyroxene pair from an eclogite sample, while the most positive values

616   are for garnet-apatite, garnet-calcite, and garnet-clinopyroxene. Note that these statements are

617   somewhat definitional, such that the most positive $\Delta^{44}Ca$ values would be the most negative if

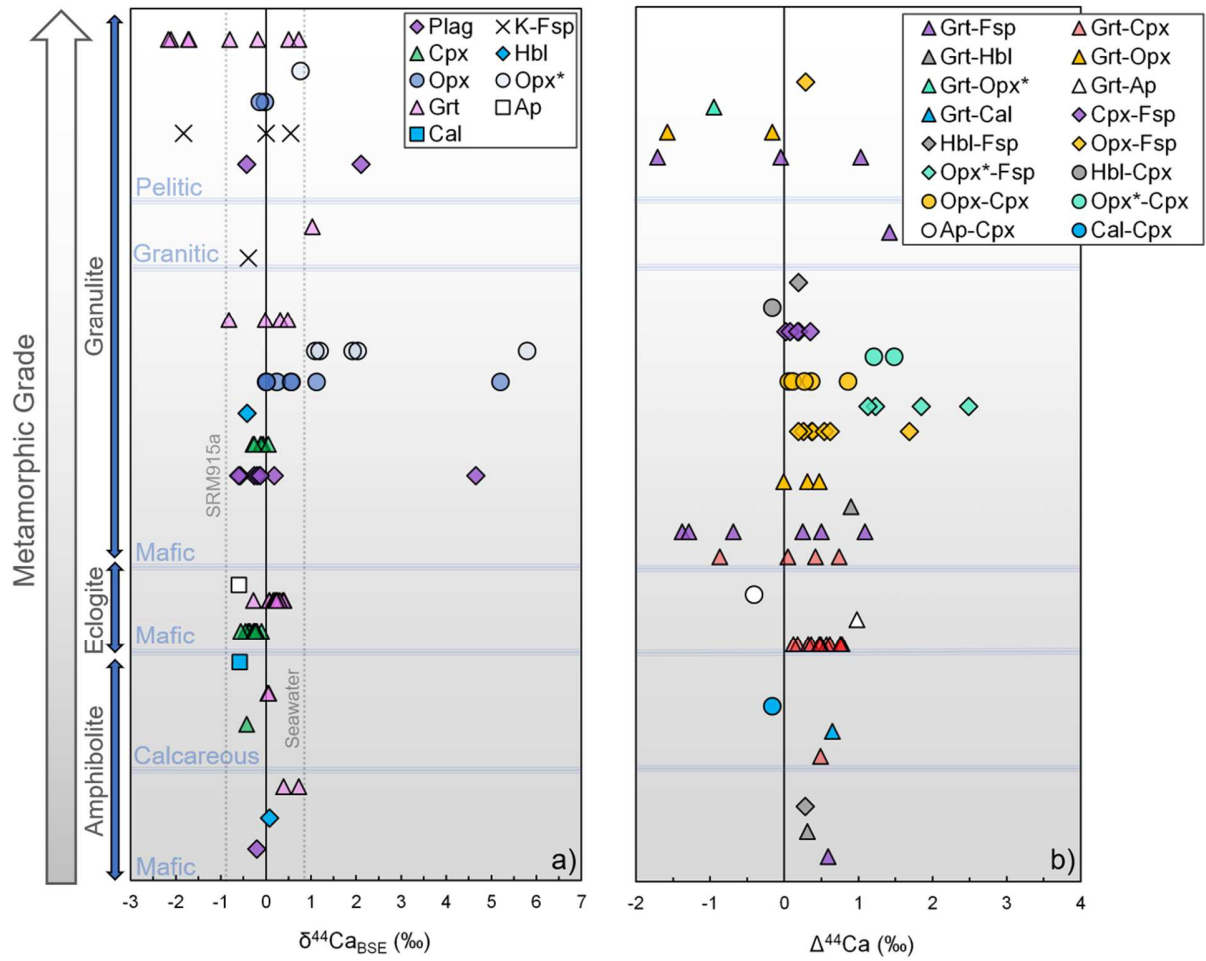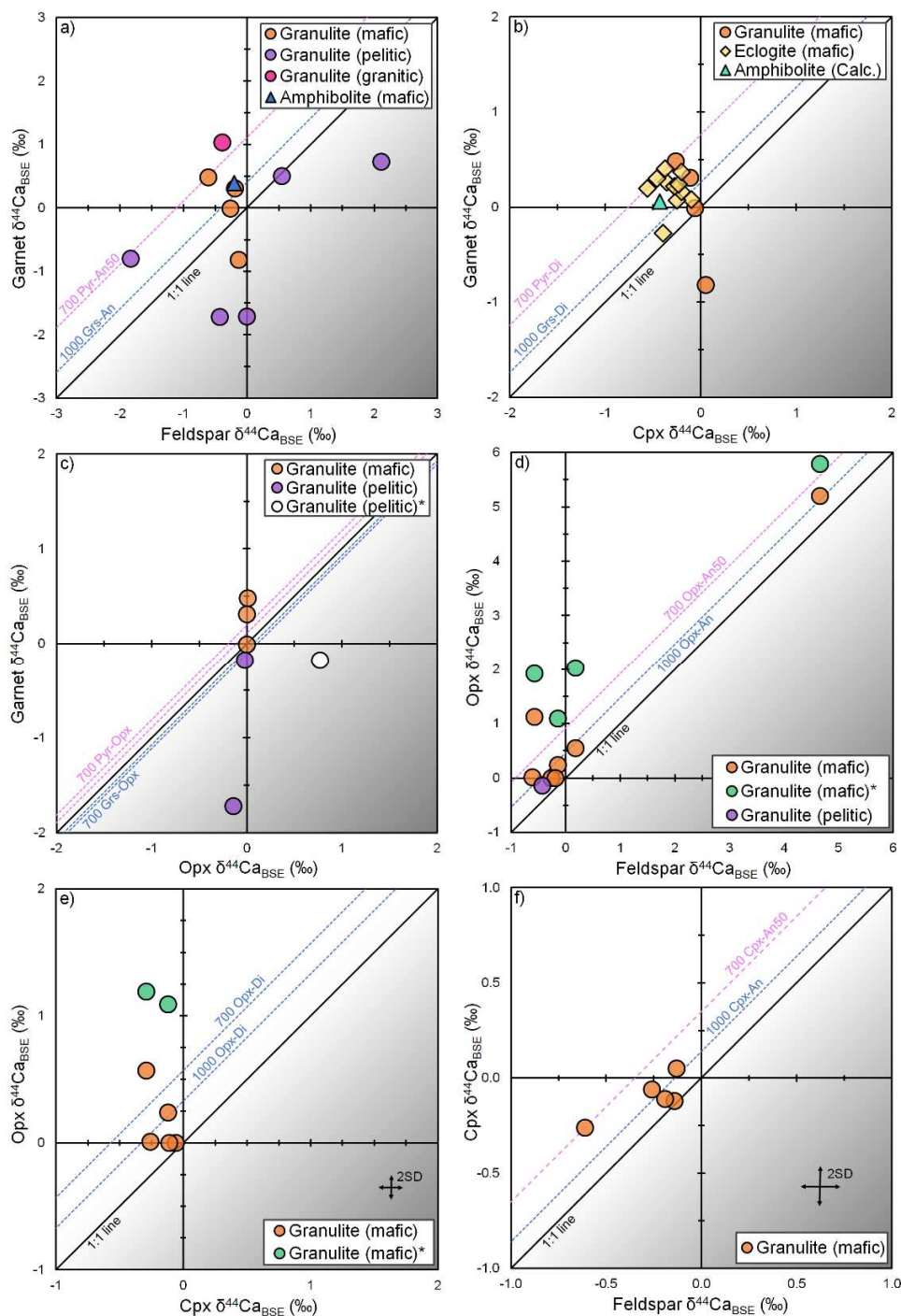618   defined in the opposite sense (*i.e.* $\Delta^{44}Ca_{ap-grt}$ instead of $\Delta^{44}Ca_{grt-ap}$).

Fig. 9a,b. Ca isotope variations in metamorphic minerals, grouped by metamorphic-facies and protolith composition. **(a)** $\delta^{44}Ca_{BSE}$ of metamorphic mineral separates (n = 81) and **(b)** inter-mineral Ca isotope differences ($\Delta^{44}Ca$) in metamorphic rocks (n = 66). Triangles correspond to $\Delta^{44}Ca_{grt-min}$, diamonds correspond to $\Delta^{44}Ca_{min-fsp}$, and circles correspond to $\Delta^{44}Ca_{min-cpx}$. Approximate 2sd uncertainties for $\delta^{44}Ca$ are ±0.1‰. Opx* corresponds to pure orthopyroxene estimates from unmixing calculations which can have variable uncertainties based on the unmixing parameters [average 2sd of ~0.5‰ (Antonelli et al., 2019c)]. Data are from (Antonelli et al., 2019c; Bessey, 2018; Kang et al., 2019; Wang et al., 2019).

Comparing the measured inter-mineral $\Delta^{44}Ca$ values to ab-initio predictions at relevant temperatures (Fig. 10), we find — similar to the igneous mineral pairs— that many represent isotopic disequilibrium. Garnet-mineral pairs in granulite-facies rocks are found to deviate

630 furthest from ab-inito equilibrium predictions, with minerals from pelitic granulites having the

631 greatest apparent disequilibrium effects, while lower-grade metamorphic garnet-mineral

632 fractionations are closer to equilibrium predictions. Orthopyroxene-mineral fractionations in

633 granulite-facies rocks also tend to suggest isotopic disequilibrium, with orthopyroxene $\delta^{44}Ca$

634 compositions either too negative or too positive compared to predictions at relevant temperatures

635 (Fig. 10c-e). Clinopyroxene-plagioclase fractionations, however, are in approximate agreement

636 with equilibrium predictions, similar to observations from igneous mineral pairs. Indeed, the

637 largest inter-mineral disequilibrium effects observed in granulite-facies rocks appear to be

638 limited to rocks with less than ~15% modal clinopyroxene (Antonelli et al., 2019c). When

639 clinopyroxene is present, the observed inter-mineral fractionations tend to better agree with

640 equilibrium predictions, and thus, mafic (*vs.* pelitic) granulites tend to have fractionations closer

641 to equilibrium. This could be a potential manifestation of (i) protolith-based differences in

642 diffusive transport/paragenetic processes or may suggest that (ii) isotopic heterogeneities in

643 pelitic precursor minerals are somehow carried over (discussed in Section 6.2).

644 It appears that the magnitude of disequilibrium effects increases with increasing temperatures in

645 granulite-facies rocks, potentially due to the activation of otherwise subordinate diffusion

646 pathways/mechanisms (Antonelli et al., 2019c). Garnet-mineral and garnet-whole-rock (WR)

647 fractionations deviate further from equilibrium predictions with increasing WR and garnet Mg#

648 (Fig. 11), and orthopyroxene-mineral fractionations increasingly deviate from equilibrium

649 predictions with WR Mg#, feldspar anorthite component, modal orthopyroxene, and

650 orthopyroxene Ca/Mg, all of which tend to increase with temperature (Antonelli et al., 2019c).

651 The trend of increasing $\Delta^{44}Ca_{opx\text{-}min}$ with increasing orthopyroxene Ca/Mg, however, is the

652 opposite of that observed in mantle mineral separates, suggesting a different underlying

653 mechanism for the disequilibrium fractionations.

654

Fig. 10a-f. Ca isotope cross-plots for minerals from metamorphic rocks, grouped by rock-type, with temperature contours representing ab-initio equilibrium predictions from DFT estimates. Garnet-mineral predictions depend on the garnet end-member chosen, with pyrope having the highest predicted 1000lnβ and grossular having the lowest 1000lnβ. In order to represent the full range of fractionations expected at equilibrium, we report grossular-mineral predictions at high temperatures (1000°C) and pyrope-mineral predictions at lower temperatures (700°C). We also chose a similar approach for feldspar predictions, where mineral-anorthite is reported at high temperatures and mineral-labradorite (An50) are reported at lower temperatures. **(a)** $\delta^{44}Ca_{grt}$ *vs.* $\delta^{44}Ca_{fsp}$ (n = 11), **(b)** $\delta^{44}Ca_{grt}$ *vs.* $\delta^{44}Ca_{cpx}$ (n = 16), **(c)** $\delta^{44}Ca_{grt}$ *vs.* $\delta^{44}Ca_{opx}$ (n = 6), **(d)** $\delta^{44}Ca_{opx}$ *vs.* $\delta^{44}Ca_{fsp}$ (n = 12), **(e)** $\delta^{44}Ca_{opx}$ *vs.* $\delta^{44}Ca_{cpx}$ (n = 7), **(f)** $\delta^{44}Ca_{cpx}$ *vs.* $\delta^{44}Ca_{fsp}$ (n = 5). Asterisk (*) denotes unmixed orthopyroxene $\delta^{44}Ca$ estimates. DFT predictions are based on PBE functionals (Antonelli et al., 2019c). Data are from (Antonelli et al., 2019c; Bessey, 2018; Kang et al., 2019; Wang et al., 2019). Average 2sd uncertainties for $\delta^{44}Ca$ (~ ±0.1‰) are smaller than the symbols except for in panels (e) and (f) where they are depicted in the lower right-hand corner.
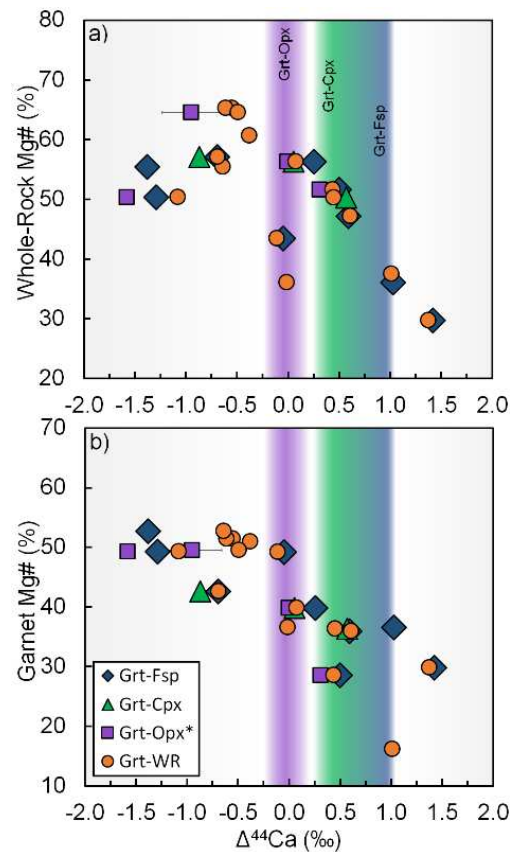
668 **Fig. 11a,b.** Whole-rock and mineral composition controls on Δ^{44}Ca in eclogite, amphibolite, and granulite-facies

669 rocks after Antonelli et al. (2019c). Garnet-mineral and garnet-whole rock Δ^{44}Ca versus **(a)** whole rock Mg# and **(b)**

670 garnet Mg#. Error bars are generally smaller than the symbols. Colored bands indicate predicted equilibrium at 800-

671 900 °C from ab-initio estimates (Antonelli et al., 2019c): Grt-Opx (purple), Grt-Cpx (green), Grt-Fsp (blue).

672 Orthopyroxene predictions are based on Ca:Mg of 1:63.

673 In sum, inter-mineral Δ^{44}Ca variability in igneous and metamorphic rocks suggests that kinetic

674 effects occur (and are subsequently preserved) at high-temperatures, however, the quantification

675 of these effects relies mainly on the accuracy of *ab-initio* predictions for equilibrium

676 fractionation and may be limited by various model assumptions. Although no experimental

677 constraints are yet available for equilibrium Ca isotope fractionation (and represent important

678 targets for future work), equilibrium and kinetic effects can potentially be distinguished using a

679 triple-isotope approach (Antonelli et al., 2019c).

680 **5. Distinguishing kinetic from equilibrium fractionations**

681 The accurate quantification of equilibrium *vs.* kinetic effects and their applicability in different

682 high-temperature systems is of paramount importance to Ca isotope geochemistry. This is

683 because isotope fractionation factors are necessary inputs for most models (*e.g.* partial melting,

684 crystallization, & diffusion models) that attempt to quantify high-temperature phenomena using

685 δ^{44}Ca and Δ^{44}Ca data. Extents of melting and fractional crystallization based on Ca isotopes, for

686 example, are often calibrated by either (i) assuming isotopic equilibrium (*i.e.* fractionation

687 factors based on DFT models), or (ii) measuring inter-mineral Δ^{44}Ca in coexisting minerals and

688 assuming that these correspond to all of the fractionations occurring in a system. Both of these

689 approaches have their own limitations, with the first approach assuming that DFT models are

690 accurate for natural systems and that the various processes are happening at isotopic equilibrium,

691 and the second approach assuming that, whether or not the fractionations are at equilibrium, that

692 Δ^{44}Ca is invariable in the system.

693 **5.1. Chemical *vs*. isotopic equilibrium**

694 Various lines of reasoning are often used in order to defend the applicability of equilibrium

695 fractionation factors derived from DFT and/or to suggest that measured δ^{44}Ca values are

696 representative of isotopic equilibrium. These include observations of: (i) textural equilibrium

697 and/or grain homogeneity, (ii) chemical equilibrium between minerals, paired with assumptions

698 about the relative rates for isotopic *vs*. chemical equilibration, and/or (iii) assumptions regarding

699 short length-scales for Ca diffusion (*e.g.* closed-system for Ca at the hand-sample scale). There

700 are several issues with these approaches, however, with the most significant being that, for a

701 given element – *chemical-equilibrium is not a sufficient condition for isotopic equilibrium.*

702 Potential confusion surrounding the relationship between isotopic and chemical equilibrium

703 comes from the high-temperature experimental community, where the word *equilibrate* is used

704 in the sense of *isotopic homogenization* across experimental diffusion couples (Baker, 1989;

705 Laan et al., 1994; Lesher, 1994, 1990; Watkins et al., 2011), and not in the sense of free-energy

706 minimization. In these diffusion experiments, it is observed that the initial pulse of isotopic

707 fractionation (where ^{40}Ca diffuses faster than ^{44}Ca, discussed in Section 6) levels out faster than

708 the chemical concentration gradient between the two starting materials (F. Huang et al., 2010;

709 Richter et al., 2009, 2003, 1999; Watkins et al., 2017, 2014, 2011, 2009). Thus, a not uncommon

710 statement from these types of studies is that isotopic equilibration occurs faster than chemical

711 equilibration*,* which has been taken at face value and used in several Ca isotope studies claiming

712 isotopic equilibrium.

713   The thermodynamic drive for chemical reactions is several orders of magnitude larger than for

714   isotopic substitution reactions (*e.g.* Chacko et al., 2001). In order to minimize free energy in a

715   system, therefore, isotopic equilibration is largely subordinate to chemical equilibration.

716   Maintaining isotopic equilibrium during an ongoing chemical reaction depends mainly on the

717   forward and backward exchange rates greatly exceeding the overall net reaction rate (DePaolo,

718   2011). Although one can envision a case where the net chemical reaction rate is so slow that the

719   forward and backward exchange rates at the crystal surface are much larger (*e.g.* extremely slow

720   carbonate precipitation), and could thus potentially maintain near isotopic equilibrium

721   throughout the reaction, this is unlikely to apply in a majority of cases (DePaolo, 2011). As noted

722   by many early experimental studies (*e.g.* Clayton, 1959; Matsuhisa et al., 1978; Matthews, 1976;

723   O'Neil and Taylor, 1969, 1967), mineral-synthesis, phase-change, and ion-exchange reactions

724   are susceptible to kinetic isotope effects that are not likely to reach subsequent isotopic

725   equilibrium, even over extended time-scales.

726   Ca isotope measurements in natural samples also suggest that chemical equilibrium generally

727   precedes isotopic equilibrium, even at high temperatures. For Ca isotopes in granulite-facies

728   metamorphic rocks, it has been shown that significant inter-mineral Δ^{44}Ca disequilibrium can

729   still exist, even when held at high-temperatures (~900°C) over extended time periods (10^7-10^8

730   years) and when Fe-Mg exchange and Ca-in-Opx thermometry indicate approximate chemical

731   equilibrium (Antonelli et al., 2019c). These authors also observe chemical homogeneity across

732   mineral grains (*e.g.* garnet) and equilibrium (granoblastic) textures in many samples, indicating

733   that neither of these conditions are sufficient for Ca isotopic equilibrium.

734   Ca isotope distributions were also explored in samples from the Guelb el Azib Complex (a mafic

735   intrusion metamorphosed to granulite-facies and subsequently retrograded through amphibolite

736 and greenschist-facies), where mineral-specific δ^{44}Ca values were estimated based on Monte

737 Carlo simulations [combining whole-rock and mineral chemical compositions, whole-rock δ^{44}Ca,

738 and modal mineralogy estimates (Valdes et al., 2019)]. Although not explicitly discussed by the

739 authors, the development and preservation of disequilibrium isotopic compositions is evidenced

740 by the large δ^{44}Ca variations (up to ~ 3‰) estimated for the same mineral phases (*e.g.*

741 amphibole, plagioclase) with otherwise similar chemical compositions across different samples.

742 Finally, the assumption that Ca isotopes behave as a closed-system on the hand-sample scale

743 during high-temperature metamorphism, used in order to look-through potential metamorphic

744 effects and quantify Ca isotope fractionation during fractional crystallization (Valdes et al.,

745 2019), is in disagreement with results from spatially-constrained granulite-facies samples that

746 suggest diffusive Ca isotope fractionation can occur over several meters during metamorphism

747 (Antonelli et al., 2019c). Ca diffusion in high-temperature systems with greater volatile element

748 concentrations (and higher Ca diffusivities) could thus occur over even greater distances, given

749 sufficiently large timescales.

750 **5.2. The triple Ca isotope method (Δ^{48}Ca')**

751 Although no experimental constraints are available, in order to confirm ab-initio predictions, a

752 recent study has exploited the predicted differences between kinetic and equilibrium mass-

753 fractionation laws in order to (i) corroborate DFT estimates and (ii) confirm the kinetic origins of

754 large (>1‰) fractionations in high-temperature whole-rocks and minerals (Antonelli et al.,

755 2019c). In triple isotope space (^{48}Ca/^{44}Ca *vs.* ^{42}Ca/^{44}Ca) the predicted equilibrium mass law,

756 based on vibrational frequency differences, is -1.751 (*e.g.* Young et al., 2002). This means that

757 measured ^{48}Ca/^{44}Ca should be equal to the measured ^{42}Ca/^{44}Ca to the exponent of -1.751, if

758 fractionation occurred at equilibrium. The kinetic limit, based on diffusion in an ideal gas

759 (Graham's Law), where the average speed of an isotope is inversely proportional to its mass,

760 leads to a predicted $^{48}Ca/^{44}Ca$ that is related to $^{42}Ca/^{44}Ca$ by the exponent -1.872. Thus, the

761 effects of equilibrium *vs.* kinetic fractionations should be distinguishable by measuring $^{48}Ca/^{44}Ca$

762 and comparing to $^{42}Ca/^{44}Ca$. Although ^{42}Ca-^{44}Ca-^{48}Ca were used in this study due to their large

763 relative mass differences, any combination of three Ca isotopes could theoretically be used in

764 order to quantify deviations from an equilibrium mass law. The authors define a new variable

765 ($\Delta^{48}Ca'$) which quantifies $^{48}Ca/^{44}Ca$ deviations from isotopic equilibrium (in ppm):

766 $$\Delta^{48}Ca' = \mu^{48}Ca - [(\mu^{42}Ca + 1)^{-1.751} - 1] \qquad \text{(Eq. 3)}$$

767 Where $\mu^{4x}Ca$ is defined as $[(^{4x}Ca/^{44}Ca)_{sample}/(^{4x}Ca/^{44}Ca)_{standard} - 1]$ and reported in ppm. A

768 similar triple-isotope method has also been used to distinguish kinetic from equilibrium

769 fractionations for Mg and Fe isotopes (McCoy-West et al., 2018; Olsen et al., 2013; Young and

770 Galy, 2004).

771 In order to test this method, two end-member samples were initially analyzed (Antonelli et al.,

772 2019c). The kinetic end-member sample comes from rapid plagioclase crystallization in an

773 experimental tonalite sample [also investigated in (Antonelli et al., 2019b)], where plagioclase

774 and melt have a $\Delta^{44}Ca$ difference greater than 2‰. The equilibrium end-member samples

775 (plagioclase and orthopyroxene mineral separates) were taken from the Stillwater cumulate

776 gabbro, which slowly crystallized over 10-100 Ka (DePaolo and Wasserburg, 1979). In Fig. 12,

777 these end-member samples are demarcated with arrows, and can be seen to closely adhere to the

778 mass-laws predicted by the equilibrium and kinetic limits for isotope fractionation: the Stillwater

779 gabbro sample has no $\Delta^{48}Ca'$ difference between minerals, whereas plagioclase from the

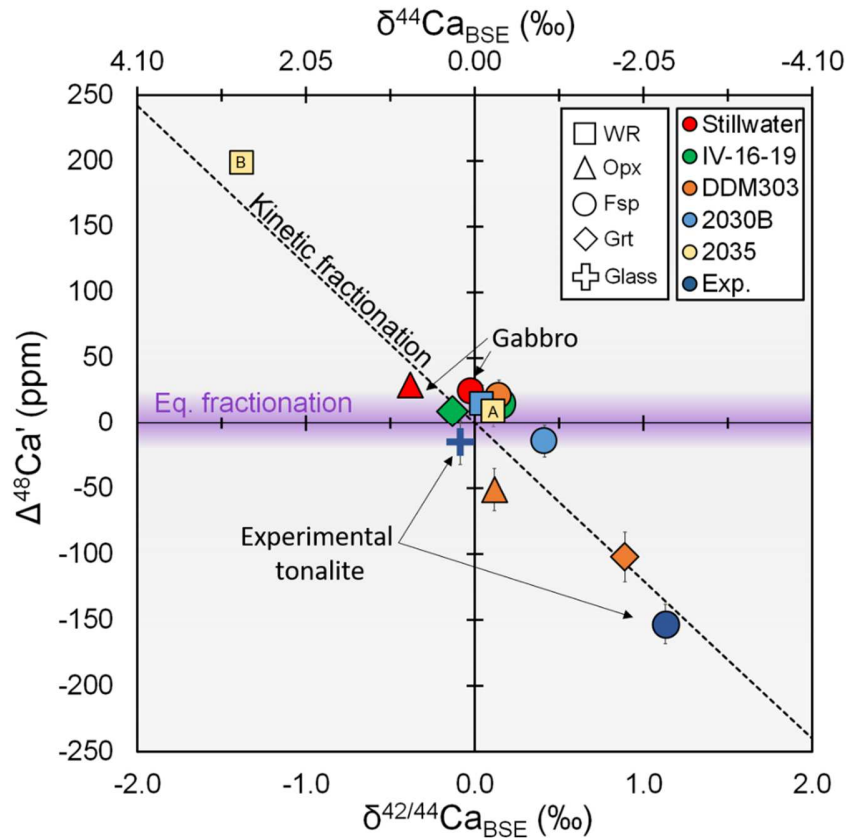780 experimental tonalite sample has a large $\Delta^{48}Ca'$ depletion relative to glass.

781

Fig. 12. Triple Ca isotope compositions (Δ^{48}Ca' vs. $\delta^{42/44}$Ca$_{BSE}$) for granulite-facies whole rocks (and minerals) from Diavik, Ivrea, and the Napier Complex, and for an experimental tonalite and cumulate gabbro sample, modified from (Antonelli et al., 2019c). The shaded purple region demarcates the compositional field that would be expected for a bulk-silicate Earth material that has not undergone any kinetic fractionations (taking into account the average uncertainty of the MC-ICP-MS measurements), but it is the difference in Δ^{48}Ca' between two phases that defines whether or not they are at isotopic equilibrium. Cumulate gabbro from the Stillwater complex exemplifies this relationship between orthopyroxene and plagioclase, whereas samples with large differences (such as plagioclase and glass from the experimental tonalite and adjacent whole-rocks 2035A and 2035B, which represent the center and edge, respectively, of a metamorphosed granulite-facies mafic dike hosted in quartzitic country rock) clearly depict the effects of kinetic fractionation and also serve to reinforce the applicability of the theoretically-predicted kinetic mass-law (dotted line). 2σ error bars correspond to 2SE of repeat analyses on the same sample and are smaller than the symbols for a majority of the samples. δ^{44}Ca$_{BSE}$ values are provided for reference at the top of the figure.

795   The other data in Fig. 12 correspond to various granulite-facies rocks and minerals. The largest

796   positive Δ^{48}Ca' fractionation is between the center (2035A) and edge (2035B) of a

797   metamorphosed ultramafic dike sample from the Napier complex (Antonelli et al., 2019c), which

798   also follows the trend predicted by the kinetic limit for isotope fractionation (yellow squares

799   labeled 'A' and 'B'). Inter-mineral separates from granulite-facies samples with large Δ^{44}Ca

800   differences (including Slave-province xenoliths and Napier complex samples) are also in general

801   agreement with the kinetic limit for mass fractionation. This may be surprising at first, because

802   the kinetic-limit is predicted from diffusion in an ideal gas, however, this simply implies that the

803   mass-law [typically referred to as the exponent 'β' (*e.g.* Richter et al., 1999), but not to be

804   confused with reduced partition function ratios (1000lnβ) from *ab-initio* estimates] is essentially

805   the same for ^{48}Ca/^{44}Ca and ^{42}Ca/^{44}Ca. Although only a limited number of samples have been

806   analyzed, the two samples which best agree with equilibrium *ab-initio* predictions

807   [orthopyroxene and plagioclase from the Stillwater gabbro, along with garnet and feldspar from a

808   lower-crustal garnet amphibolite ('IV-16-19')] have equilibrium Δ^{48}Ca' values (Fig. 12). In the

809   absence of experimental data, this observation lends weight to the applicability of currently

810   available DFT estimates for estimating Ca isotopic equilibria between minerals (*e.g.* Antonelli et

811   al., 2019c; Huang et al., 2019; Wang et al., 2017b).

812   The triple Ca-isotope method may also allow for the separation of equilibrium and kinetic

813   fractionations in the same sample. As can be seen, for example, in the Stillwater gabbro mineral

814   separates (Fig. 12), despite having the same Δ^{48}Ca' values (equilibrium between the minerals),

815   there is a slight offset between these and bulk silicate earth (Δ^{48}Ca' = 0). This implies that the

816   parent material may have undergone kinetic fractionations, before subsequent isotopic re-

817   equilibration. Given the difficulty of precisely measuring Δ^{48}Ca', however, the possibility of

818 distinguishing kinetic fractionations that underwent subsequent equilibrium fractionation (or vice

819 versa) remains to be explored in future work. Although unequivocal confirmation of the kinetic

820 mass-dependence for fractionations between minerals (and adjacent whole-rocks) was

821 accomplished by analyzing samples with large δ^{44}Ca differences (up to ~3‰) and by targeting

822 multiple Ca isotopes with the largest mass differences (Antonelli et al., 2019c), an earlier study

823 used unspiked TIMS measurements (corrected with an exponential mass-law) on metasomatized

824 peridotite mineral separates and showed that there were no ^{40}Ca/^{44}Ca anomalies (Zhao et al.,

825 2017), which, although lacking the necessary precision to confirm a specific mass law, strongly

826 suggested a kinetic control on fractionation in these samples.

827 **6. Kinetic Ca isotope fractionation at high-temperatures**

828 In a general sense, isotopic rate differences for dominantly unidirectional reactions (*e.g.* rapid

829 crystal precipitation) are responsible for the large disequilibrium effects observed in δ^{44}Ca. These

830 kinetic fractionations can occur during transport of Ca isotopes towards a reaction locus, where

831 ^{40}Ca diffuses faster than ^{44}Ca, or from isotopic rate differences during bond formation (*e.g.* at a

832 precipitating crystal surface) or bond breaking (*e.g.* disruption of the hydration sphere around

833 Ca^{2+} ions in water). We refer the reader to DePaolo (2011), Simon (2017), Simon and DePaolo

834 (2010), and Watkins et al. (2017) where these topics are discussed in greater detail.

835 Of all the kinetic Ca isotope fractionations occurring in high-temperature terrestrial settings,

836 diffusive Ca transport has the largest δ^{44}Ca effects, which can be an order of magnitude larger

837 than equilibrium effects at similar temperatures (Watkins et al., 2017). Given the potential size of

838 the effects, modeling kinetic Ca isotope fractionation (although slightly more challenging than

839 modeling equilibrium fractionations) is often necessary in order to interpret δ^{44}Ca data from

840 natural samples.

841 In conjunction with kinetic fractionation models, $\delta^{44}Ca$ data can yield essential information on

842 chemical reaction rates (and durations) and on the nature of Ca transport in various geochemical

843 reservoirs throughout Earth's geologic past. In this section we briefly cover the principles behind

844 kinetic Ca isotope fractionations at high temperatures, and then explore the various models used

845 to gain information from isotopic disequilibria observed in natural samples. These include

846 models constraining: (i) the duration of mantle metasomatism events, (ii) Ca transport

847 mechanisms during high-temperature metamorphism in the lower continental crust, and (iii)

848 crystal growth-rates in volcanic and sub-volcanic systems.

849 **6.1. Ca diffusion in experimental silicate liquids**

850 During diffusion in an ideal gas, kinetic isotope effects can be essentially explained by classical

851 mechanics (based on differences in translational energies) and are due to the greater average

852 speeds of lighter isotopes (at a given kinetic energy). Within more complex diffusion media,

853 such as silicate melts, however, cation diffusion occurs by hopping between interstitial sites

854 (potential energy minima within the silicate framework), and can therefore be modeled using

855 transition-state theory (Dominguez et al., 2011). The difficulty of estimating the various

856 parameters needed to estimate kinetic isotope effects from transition-state theory, however, has

857 motivated a more empirical approach towards quantifying diffusive isotope fractionation in

858 silicate liquids (F. Huang et al., 2010; Richter et al., 2009, 2003, 1999; Watkins et al., 2017,
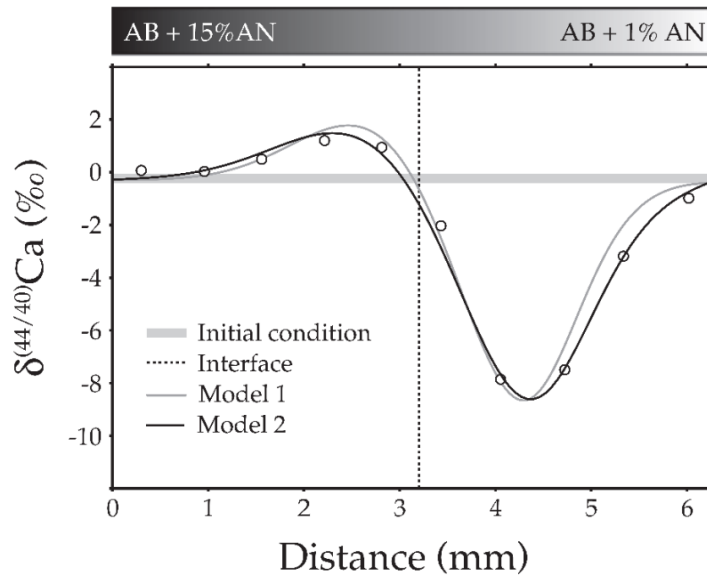
859 2014, 2011, 2009).

Fig. 13. Example of diffusion experiment results between high-An and low-An plagioclase melts at 1450°C, from (Watkins et al., 2011). The low-Ca side (right) experiences a temporary negative shift in $\delta^{44}Ca$ as the ^{40}Ca diffuses into it more quickly, while the high-Ca side (left) experiences a positive shift in $\delta^{44}Ca$ as the ^{44}Ca atoms are preferentially left behind. In a closed system, the isotopic deviations level out to zero once ^{44}Ca has had the time to 'catch up' with ^{40}Ca, which generally occurs before the Ca concentration gradients reach zero. In this example, the Ca isotopic fractionations are increased due to counter diffusion of Na.

Experiments using high-temperature diffusion couples have shown that Ca isotope fractionation in silicate liquids can occur during chemical diffusion, thermal diffusion ('Soret diffusion'), and even in the absence of chemical or thermal gradients ('isotopic self-diffusion') when the reactants differ only in their isotopic compositions. During chemical diffusion experiments, such as that shown in Fig. 13, the fractionation factor (often defined as the diffusivity of ^{44}Ca relative to ^{40}Ca, D_{44}/D_{40}) depends on a variety of parameters including: (i) the degree of melt polymerization (*e.g.* the diffusivity of Ca relative to that of the SiO_2 framework, as shown in Fig. 14a), where greater isotopic fractionations are correlated with higher $SiO_2 + Al_2O_3$ in the melt (Fig. 14b), (ii) the direction and strength of chemical gradients for other chemical species, where

48

876   counter-diffusion (*e.g.* of Na, as in Fig. 13) generally increases the Ca isotopic fractionation, and

877   (iii) the direction of thermal gradients imposed on the system, where heavier Ca isotopes are

878   favored at the colder end. A detailed review of the factors influencing isotopic fractionation

879   during diffusion in silicate liquids can be found in Watkins et al. (2017), and the reader is
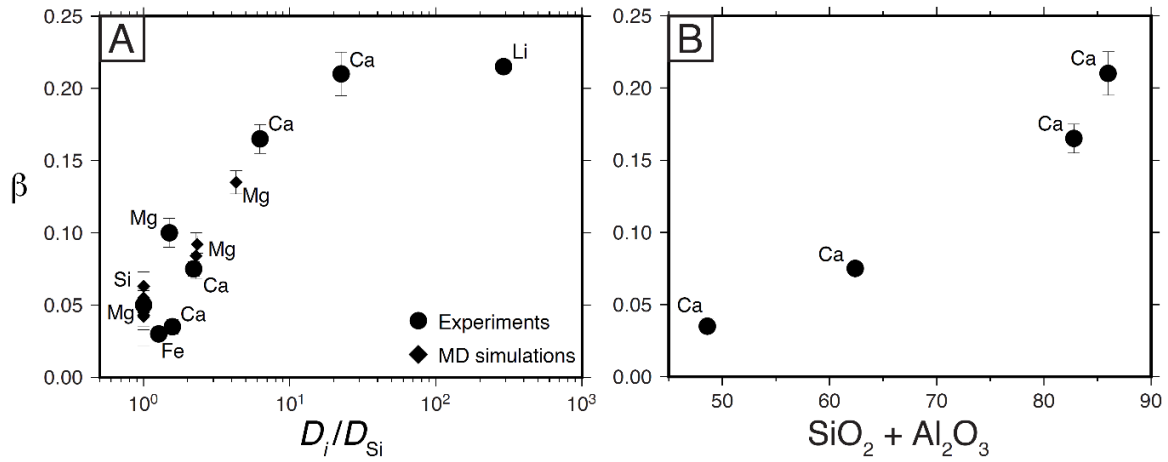
880   referred there for further information.

881

882   **Fig. 14a,b.** Experimental and molecular-dynamic simulation beta-factors versus **(a)** cation diffusivity relative to the

883   diffusivity of silicon (D_i/D_{Si}) and **(b)** magma SiO_2 + Al_2O_3 (in wt%) after (Watkins et al., 2017). 'β' is related to

884   D_{44}/D_{40} by $(m_{44}/m_{40})^\beta$ [but must not to be confused with the same variable used for reduced partition function ratios

885   ($1000ln\beta$, as in Figs. 4-6) presented earlier in the text], where m_{44} and m_{40} are the atomic masses of [44]Ca and [40]Ca,

886   respectively. The efficacy of kinetic isotopic fractionation increases with increasing magma viscosity (SiO_2 +

887   Al_2O_3), with the largest effects in high SiO_2 magmas.

888   **6.2. Ca isotope diffusion in nature: whole-rock and inter-mineral fractionation models**

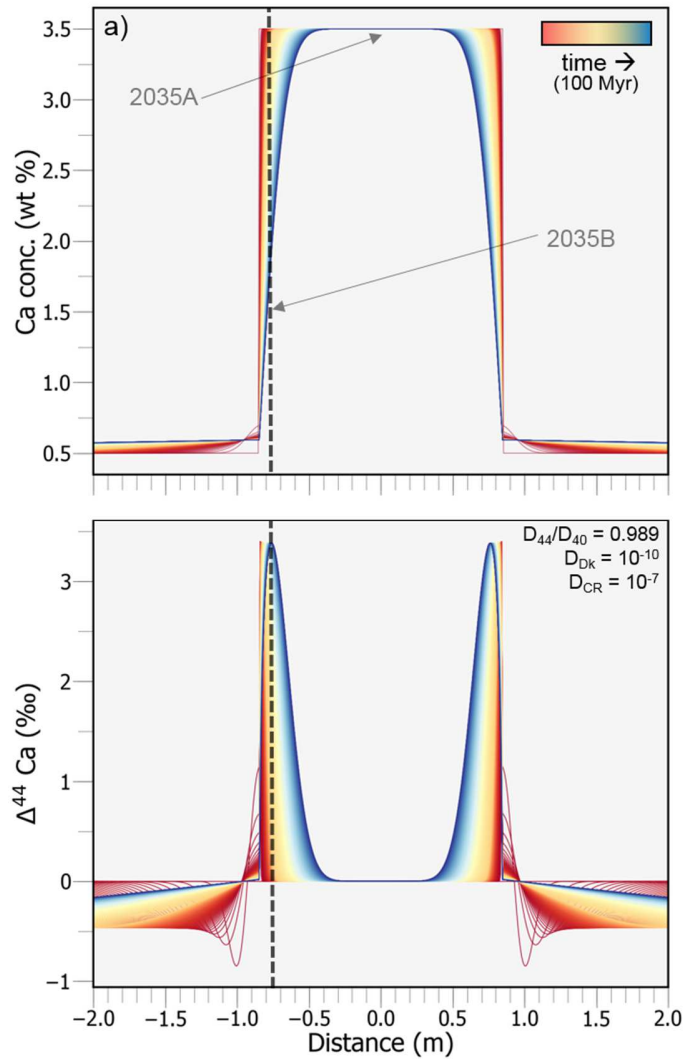889   Given that large (>1‰) inter-mineral and whole-rock δ^{44}Ca fractionations closely adhere to the

890   kinetic (diffusion-based) mass law in triple isotope space (see Fig. 12), it appears that Ca

891   diffusion is often responsible for isotopic disequilibrium observed in natural samples. However,

892   only a handful of studies have applied diffusion-based Ca isotope fractionation models to high-

893   temperature samples (Antonelli et al., 2019c, 2019b; Zhao et al., 2017).

894   The first study used disequilibrium δ^{44}Ca measurements (Δ^{44}Ca$_{opx-cpx}$ down to -0.5‰) in

895   metasomatized mantle xenoliths in order to constrain the product of calcium diffusivity and time

896   (Dt) for mantle metasomatism (Zhao et al., 2017). By assuming various Ca diffusivities and

897   D_{44}/D_{40} values for volume diffusion (from high-Ca fluids into solid pyroxene grains), and

898   combining them with estimates for grain-sizes, geometry, and original δ^{44}Ca, the authors were

899   able to constrain the duration of metasomatism by solving analytical diffusion equations (Zhao et

900   al., 2017). All of the minerals in the calculations were treated as spheres and the composition of

901   the percolating melt was assumed to not change over time, in accordance with the assumption of

902   high flow rates and high melt/peridotite ratios. The ^{44}Ca/^{40}Ca beta factors used in the successful

903   models varied between 0.05 and 0.10 [which are equivalent to those of an ultramafic and mafic

904   silicate liquid, respectively (see Fig. 14)], however, the models target diffusion *into* mineral

905   grains and not within the liquid phase, thus the isotopic diffusivity ratios assumed in the models

906   correspond to currently unconstrained fractionation factors for diffusion within solid minerals

907   ('volume diffusion'). Although future studies should focus on understanding Ca isotope

908   fractionations during volume diffusion in different minerals, the study (which also incorporates

909   Fe isotopes) is able to reproduce the measured isotopic fractionations with a large variety of

910   model parameter combinations [including variable clinopyroxene/orthopyroxene size ratios (0.33

911   to 0.66), temperatures (1000-1200°C), and olivine solid solution compositions (Fo90-Fo60)] and

912   uses these to constrain the duration of the associated metasomatic event to between 10^0 and 10^4

913   years (Zhao et al., 2017).

914   In a high-grade metamorphic example from the Napier Complex, disequilibrium $\Delta^{44}Ca$ between

915   adjacent whole-rocks (with known spatial constraints) were used in conjunction with numerical

916   diffusion models. Numerical methods, as opposed to analytical methods, are generally necessary

917   to model diffusion in heterogeneous media (where Ca diffusivity and D_{44}/D_{40} may vary between

918   layers). In order to constrain effective Ca diffusivities and D_{44}/D_{40} during granulite-facies

919   metamorphism in the lower crust, the authors used independent estimates for the duration of

920   high-temperature metamorphism in the Napier Complex and found that measured Ca

921   concentrations and $\delta^{44}Ca$ values were best reproduced by effective Ca diffusivity values ranging

922   from 10^{-10} to 10^{-7} m^2/yr (Fig. 15), consistent with previous estimates for Ca diffusion in high-

923   temperature rocks via grain-boundary and volume diffusion (*e.g.* Dohmen and Milke, 2010;

924   Farver and Yund, 1995; Giletti, 1994; Keller et al., 2008; Vielzeuf et al., 2007). The authors also

925   found that isotopic diffusivity ratios (D_{44}/D_{40}) of ~0.99 were necessary in order to reproduce the

926   measured $\delta^{44}Ca$ of the various units.

927   Given the existing experimental constraints for D_{44}/D_{40} in various media, a value of ~0.99

928   suggests that grain-boundary diffusion likely occurred within silicate melts as opposed to within

929   aqueous fluids [where fractionation factors are expected to be much smaller (*e.g.* Watkins et al.,

930   2017)]. As there is an on-going debate regarding the dominant mechanism through which

931   granulite-facies rocks lose their incompatible elements (*e.g.* dehydration *vs.* partial-melting/melt-

932   loss), these results, along with those previously described for mantle xenoliths (Zhao et al.,

933   2017), serve to highlight the potential for pairing diffusion models with disequilibrium Ca

934   isotope variations in order to constrain both the nature and rates of processes important to both

935   igneous and metamorphic petrology.

936

Fig. 15. Results of numerical modeling for Ca isotope diffusion between a high-Ca ultramafic dike and low-Ca pelitic country rock, metamorphosed at granulite-facies conditions for 100 Myr from (Antonelli et al., 2019c). The top panel shows changing Ca concentrations and the bottom panel shows the corresponding Δ^{44}Ca values over time (where Δ^{44}Ca corresponds to δ^{44}Ca$_{initial}$-δ^{44}Ca$_{final}$). The two analyzed samples (also shown in Fig. 12) come from the center ('2035A') and ~8cm from the edge ('2035B' demarcated by the dashed lines) of a ~1.7m thick dike and have pronounced Ca concentration and δ^{44}Ca differences, with the edge (~1.5 wt% Ca) being +3.3‰ heavier than the center (~3.5 wt% Ca). The initial conditions assume uniform δ^{44}Ca (and Ca concentration) across the dike, which slowly increase as Ca diffuses into the country rock. In order to reproduce the measured δ^{44}Ca and Ca concentrations at the correct locations, Ca diffusivities must equal ~10^{-10} m^2/yr and ~10^{-7} m^2/yr in the dike and

country rock, respectively. The required isotopic diffusivity ratio (D_{44}/D_{40}) is ~0.99, similar to that in dacitic liquids (see Fig. 14b). Additional details and diffusion model results for more complicated scenarios and rock-types can be found in the supplementary information of Antonelli et al. (2019c).

Another emerging application for disequilibrium inter-mineral $\Delta^{44}Ca$ data is to constrain metamorphic mineral paragenesis. Preliminary results from the previously discussed granulite study (Antonelli et al., 2019c) suggest that $\Delta^{44}Ca_{grt-mineral}$ fractionations are related to the pressure-temperature-time (PTt) paths for metamorphism, where retrograde garnet formation (*e.g.* during isobaric cooling from ultrahigh-temperatures) leads to negative disequilibrium $\Delta^{44}Ca_{grt-mineral}$ values, and prograde garnet formation (clockwise PTt paths) appears to generate positive $\Delta^{44}Ca_{grt-mineral}$ values closer to predicted isotopic equilibrium (schematically depicted in Fig. 16). Combined with the observed kinetic slopes for negative garnet-plagioclase fractionations in triple isotope space (Fig. 12), this observation suggests that Ca sourced from plagioclase may be subjected to kinetic effects during diffusive transport towards growing garnet grains during isobaric cooling (Antonelli et al., 2019c). The large kinetic effects during retrograde garnet formation, that appear to be essentially absent during prograde and magmatic garnet formation, could be due in part to the removal of volatile elements prior to its formation. However, very few samples have been measured and further work is required in order to better understand the origins of disequilibrium Ca isotope signatures observed between various metamorphic minerals.
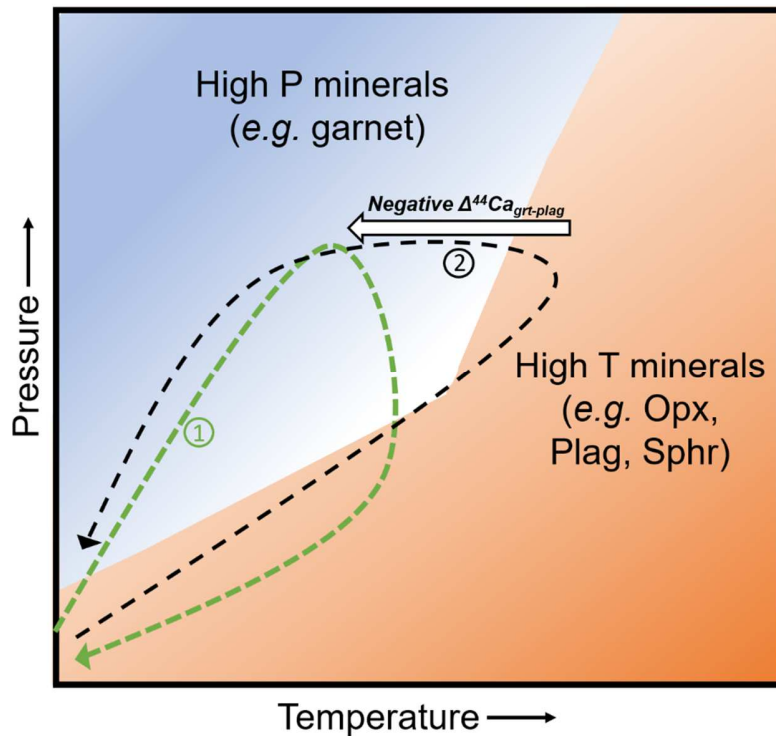
Fig. 16. Simplified conceptual phase diagram depicting the hypothesized effects of pressure-temperature-time (PTt) paths on the Ca isotopic differences observed between garnet and other minerals, as described in (Antonelli et al., 2019c). Path 1 (dashed green line) corresponds to a 'clockwise' heating path resulting in prograde garnet formation closer to isotopic equilibrium, while path 2 (dashed black line) corresponds to a 'counter-clockwise' path in which garnet is formed during isobaric cooling from very high-temperatures ('retrograde garnet growth') and acquires a negative disequilibrium $\Delta^{44}Ca_{grt-plag}$ signature (likely due to Ca diffusion, as suggested by $\Delta^{48}Ca'$ measurements).

By constraining Ca isotope compositions in individual grains (through the development of in-situ $\delta^{44}Ca$ analyses or more refined sampling techniques) and the average length-scales for Ca diffusion within a given system (*e.g.* through chemical image analyses), future studies should be able to yield important information on mineral paragenesis and Ca isotope disequilibrium related to metamorphic reactions.

Although our current state of knowledge on this topic is in its infancy, the various possibilities regarding isotopic fractionation during high-temperature metamorphic reactions can still be

979 evaluated. When a new phase is created at the expense of an existing phase ('net-transfer

980 reaction'), for example, the Ca isotopic composition of the precursor mineral(s) may be (i) at

981 equilibrium with the product phase (if the forward and backward exchange rates are much larger

982 than the net reaction rate), (ii) directly passed-on to the product phase (which would then require

983 subsequent isotopic re-equilibration with surrounding minerals), or (iii) subjected to kinetic

984 fractionation effects due to isotopic rate differences during bond breaking, diffusive transport

985 (within minerals or along grain-boundaries), and/or bond formation at the new mineral surface

986 (thereby inheriting an isotopic composition different from the precursor). During exchange

987 reactions, which are often used for geothermometry, pre-existing phases exchange components

988 in order to reach chemical equilibrium (*e.g.* Fe-Mg exchange between ferromagnesian minerals

989 and Ca exchange between clinopyroxene and orthopyroxene). Given that the exchange of

990 components is diffusive in nature, kinetic Ca isotope effects could occur via both volume and

991 grain-boundary diffusion. Upon completion of the chemical exchange, the new mineral may have

992 to isotopically re-equilibrate with surrounding phases in the absence of a chemical potential

993 gradient ('isotopic self-diffusion'), which may be exceedingly slow. Future studies of spatially

994 constrained δ^{44}Ca variations across minerals and grain boundary interfaces should allow us to

995 evaluate the possible mechanisms for inter-mineral Ca isotope disequilibrium in metamorphic

996 samples.

6.3. Crystal growth rates from Ca isotope disequilibrium in volcanic systems

998 Crystal growth rates in magmatic systems are especially important for understanding the physical

999 processes leading up to volcanic eruptions. Current methods, such as crystal-size distribution

1000 (CSD) analyses or trace-element diffusion profile models [see Cooper (2019)], however, must

1001 generally assume crystal-growth rates *a priori* in order to arrive at timescale estimates for the

1002　　associated volcanic process. Given that crystal growth rates in magmatic systems vary by at least

1003　　five orders of magnitude in nature (Cooper, 2019), they constitute a major uncertainty in

1004　　estimating the durations of past volcanic eruption and magmatic recharge events. In order to

1005　　address this problem, Ca isotope disequilibria have recently been used to independently estimate

1006　　crystal-growth rates in volcanic and sub-volcanic samples (Antonelli et al., 2019b).

1007　　Ca isotope growth rate estimates are based on the model predictions of Watson and Müller

1008　　(2009), where diffusion through a chemically-distinct boundary-layer (BL, formed around

1009　　rapidly growing phenocrysts) can lead to kinetic isotope effects during crystal growth. If growth

1010　　rates are rapid relative to Ca diffusivity in the melt (R/D), this is predicted to generate

1011　　disequilibrium Δ^{44}Ca variations in the crystals. As depicted in Fig. 17, crystallization of minerals

1012　　where Ca is compatible (K > 1, *e.g.* plagioclase, clinopyroxene) is expected to lead to formation

1013　　of a Ca-depleted BL (through which ^{40}Ca diffuses faster than ^{44}Ca) and negative kinetic Δ^{44}Ca,

1014　　whereas the opposite is expected if Ca is strongly incompatible within the mineral (K < 1, *e.g.*

1015　　olivine, orthopyroxene) (Fig. 17).

1016　　The predicted kinetic fractionations during crystal growth depend on: (i) crystal growth-rates

1017　　relative to Ca diffusivity (*R/D*), (ii) isotopic differences in Ca diffusion coefficients (*D_{44}/D_{40}*)

1018　　(iii) mineral-melt Ca distribution coefficients, and (iv) boundary-layer (BL) thicknesses around

1019　　the growing crystals (Watson and Müller, 2009). Given the development of a steady-state BL

1020　　during crystal growth, the kinetic δ^{44}Ca fractionation between crystals and melt (Δ^{44}Ca) is given

1021　　by:

$$\Delta^{44}Ca = 10^3 \left(1 - \frac{D_{40}}{D_{44}}\right)^{\frac{R \times BL}{D_{40}}} (1 - K) \qquad \text{(Eq. 4)}$$

1023 where D_{40} and D_{44} are the diffusivities of ^{40}Ca and ^{44}Ca in the melt, respectively, R is the crystal

1024 growth rate, BL is the boundary layer thickness, and K is the Ca distribution coefficient in the

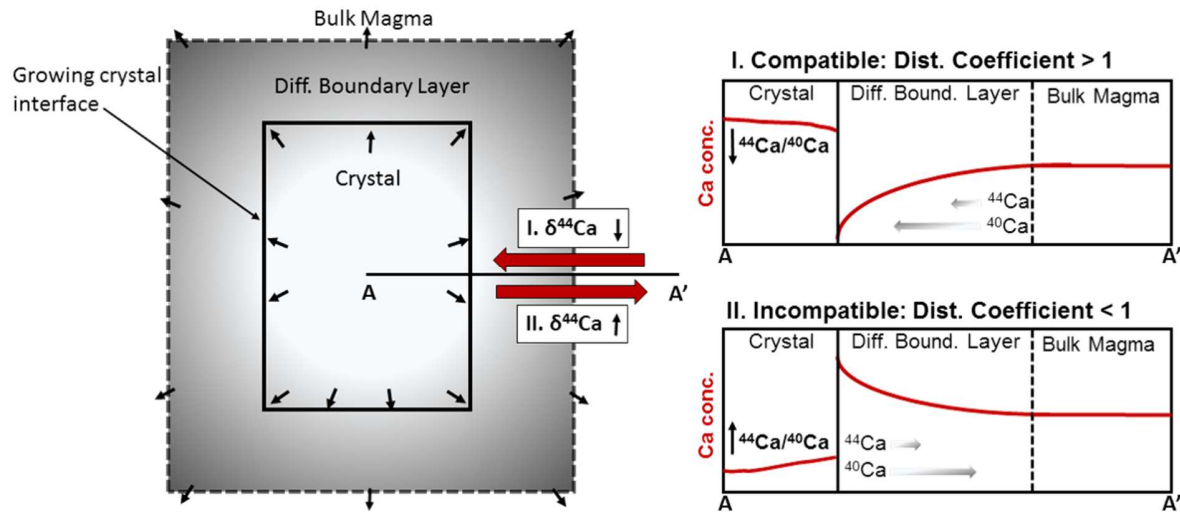1025 mineral *vs.* the melt (generally $K > 1$ in plagioclase).

1026

1027 **Fig. 17.** Schematic diagram showing the effects of Ca diffusion through a chemically-distinct boundary layer (BL)

1028 surrounding a growing crystal, based on the model of Watson and Müller (2009), figure from Antonelli et al.

1029 (2019b). When Ca is compatible within a mineral, depletion of Ca in the BL leads to an enrichment of ^{40}Ca at the

1030 mineral surface due to diffusion through the BL towards the crystal (top right panel); when Ca is incompatible,

1031 build-up of Ca in the BL leads to a relative enrichment of ^{44}Ca at the crystal surface as Ca diffuses away from the

1032 crystal (lower right panel). For further details see Antonelli et al. (2019b), Watkins et al. (2017), and Watson and

1033 Müller (2009).

1034 Analyzing plagioclase separates from rapid tonalite crystallization experiments (Antonelli et al.,

1035 2019b), it was found that the driest samples (1 wt% H_2O) have the largest fractionations

1036 ($\Delta^{44}Ca_{plag-matrix} = -2.2‰$) which gradually become smaller with increasing water contents

1037 ($\Delta^{44}Ca_{plag-matrix}$ of -1.0‰ and -0.3‰, for the 1.5 wt% and 2 wt% H_2O experiments, respectively).

1038 Although the limited data cannot rule out changes in isotopic diffusivity ratios (D_{44}/D_{40}) and BL

1039 thicknesses due to increasing H_2O (which have not yet been explored), the most simple

1040 explanation is that water leads to increases in Ca diffusivity and decreases in R/D (Antonelli et

1041 al., 2019b). Recent work on Li isotope diffusion suggests that water concentrations do not have a

1042 significant effect on isotopic diffusivity ratios in silicate liquids (Holycross et al., 2018), but this

1043 still remains to be confirmed for Ca isotopes. In natural phenocryst samples, clinopyroxene and

1044 other mafic minerals (amphibole, olivine) have slight positive $\Delta^{44}Ca_{mineral-matrix}$ (up to +0.3‰)

1045 and plagioclase phenocrysts have slightly negative $\Delta^{44}Ca_{mineral-matrix}$ (~-0.2‰). $\delta^{44}Ca$ variations of

1046 ~0.5‰ in high-purity plagioclase separates taken from orbicules and comb-layers, however,

1047 suggest especially fast growth rates. Assuming that equilibrium $\Delta^{44}Ca_{plag-melt} = 0$ [in agreement

1048 with Zhang et al. (2018)], and using conservative estimates for the other various parameters in

1049 Equation 4 [see supplementary text of Antonelli et al. (2019b)], the authors were then able to

1050 constrain minimum crystal growth rates in the volcanic systems (Fig. 18).

1051 Although the estimated growth rates for orbicules, comb-layers, and several natural phenocryst

1052 samples are faster than commonly assumed [typically assumed to be ~0.3 cm/yr in

1053 decompressing magmas (*e.g.* Brugger and Hammer, 2010; Cooper, 2019; Cooper and Kent,

1054 2014; Salisbury et al., 2008)], they agree with previous estimates for orbicule growth [~10 cm/yr,

1055 based on textural constraints from superheated experimental magmas (McCarthy and Müntener,

1056 2016; Shea and Hammer, 2013)], and rates as high as ~30 cm/yr have been described for

1057 crystallization of experimental plagioclase spherulites (Arzilli et al., 2015).

Fig. 18a-c. $\Delta^{44}Ca$ *vs.* Ca distribution coefficients for analyzed plagioclase separates from **(a,b)** experimental (n = 3) and natural phenocryst samples (n = 4) along with **(c)** separates from orbicule and comb-layer samples (Emerald Bay and Fisher Lake, n = 19) with dashed contours representing predictions for different crystal growth rates, after Antonelli et al. (2019b). In **(a,b)**, $\Delta^{44}Ca$ represents $\delta^{44}Ca$ differences between plagioclase and glass/matrix, and $D_{44}/D_{40} = 0.980$, in accordance with previous work shown in Fig. 14. Boundary-layer (BL) thicknesses are 100 μm, suggested as maximum values in dynamic systems (Lu et al., 1995). In **(c)**, $D_{44}/D_{40} = 0.990$ and $\Delta^{44}Ca$ represents kinetic effects based on differences for plagioclase $\delta^{44}Ca$ (Fisher Lake) or non-mineralogical $\delta^{44}Ca$ differences

1066   between orbicule layers (Emerald Bay). BL sizes are 200 µm to account for larger crystal sizes in the orbs and

1067   comb-layers. Rate estimates are directly proportional to BL thicknesses, such that ½ a given BL thickness leads to

1068   double the required growth rate. Average values and 2SE for Fisher Lake samples (AM26, AM131) and kinetic

1069   layers in OG sample (Emerald Bay) are represented by colored squares (n = 3) with bold error bars in panel **(c)**.

1070   In conjunction with crystal-size distribution (CSD) analyses and measurements of maximum

1071   crystal sizes, the authors were able to estimate the durations of crystal growth in various volcanic

1072   systems. For the mafic and silicic systems studied, the results yielded similar timescales (ranging

1073   from <1 day to ~2 months), suggesting that the previously observed relationship between

1074   magmatic timescales and melt compositions [where timescales appear to generally increase from

1075   mafic to silicic systems (*e.g.* Cooper, 2019)] may be due to *a priori* assumptions regarding

1076   crystal growth rates.

1077   Although the initial results are promising, much work remains in order to improve $\Delta^{44}Ca$ as a

1078   proxy for crystal-growth rates in volcanic systems. This includes, for example, careful separation

1079   of different phenocryst populations for a given mineral within a sample, where populations of

1080   smaller crystals (*e.g.* plagioclase microlites) are likely to have crystallized the fastest and to

1081   contain the largest disequilibrium $\Delta^{44}Ca_{plag-melt}$ signatures. The samples shown in Fig. 18

1082   represent mixtures of different plagioclase crystal populations (up to 3 per sample in the

1083   phenocrystic rocks), so the $\Delta^{44}Ca$ measurements represent minimum values for the rapidly-

1084   grown populations within each sample (Antonelli et al., 2019b). Furthermore, most of the

1085   parameters in Equation 1 are poorly constrained and could benefit from additional crystallization

1086   experiments and detailed observations of natural samples. This would then allow future studies

1087   to incorporate, for example, (i) the effects of multi-component diffusion into D_{44}/D_{40} estimates,

1088   which could also consider chemical variations in BL compositions, (ii) variations in BL sizes in

1089   natural and experimental systems, and (iii) compositional and pressure/temperature dependence

1090 of Ca diffusivity in magmas. Nevertheless, preliminary results suggest that Ca isotopes provide

1091 an exciting new opportunity for understanding fundamental aspects of crystallization and

1092 magmatic recharge across volcanic systems observed on Earth today and in the geologic past.

6.4. High fluid/rock and hydrothermal systems

1094 The Ca isotope composition of hydrothermal fluids and minerals has not been as extensively

1095 studied as low temperature weathering and carbonate mineral formation processes. Despite the

1096 relatively few studies of Ca isotopes in hydrothermal systems, high temperature fluid-mineral

1097 reactions are important for the global geochemical cycle because ocean hydrothermal systems

1098 are the second largest Ca flux to the oceans (Staudigel, 2003). Additionally, fossil hydrothermal

1099 systems record information about water rock reactions in a diverse set of geologically important

1100 environments such as porphyry deposits, continental hydrothermal systems, and ophiolites.

1101 Shallow heat from mid-ocean ridge magmatism drives fluid circulation with the influx of

1102 seawater into the ocean crust and the emergence of high temperature (~400°C) fluids at the ridge

1103 axis that are chemically distinct from seawater. Chemical reactions in the hydrothermal flow path

1104 remove Mg and SO_4 and exchange seawater Ca (and Sr) for Ca derived from igneous minerals

1105 (*e.g.* Staudigel, 2003; von Damm, 2000). Because the Ca isotope cycle in the ocean is possibly a

1106 robust record of past climate, the effect of hydrothermal reactions on the Ca isotope composition

1107 of seawater is an important research question.

1108 The first measurements of mid-ocean ridge hydrothermal fluids were reported by Schmitt et al.

1109 (2003), while subsequent data were reported by Amini et al. (2008), and most recently by

1110 Scheuermann et al. (2018). Sampled hydrothermal fluids are often mixed with seawater, and thus

1111 require some correction to calculate their hydrothermal endmember compositions. Figure 19

1112 shows a compilation of hydrothermal fluid δ^{44}Ca values as a function of percent seawater, which

assumes that hydrothermal fluids have [Mg] = 0 and seawater has [Mg] = 53 mM (*e.g.* Lowenstein et al., 2013; Turchyn and DePaolo, 2019). While the data exhibit scatter and are heavily weighted at the near-zero and near-100% seawater endmembers, they suggest that high temperature hydrothermal fluids have Ca isotope compositions similar to MORB ($\delta^{44}Ca_{BSE} \approx 0$, which is approximately -1‰ relative to modern seawater).

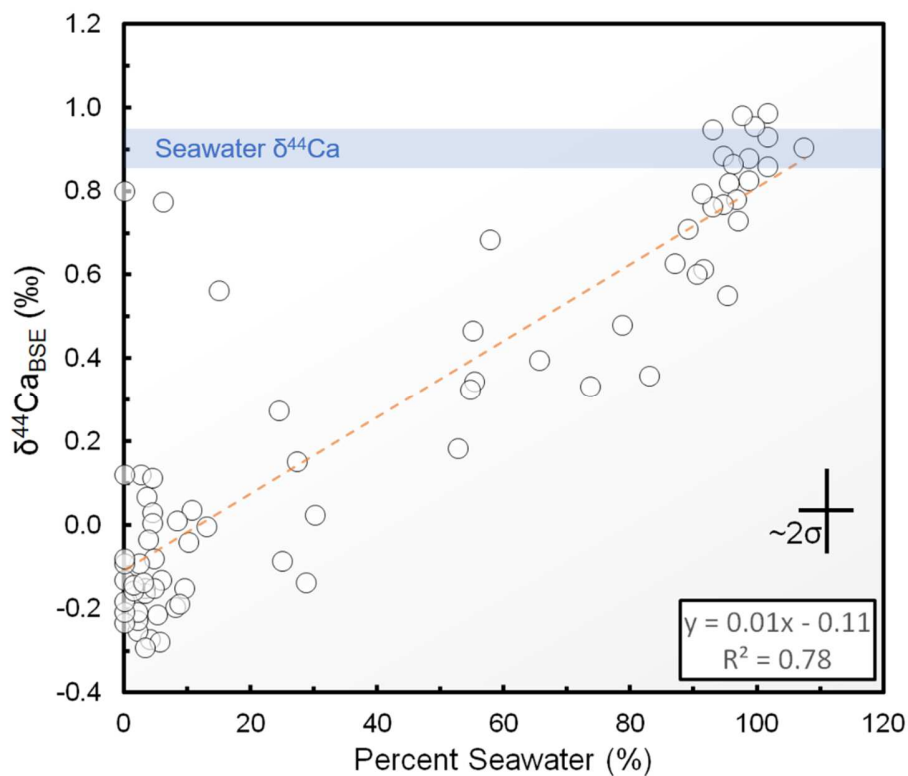**Fig 19.** $\delta^{44}Ca$ of hydrothermal fluids as a function of seawater percentage. Seawater percentage is based on Mg concentrations assuming end-member hydrothermal fluids and seawater have [Mg] of 0 and 53.4 mM, respectively. Data are from (Amini et al., 2008; Scheuermann et al., 2018; Schmitt et al., 2003).

The hydrothermal fluid data are consistent with near complete Ca isotopic exchange between infiltrating seawater and basaltic minerals and require little or no net Ca isotopic fractionation in high temperature hydrothermal systems. Radiogenic Ca isotope differences reported between seawater and modern hydrothermal vents (Antonelli et al., 2019a, 2018) also suggest that the Ca

1126 within hydrothermal fluids is sourced almost entirely from oceanic crust. The Ca isotope system

1127 is thus dissimilar to $^{87}Sr/^{86}Sr$, which is incompletely exchanged in modern and some ancient

1128 hydrothermal systems (Amini et al., 2008; Antonelli et al., 2017; Turchyn et al., 2013). The

1129 complete exchange of Ca isotopes and incomplete exchange of Sr isotopes is likely due to the

1130 relative distribution between the fluid and rock phases, where $[Ca]_{basalt}/[Ca]_{seawater}$ is an order of

1131 magnitude higher than $[Sr]_{basalt}/[Sr]_{seawater}$ (Brown et al., 2020). Brown et al. (2020) presented

1132 simplified reactive transport models for Ca and Sr in mid-ocean ridge hydrothermal systems that

1133 suggest $^{87}Sr/^{86}Sr$ in hydrothermal fluids can vary as a function of paleoseawater composition [as

1134 predicted in Antonelli et al. (2017)], but $\delta^{44}Ca$ values in hydrothermal fluids are likely to be the

1135 same as MORB (or at the most ~0.1‰ displaced toward seawater) in the geologic past. In

1136 contrast, it is possible that serpentinite-hosted hydrothermal systems are shifted from local rock

1137 compositions (*e.g.* Amini et al., 2008; Scheuermann et al., 2018) and could lead to distinct

1138 hydrothermal $\delta^{44}Ca$ signatures.

1139 As opposed to oceanic hydrothermal systems, studies of continental hydrothermal systems show

1140 relatively large variations in fluid $\delta^{44}Ca$ up to 1.5‰ (Brown et al., 2013; Wiegand et al., 2015).

1141 The primary observation is that $\delta^{44}Ca$ of the hydrothermal fluids increases as the fluid Ca

1142 concentration decreases, broadly consistent with isotope fractionation during secondary mineral

1143 precipitation (Brown et al., 2013; Wiegand et al., 2015). In the case of Long Valley caldera, the

1144 $\delta^{44}Ca$ shifts are primarily attributed to secondary carbonate mineral precipitation, which is a

1145 larger magnitude effect than Ca supply by primary mineral dissolution. The magnitude of $\delta^{44}Ca$

1146 fractionation (α) for the Long Valley system was inferred using an isotope distillation model,

1147 which yielded α=0.99965, similar to observations of calcite-fluid pairs: 0.99945-0.99970 (Brown

1148 et al., 2013). While the inferred fractionations are smaller than low temperature processes such

1149   as marine carbonate precipitation, the fractionations are greater than would be predicted by

1150   temperature-dependent equilibrium models extended from low temperature minerals (Brown et

1151   al., 2013).

1152   Hydrothermal minerals offer an additional opportunity to assess the mechanisms and magnitude

1153   of Ca isotope fractionation in high temperature fluids. Figure 20 shows a compilation of $\Delta^{44}Ca$

1154   for synthetic and natural hydrothermal minerals as a function of fluid temperature. In some cases

1155   the fluid and minerals were directly measured (Brown et al., 2013; Syverson et al., 2018), for

1156   others the fluid composition and temperature have been calculated based on $^{87}Sr/^{86}Sr$ and

1157   isenthalpic mixing between seawater and vent fluids (Amini et al., 2008; Griffith et al., 2008b).

1158   For epidotes, a reactive transport model was used to estimate the fluid composition (Brown et al.,
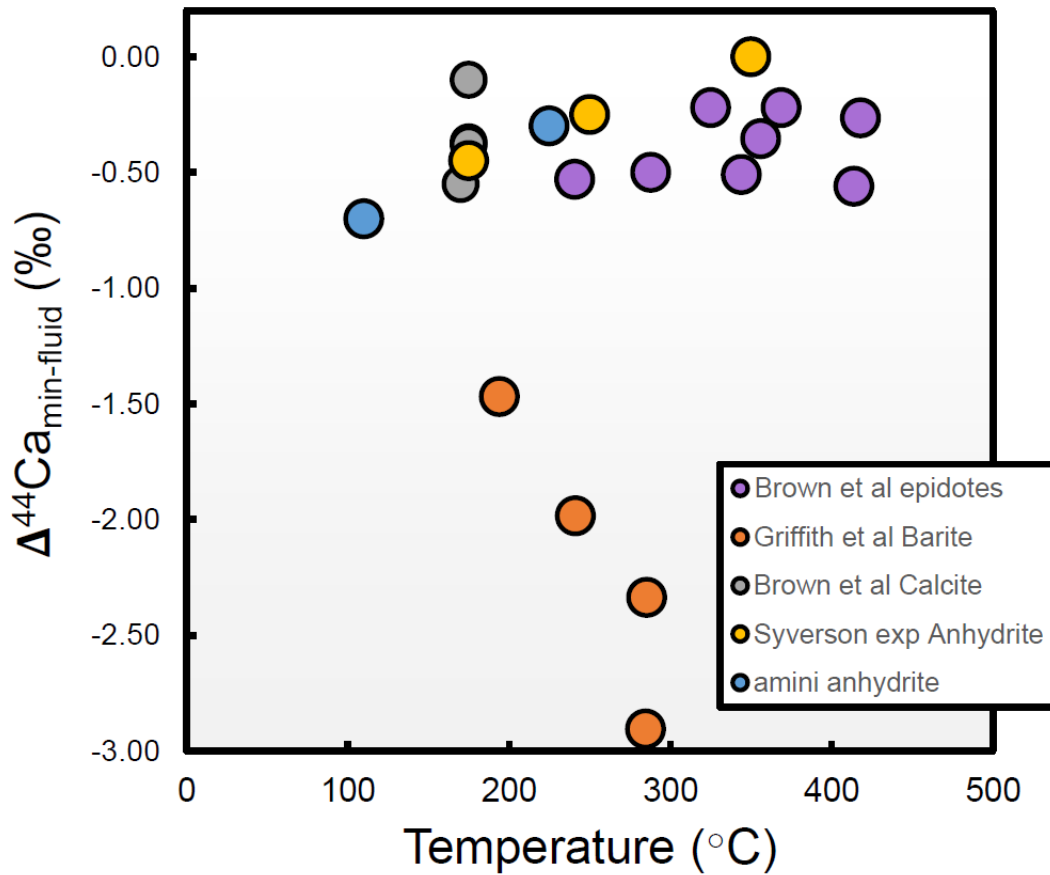
1159   2020).

1160

Fig. 20. Compilation of Ca isotope fractionation between hydrothermal fluids and hydrothermal minerals with

increasing temperatures (n = 20). The different colors correspond to epidote (purple), barite (orange), calcite (grey),

experimental anhydrite (yellow), and natural anhydrite (light blue). Data are from (Amini et al., 2008; Brown et al.,

2020, 2013; Griffith et al., 2008b; Syverson et al., 2018).

1165   The first and most significant observation is that $\Delta^{44}Ca_{mineral-fluid} \leq 0$, with only one sample at

1166   unity. Additionally, there is no obvious trend in $\Delta^{44}Ca$ with temperature for the dataset as a

1167   whole, however, the anhydrites show decreasing fractionation with increasing temperature, while

1168   the $\Delta^{44}Ca$ of barites are positively correlated with temperature (Fig. 20).

1169   Amini et al. (2008) used the temperature dependence of $\Delta^{44}Ca$ for anhydrite to predict an average

1170   isotopic fractionation of $\Delta^{44}Ca_{fluid-anhydrite}$ of -0.54‰, but the temperature relationship is less

1171 robust if the experimental data of Syverson *et al.* (2018) are included (Fig. 20). In contrast,

1172 Brown et al. (2020, 2013) found no Δ^{44}Ca temperature dependence for hydrothermal calcite or

1173 epidote. Thus, the extent to which there is a temperature dependence to Δ^{44}Ca for hydrothermal

1174 minerals remains an open question. One possible reconciliation of the data is that the relationship

1175 between temperature and Δ^{44}Ca is actually related to rapid changes in mineral saturation with

1176 fluid temperature changes. In this case, changes in temperature might correlate with mineral

1177 saturation (greater oversaturation is generally linked to faster precipitation rates) and by

1178 extension Δ^{44}Ca. This suggests that Δ^{44}Ca in hydrothermal minerals is primarily a kinetic

1179 effect—similar to the previously discussed examples for igneous and metamorphic mineral

1180 assemblages.

1181 Significant Δ^{44}Ca between hydrothermal fluids and secondary minerals offer an opportunity to

1182 quantify subsurface processes in mid-ocean ridges, economic geothermal fields, and possibly in

1183 mineralizing fluids, however, additional research is required to better understand the underlying

1184 fractionation mechanisms and their implications for fluid-rock systems. Future work should

1185 include experiments at varying water-rock ratios, fluid chemistry, and temperatures, in order to

1186 enable more quantitative interpretations of modern and fossil hydrothermal systems.

1187 **7. Employing radiogenic and stable Ca isotopes as high-temperature source-tracers**

1188 The application of Ca isotopes as a petrogenetic tracer is different but complementary to other

1189 more commonly used trace element isotope systems (*e.g.* Sr, Pb, Hf, and Pb). The K-Ca

1190 radioactive system (half-life of ~1.25 Ga), however, behaves differently because this parent-

1191 daughter system involves elements that make up stoichiometric constituents of major minerals,

1192 and therefore the concentrations of K and Ca, and the K/Ca ratio in rocks, are directly related to

1193 mineralogy (*e.g.* Marshall and DePaolo, 1989). Radiogenic Ca isotope excesses are commonly

1194   reported using epsilon notation, after correcting for natural and instrumental mass-fractionation

1195   (using an exponential law and $^{42}Ca/^{44}Ca = 0.31221$):

$$\varepsilon_{Ca} = 10{,}000 \left[\frac{\left(^{40}Ca/_{44}Ca\right)_{sample}}{\left(^{40}Ca/_{44}Ca\right)_{BSE}} - 1 \right] \qquad \text{(Eq.}$$

1196

1197   5)

1198   Where $(^{40}Ca/^{44}Ca)_{BSE}$ is generally assumed to be 47.162, though recent work suggests that a

1199   value of 47.156 (about 1 epsilon unit lower), may be more accurate (Antonelli et al., 2019a,

1200   2018; Mills et al., 2018). The comparatively large mass differences among Ca isotopes cause

1201   physiochemical processes to produce relatively large mass-dependent variations in nature, even

1202   at relatively high temperature. Although such studies are not routine, as methods become more

1203   efficient and measurements become more reproducible, both radiogenic and stable Ca isotope

1204   signatures will play important roles in tracking the petrological evolution of planetary to outcrop-

1205   scale processes in igneous and metamorphic rocks.

1206   **7.1. Carbonate recycling in the mantle**

1207   Over 50 years of sample measurements have shown that the mantle remains chemically and

1208   isotopically heterogeneous despite the fact that mantle convection has been active for most of

1209   Earth's history. Oceanic basalt studies employing radioactive isotope systems (*e.g.*, Sr, Nd, and

1210   Pb) have been used to identify compositionally distinct mantle reservoirs that reflect recent

1211   mixtures of different source components as well as the time integrated compositional history of

1212   ancient mantle reservoirs (*e.g.* Hawkesworth and Van Calsteren, 1984). Likewise, there are a

1213   number of geochemical and isotopic systems that have been used to suggest that recycled marine

1214   sediments are important in the petrogenesis of ocean island basalts (*e.g.* Blichert-Toft, 1999;

1215   Castillo et al., 2018; Dasgupta et al., 2004; Frey et al., 1994; Huang et al., 2009; Huang and Frey,

1216   2005; Lassiter and Hauri, 1998; Plank and Langmuir, 1998). The interconnection between

1217   recycled materials at subduction zones and more ancient mantle reservoirs remains elusive,

1218   however, and debates continue as to whether recycling at subduction zones is related to the

1219   isotopic heterogeneity in oceanic basalts.

1220   Ca isotopes potentially provide a powerful tool to test ideas about the various potential source(s)

1221   of mantle heterogeneity, in particular for recycling of Ca-rich marine sedimentary materials,

1222   because both radiogenic and stable Ca isotope variations yield complementary information.

1223   Significant stable mass-dependent Ca isotope variability is not generally expected to originate at

1224   mantle solidus temperatures under which oceanic basalts have been generated (>1200-1500°C,

1225   *e.g.* Putirka, 2005; Zhang et al., 2018). However, subduction and recycling of sediments,

1226   especially marine carbonates, could introduce distinctive Ca isotopic variations within the mantle

1227   because marine carbonates have high Ca concentrations with potentially light $\delta^{44}Ca$, up to ~2‰

1228   lower than BSE (De La Rocha, 2000; DePaolo, 2004; Fantle and DePaolo, 2005; Farkaš et al.,

1229   2007; Griffith et al., 2008a; Heuser et al., 2005; Kasemann et al., 2005; Watkins et al., 2017; Zhu

1230   and Macdougall, 1998).

1231   To date, resolvable radiogenic Ca signatures have not been observed in oceanic basalts (Huang et

1232   al., 2011; Marshall and DePaolo, 1989; Simon et al., 2009). This might not be surprising given

1233   the work of Caro et al. (2010) who despite finding well-defined excesses of ^{40}Ca in some river

1234   waters draining into the ocean, report that no discernable effects of ^{40}K decay (within their

1235   reported analytical precision of ~0.4 epsilon units, 2σ) were seen in a number of marine

1236   carbonate samples ranging in age from Archean to recent. This led the authors to conclude that

1237   hydrothermal Ca has dominated the oceanic budget over all of Earth history. This conclusion is

1238   at odds, however, with estimates of modern riverine *vs.* hydrothermal Ca fluxes (*e.g.* DePaolo,

1239   2004) and with ε_{Ca} differences observed between modern seawater/carbonates and hydrothermal

1240   fluids/mafic igneous rocks (Antonelli et al., 2019a, 2018).

1241   Stable mass-dependent Ca isotope signatures that correlate with other geochemical parameters

1242   (Sr/Nb and $^{87}Sr/^{86}Sr$, shown in Fig. 21) have been interpreted to represent recycling of ancient Ca

1243   bearing surface materials in Hawaiian lavas (*e.g.* Huang et al., 2011). Although the interpretation

1244   of the trends presented by Huang et al. (2011) is currently under debate due to the low $\delta^{44}Ca$ and

1245 $^{87}Sr/^{86}Sr$ values required for the carbonates, it has been reported that that the global ocean (and

1246   thus marine carbonates) may have gradually evolved through time towards higher $\delta^{44}Ca$ values

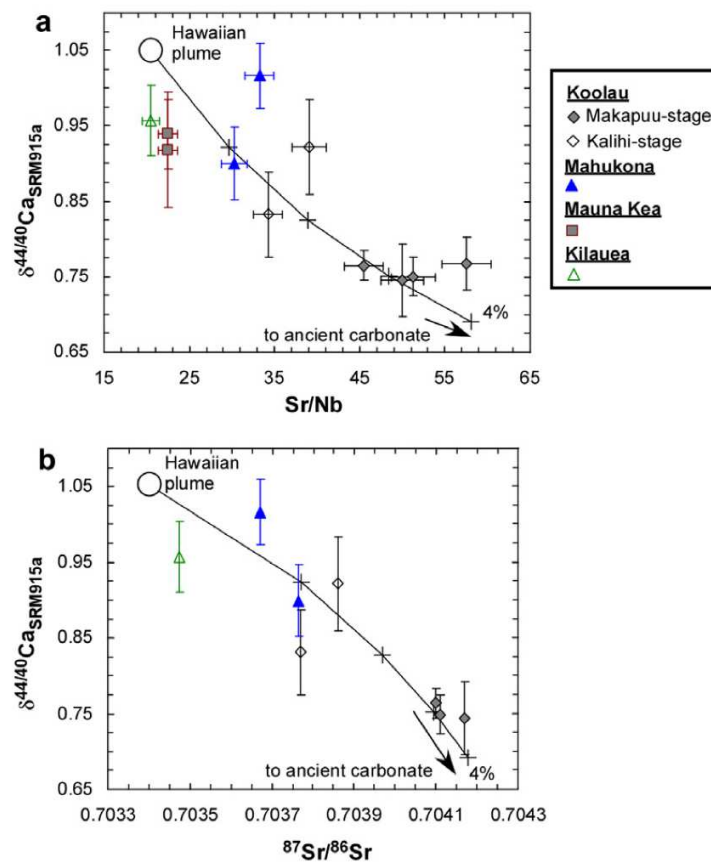1247   (*e.g.* Farkaš et al., 2007).

1248

1249 **Fig. 21a,b.** Stable Ca isotope variations versus traditional proxies for carbonate incorporation in Hawaiian shield

1250 lavas after Huang et al. (2011). **(a)** $\delta^{44}Ca$ *vs*. Sr/Nb, **(b)** $\delta^{44}Ca$ *vs*. $^{87}Sr/^{86}Sr$. In this figure, Ca isotope ratios are

1251 reported relative to SRM915a (-0.95‰, relative to BSE), and the carbonate end-member component is assumed to

1252 have 800 ppm [Sr], 0 ppm [Nb], $^{87}Sr/^{86}Sr$ = 0.7034, [CaO] = 56 wt%, and $\delta^{44}Ca_{SRM915a}$ = 0.2‰ (-0.75‰ relative to

1253 BSE).

1254 However, the importance of both of these studies has been challenged more recently, in part,

1255 because marine carbonates deposited over the last ~2.5 Ga have average $\delta^{44}Ca$ that exhibit little

1256 change through time, with values similar to BSE (Blättler and Higgins, 2017). Likewise, it has

1257 been recently shown that carbonate metasomatism in the mantle has no discernable $\delta^{44}Ca$ effects

1258 (Ionov et al., 2019). More work like that of Huang et al. (2011), therefore, is needed to validate

1259 the influence of sediment recycling on the isotopic source compositions of igneous rocks. One

1260 possible reconciliation of these models and data could be that the marine carbonate records no

1261 longer accurately record their ancient (isotopically light) signatures because they have been reset

1262 more recently by exchange with bulk silicate mantle Ca reservoirs.

1263 **7.2. Crustal Contamination in Magmatic Systems**

1264 The Ca isotope ratio determinations of Russell et al. (1978) provide the basis for all current

1265 measurements. Established on sample measurements where radiogenic ^{40}Ca excesses are

1266 negligible, these values are used to represent the normal terrestrial composition at ca. 0.01%

1267 resolution. For radiogenic enrichment studies, Ca isotope variations are commonly reported as

1268 ε_{Ca} (Equation 5). Radioactive decay of ^{40}K within the continental crust can produce a Ca isotopic

1269 signature where ^{40}Ca excesses $\geq$ 0.5 epsilon units are distinguishable from mantle-like Ca isotope

1270 compositions, as shown in Mills et al. (2018). First employed in modern literature for igneous

1271 rocks by Marshall and DePaolo (1989, 1982), the K-Ca radiogenic isotope system has not been

1272   applied to many petrogenetic studies primarily because of the difficulty in decoupling the

1273   radiogenic enrichments of ^{40}Ca from stable ^{40}Ca that makes up ~97% of terrestrial calcium.

1274   Oceanic basalts largely have compositions and isotopic signatures that indicate derivation from

1275   partial melting of mantle sources. At levels that were near the analytical capabilities available at

1276   the time, however, Marshall and DePaolo (1989) showed the first evidence for crustal (^{40}Ca-

1277   enriched) calcium in some oceanic island arc magmas. The source components for more evolved

1278   magmas erupted through, or emplaced within, continental crust also remain debated. The

1279   petrogenic origin(s) of evolved magmas in the continental crust can be complicated because the

1280   relative importance of various petrogenetic processes, including magma mixing, fractional

1281   crystallization, and assimilation-fractional crystallization (*i.e.,* AFC), controlling magma

1282   differentiation can vary (DePaolo, 1981).

1283   As with studies of crustal recycling discussed above, trace element radiogenic isotope systems

1284   have long been used to assess the petrogenesis of felsic magmas. Despite all that has been

1285   learned from trace element radiogenic studies, unresolved geologic problems remain. In fact, one

1286   of the most important and long-standing challenges is the ability to distinguish the contributions

1287   of mantle-derived sources in felsic magmas that are generated from preexisting continental crust

1288   [see Mills et al. (2018) and reference therein]. Although old continental crust and asthenospheric

1289   mantle sources can be readily distinguished with ε_{Nd} values, these authors showed that by

1290   combining radiogenic Nd and Ca isotope ratios, significant progress can be made. This is

1291   because whereas non-radiogenic Nd can be indicative of either old continental crust or

1292   lithospheric mantle, Ca isotopes can potentially distinguish between crustal (elevated ε_{Ca}) and

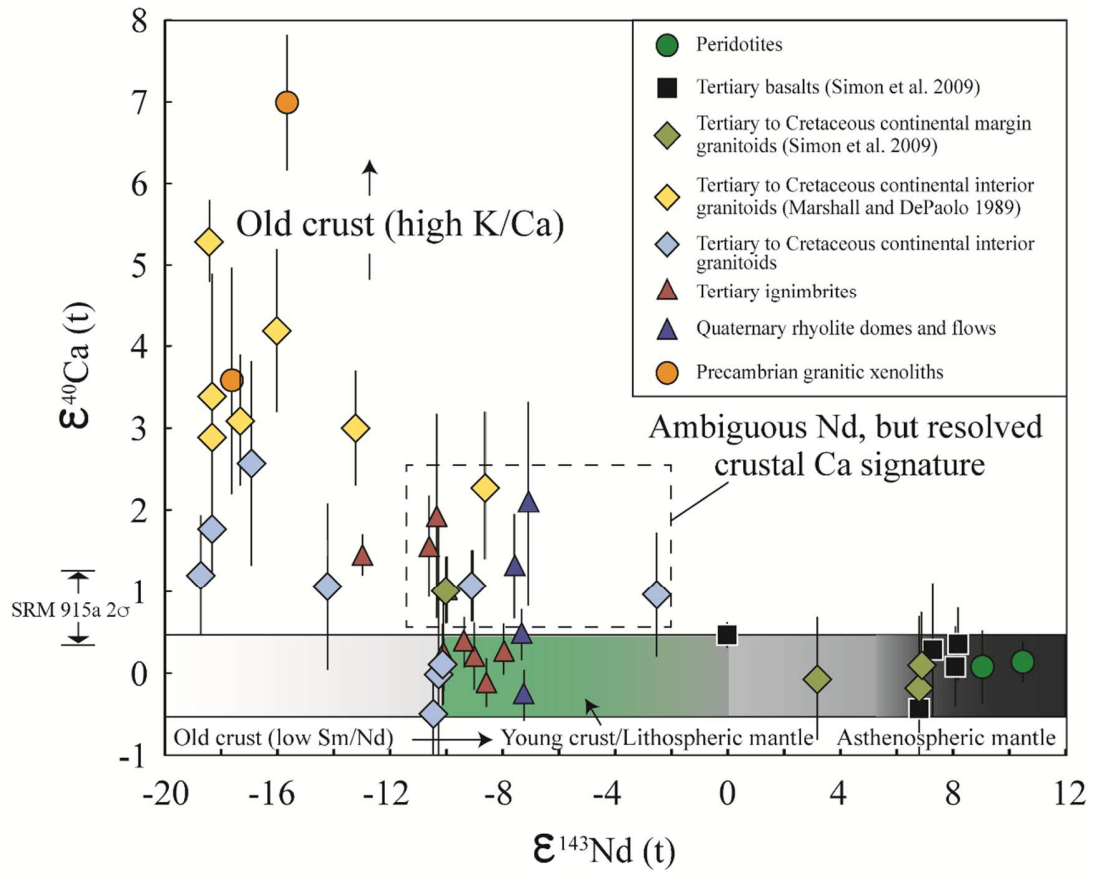1293   lithospheric mantle (near zero ε_{Ca}) sources (Fig. 22).

Fig. 22. Plot of age-corrected ε^{143}Nd *vs.* ε^{40}Ca showing the potential use of radiogenic Ca for discriminating between different mantle sources. The Data are from Mills et al. (2018) unless otherwise indicated in the legend. Epsilon values for Ca were calculated using the average ^{40}Ca/^{44}Ca value measured for peridotite and data from Simon et al. (2009) for oceanic basalts, which was used to define bulk silicate Earth. The SRM 915a value (shown on left axis) is ~1 ε-unit higher than bulk silicate Earth. Epsilon values for Nd were calculated using ^{143}Nd/^{144}Nd (CHUR, 0 Ma) = 0.512638 and ^{147}Sm/^{144}Nd (CHUR, 0 Ma) = 0.1967.

7.3. Radiogenic Ca and K-loss in metamorphic systems

The loss of incompatible trace elements (*e.g.* U, Rb) during melting/dehydration of granulite-facies rocks is well documented (*e.g.* Rudnick et al., 1985; Rudnick and Gao, 2014). The resultant transfer of heat-producing elements from the lower-crust to the middle- and upper-crust is an essential aspect of many models for the creation of stable continents (through the coupling

1306   of continental crust and lithospheric mantle, 'cratonization'). Given that ^{40}K was the largest

1307   source of radioactive heat on the early Earth, loss of potassium from the lower crust is especially

1308   important for cratonization, however, other than by comparison with similar systems (*e.g.* Rb/Sr,

1309   Rudnick et al., 1985) and direct measurements [in rare cases when the unmetamorphosed

1310   protoliths are still available (*e.g.* Ewing et al., 2014; Stepanov et al., 2014)], there have been no

1311   direct proxies for K-loss from these systems.

1312   To address this issue, a recent study used radiogenic ^{40}Ca measurements (ε_{Ca}) in order to directly

1313   constrain K-loss during high-temperature granulite-facies metamorphism of the lower crust

1314   (Antonelli et al., 2019a). Analyzing ^{40}Ca/^{44}Ca in garnet separates from granulite-facies rocks, the

1315   authors found large enrichments in ε_{Ca} (up to +42) correlating inversely with garnet grossular

1316   percentage and positively with whole-rock peraluminosity index ('A/CNK', defined as molar

1317 Al_2O_3/CaO + Na_2O + K_2O, Fig. 23a,b). The large radiogenic ^{40}Ca enrichments must have

1318   occurred through decay of ^{40}K in protolith rocks, prior to garnet formation, as garnet is very

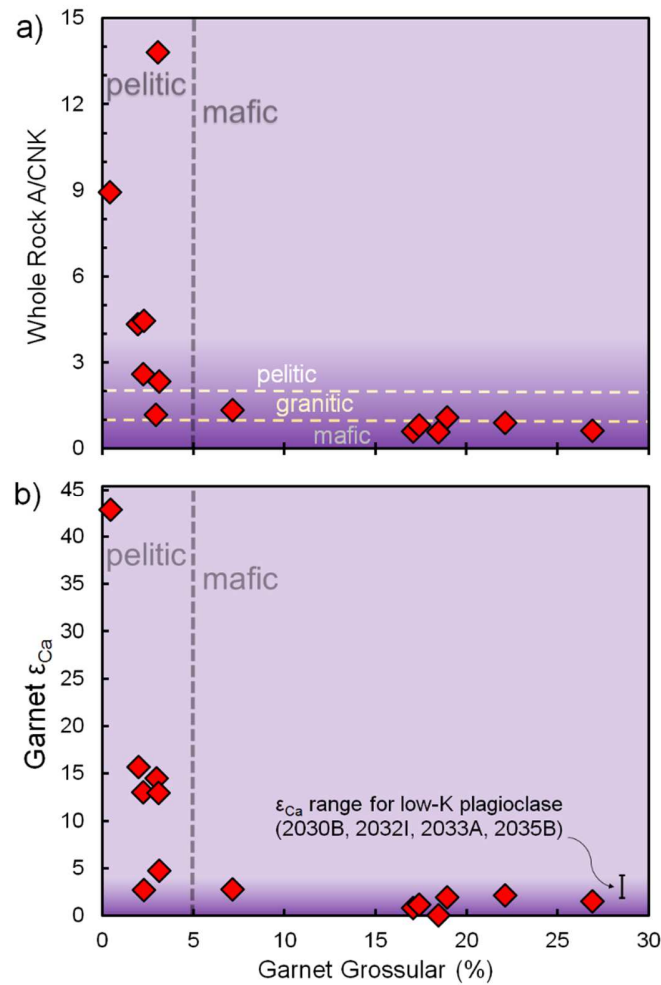1319   effective at excluding K during crystallization.

Fig. 23a,b. (a) Whole rock A/CNK, defined as molar $Al_2O_3/(CaO+Na_2O+K_2O)$ and **(b)** ε_{Ca} data for garnet separates from granulite-facies metamorphic rocks versus garnet grossular (%); after Antonelli et al. (2019a). Approximate compositional fields for various protoliths (based on A/CNK and garnet grossular) are demarcated with dashed lines. Garnet efficiently excludes K from its crystal structure, thus the measured ε_{Ca} values are the initial values at time of metamorphism. A bulk-silicate Earth $^{40}Ca/^{44}Ca$ value of 47.156 was used to calculate ε_{Ca}.

Using available protolith and metamorphic age estimates for the various localities, the authors placed constraints on the protolith K/Ca values necessary to generate initial ε_{Ca} recorded by garnet, assuming the oldest protolith ages from each locality in order to arrive at minimum protolith K/Ca estimates (as shown in Fig. 24). This figure also serves to demonstrate the relationship between estimated protolith K/Ca and uncertainties in associated protolith age

1331   estimates, where an uncertainty of ±0.3 Ga gives K/Ca estimates consistent within a factor of ~2,

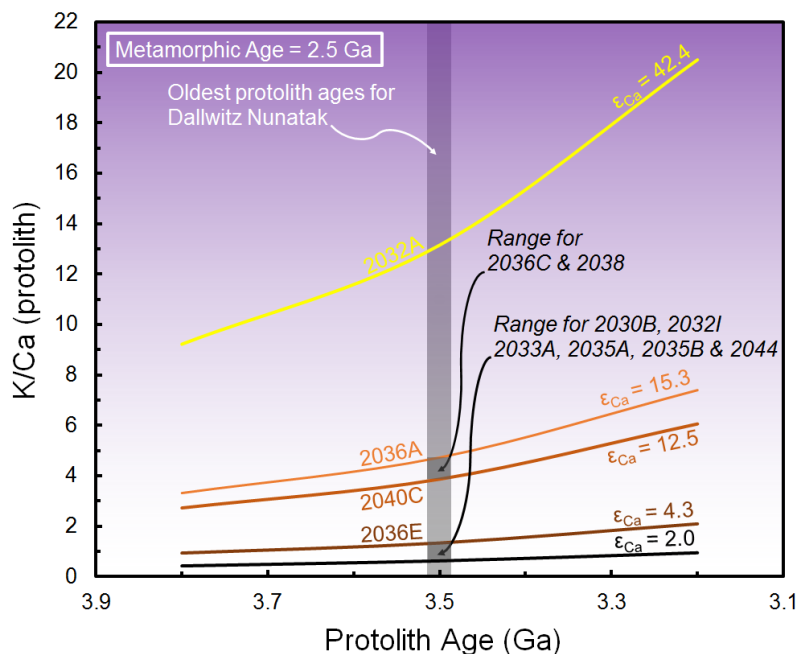1332   even for ancient samples where radiogenic ingrowth of ^{40}Ca had the biggest effects.

1333

Fig. 24. Effect of protolith age uncertainty on estimated protolith K/Ca, after Antonelli et al. (2019a). The different lines represent garnet ε_{Ca} measurements from granulite-facies rocks from the Napier Complex, where the metamorphic age is ~2.5 Ga. Due to the very low compatibility of K in garnet, garnet is assumed to represent whole-rock ε_{Ca} at the time of metamorphism. Although protolith ages are not often constrained with great precision, this figure demonstrates the relatively minor effect that this has on estimated protolith K/Ca.

Comparing protolith estimates to K/Ca measured in the rocks today, minimum values for K loss (relative to Ca) during lower crustal metamorphism were constrained to ~67% to > 95% (Fig. 25a), confirming that K is effectively lost from the lower-crust during metamorphism. A non-modal batch melting model [*see SI text of Antonelli et al. (2019a) for details*] suggests that most samples represent 20-30% granitic melt-loss (Fig. 25b). These estimates are in good agreement with other estimates for melt-loss during granulite-facies metamorphism, (*e.g.* Yakymchuk and Brown, 2014), but further constraints on K and Ca partitioning during partial melting, along with

1346 sample-specific protolith age estimates, would be greatly useful to further constrain K and melt
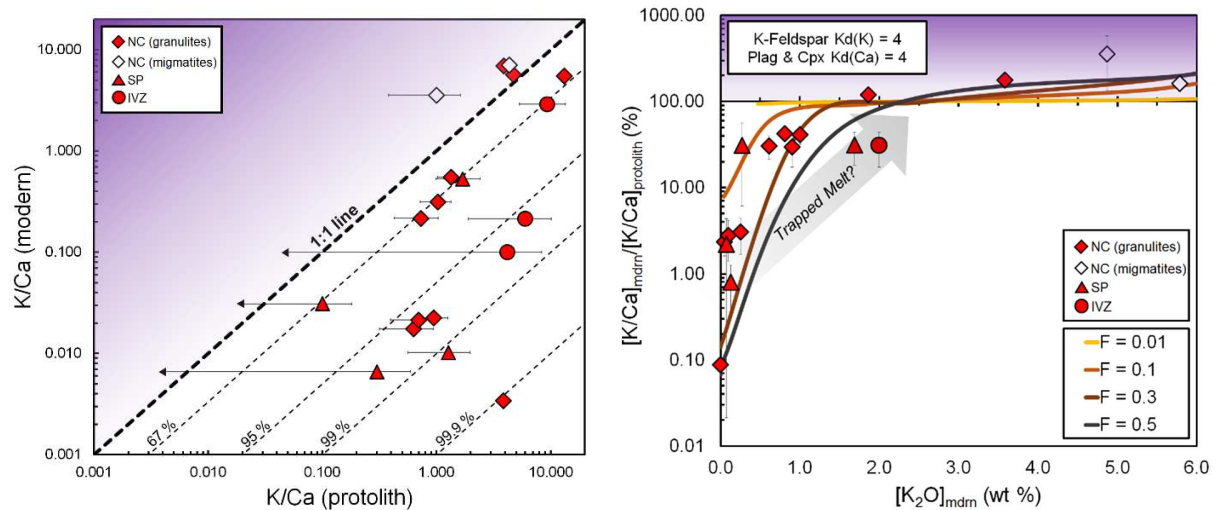
1347 loss in future studies.

1348

1349 **Fig. 25a,b. (a)** K/Ca modern *vs.* K/Ca protolith estimates based on garnet ε_{Ca} and protolith/metamorphic ages, and

1350 **(b)** $(K/Ca)_{mdrn}/(K/Ca)_{protolith}$ *vs.* modern whole rock K_2O (wt%) with melt-loss estimates based on a non-modal batch

1351 melting model, after Antonelli et al. (2019a). Arrow shows the potential effects of incomplete melt loss.

1352 **8. Conclusions and future work**

1353 In this review, we have shown that stable Ca isotope fractionations at high-temperatures can

1354 equal and often exceed those that occur in low-temperature surface environments. To date,

1355 igneous and metamorphic whole-rock analyses have $\delta^{44}Ca$ ranges of ~2‰ and ~6‰,

1356 respectively, indicative of open-system processes such as fractional crystallization, partial-melt

1357 loss, metamorphism/metasomatism, and diffusive Ca transport. Despite this observation, non-

1358 metasomatized peridotites have little $\delta^{44}Ca$ variability and define a bulk-silicate Earth (BSE)

1359 value of +0.95‰ relative to standard SRM915a, while mid-ocean ridge basalts and average

1360 continental crust have slightly lower $\delta^{44}Ca$ (by ~0.1‰ and ~0.2‰, respectively). Basaltic

1361 standards analyzed by TIMS generally give values closer to BSE, but this may be due to a

1362   +0.1‰ difference in $\delta^{44}Ca$ compared to the same standards analyzed by ICP-MS (where ^{40}Ca is

1363   not directly measured). This suggests that there may be slight excess ^{40}Ca in SRM915a (ε_{Ca} = +1

1364   relative to basaltic igneous rocks), and that BSE has lower $^{40}Ca/^{44}Ca$ [~47.156 *vs.* ~47.162

1365   (Antonelli et al., 2019a)], but further exploration is required.

1366   Although there have been no experimental constraints for equilibrium fractionation factors

1367   between minerals, *ab-initio* simulations have provided great insight into equilibrium Ca isotope

1368   fractionation at high temperatures. General agreement is reached between the various studies in

1369   spite of their different theoretical approaches. Likewise, the existing measurements of

1370   equilibrium slopes in triple Ca isotope space ($^{48}Ca/^{44}Ca$ *vs.* $^{42}Ca/^{44}Ca$) for samples that agree

1371   with *ab-initio* estimates, suggest that they are approximately correct. Thus, there is potential for

1372   using inter-mineral $\Delta^{44}Ca$ measurements for future geothermometry, especially in non-

1373   metasomatized plutonic rocks where minerals tend to have compositions closer to predicted

1374   equilibrium. For the moment, however, relatively common observations of inter-mineral

1375   disequilibrium preclude the use of Ca isotopes for geothermometry, and additional constraints

1376   (*e.g.* independent temperature estimates combined with *ab-initio* predictions, and/or $\Delta^{48}Ca$'

1377   measurements) are necessary in order to further understand the geologic environments in which

1378   isotopic equilibrium can be expected.

1379   The large $\Delta^{44}Ca$ fractionations observed between adjacent whole rocks (which can exceed 3‰)

1380   and between coexisting minerals (which can exceed 2‰) have slopes in triple Ca isotope space

1381   that agree with the predicted kinetic mass-fractionation law (based on Graham's law), suggesting

1382   that they are the result of Ca diffusion. Although modeling disequilibrium isotope fractionation

1383   can be more complicated than modeling equilibrium fractionation, Ca isotope diffusion models

1384   have been applied to natural samples and yield important information on (i) the timescales of

1385 mantle metasomatism, (ii) Ca transport mechanisms during lower crustal metamorphism, (iii)

1386 metamorphic mineral paragenesis, (iv) crystal growth rates in volcanic and sub-volcanic rocks,

1387 and (v) mineral precipitation rates in hydrothermal systems.

1388 Radiogenic ^{40}Ca variations (ε_{Ca}) are especially useful for source-tracing studies, as they are not

1389 complicated by the numerous stable isotope effects mentioned above. In rocks with known

1390 protolith and metamorphic ages, ε_{Ca} measurements can be used to estimate initial K/Ca values

1391 and constrain K-loss (and potentially K-gains) during metamorphism. Studies have also shown

1392 that ε_{Ca} can be used as a proxy for crustal contamination in mantle-derived continental magmas

1393 and (in combination with ε_{Nd}) to differentiate between lithospheric and asthenospheric mantle

1394 sources.

1395 The ε_{Ca} differences between (modern) carbonates and mantle, however, are not large enough to

1396 trace potential contributions from carbonate subduction in igneous samples. Although there is

1397 potential for using stable Ca isotopes for this purpose (due to low δ^{44}Ca values in rapidly-

1398 precipitated carbonates), this idea has recently been challenged by studies concluding that, on

1399 average, carbonates have the same δ^{44}Ca as BSE over the last several billion years, and that

1400 carbonatite metasomatism has no measurable effects in mantle samples. Thus, further studies are

1401 necessary in order to better constrain the situations in which δ^{44}Ca can be used as a tracer of

1402 carbonate subduction.

1403 In order to further advance our understanding of Ca isotope fractionations during high-

1404 temperature processes, future studies of natural samples should pay special attention to: (i)

1405 kinetic *vs.* equilibrium signatures (*e.g.* by using Δ^{48}Ca' measurements or independent

1406 temperature constraints combined with *ab-initio* estimates), (ii) spatial constraints and field

1407 relationships suggestive of initial chemical/temperature gradients or open-system processes, and

78

1408 (iii) detailed petrographic observations (including textural and paragenetic relationships). A

1409 greater number of experimental constraints, including inter-mineral equilibration (to verify

1410 fractionation factors), crystallization, melting, hydrothermal mineral precipitation, and diffusion-

1411 couple experiments would also be greatly beneficial. Finally, technical advancements such as (i)

1412 improved sampling (*e.g.* micro-drilling across mineral-zones or separation of specific crystal

1413 populations) and small sample analysis methods (*e.g.* TIMS analyses using next generation high-

1414 resistance amplifiers) and (ii) the development of in-situ Ca isotope analysis techniques (*e.g.* by

1415 SIMS or LA-MC-ICP-MS), would greatly enhance our understanding of the various processes

1416 leading to Ca isotope equilibrium and disequilibrium in high-temperature samples. Next

1417 generation CC-MC-ICP-MS instruments with low energy collision-cell technology should also

1418 allow ^{40}Ca, ^{42}Ca, ^{44}Ca, and ^{48}Ca to be measured without isobaric interferences from Ar-based

1419 polyatomic species (Simon, 2019; Zhao and Simon, 2019), which will be especially useful for

1420 determining Ca isotope variations (including ε_{Ca}, $\delta^{44}Ca$, and $\Delta^{48}Ca'$) in future studies.

1421 9. Acknowledgments

References

Amini, M., Eisenhauer, A., Böhm, F., Fietzke, J., Bach, W., Garbe-Schönberg, D., Rosner, M., Bock, B., Lackschewitz, K.S., Hauff, F., 2008. Calcium isotope (δ44/40Ca) fractionation along hydrothermal pathways, Logatchev field (Mid-Atlantic Ridge, 14 45 N). Geochim. Cosmochim. Acta 72, 4107–4122. https://doi.org/10.1016/j.gca.2008.05.055

Amini, M., Eisenhauer, A., Böhm, F., Holmden, C., Kreissig, K., Hauff, F., Jochum, K.P., 2009. Calcium isotopes (d44/40Ca) in MPI-DING reference glasses, USGS rock powders and various rocks: Evidence for Ca isotope fractionation in terrestrial silicates. Geostand. Geoanalytical Res. 33, 231–247. https://doi.org/10.1111/j.1751-908X.2009.00903.x

Amsellem, E., Moynier, F., Pringle, E.A., Bouvier, A., Chen, H., Day, J.M.D.D., 2017. Testing the chondrule-rich accretion model for planetary embryos using calcium isotopes. Earth Planet. Sci. Lett. 469, 75–83. https://doi.org/10.1016/j.epsl.2017.04.022

Amsellem, E., Moynier, F., Puchtel, I.S., 2019. Evolution of the Ca isotopic composition of the mantle. Geochim. Cosmochim. Acta 258, 195–206. https://doi.org/10.1016/j.gca.2019.05.026

Antonelli, M.A., Depaolo, D.J., Brown, S.T., Pester, N.J., 2018. Radiogenic 40Ca in Seawater, in: Goldschmidt Conference 2018, Boston, MA.

Antonelli, M.A., DePaolo, D.J., Chacko, T., Grew, E.S., Rubatto, D., 2019a. Radiogenic Ca isotopes confirm post-formation K depletion of lower crust. Geochemical Perspect. Lett. 9, 43–48. https://doi.org/10.7185/geochemlet.1904

Antonelli, M.A., Mittal, T., McCarthy, A., Tripoli, B., Watkins, J.M., DePaolo, D.J., 2019b. Ca isotopes record rapid crystal growth in volcanic and subvolcanic systems. Proc. Natl. Acad. Sci. 201908921. https://doi.org/10.1073/pnas.1908921116

Antonelli, M.A., Pester, N.J., Brown, S.T., DePaolo, D.J., 2017. Effect of paleoseawater composition on hydrothermal exchange in midocean ridges. Proc. Natl. Acad. Sci. 114, 201709145. https://doi.org/10.1073/pnas.1709145114

Antonelli, M.A., Schiller, M., Schauble, E.A., Mittal, T., DePaolo, D.J., Chacko, T., Grew, E.S., Tripoli, B., 2019c. Kinetic and equilibrium Ca isotope effects in high-T rocks and minerals. Earth Planet. Sci. Lett. 517, 71–82. https://doi.org/10.1016/j.epsl.2019.04.013

Arzilli, F., Mancini, L., Voltolini, M., Cicconi, M.R., Mohammadi, S., Giuli, G., Mainprice, D., Paris, E., Barou, F., Carroll, M.R., 2015. Near-liquidus growth of feldspar spherulites in trachytic melts: 3D morphologies and implications in crystallization mechanisms. Lithos 216–217, 93–105. https://doi.org/10.1016/j.lithos.2014.12.003

Baker, D.R., 1989. Tracer versus trace element diffusion: Diffusional decoupling of Sr concentration from Sr isotope composition. Geochim. Cosmochim. Acta 53, 3015–3023. https://doi.org/10.1016/0016-7037(89)90177-4

Banerjee, A., Chakrabarti, R., 2019. A geochemical and Nd, Sr and stable Ca isotopic study of carbonatites and associated silicate rocks from the ~65 Ma old Ambadongar carbonatite complex and the Phenai Mata igneous complex, Gujarat, India. LITHOS 326–327. https://doi.org/10.1016/j.lithos.2019.01.007

Banerjee, A., Chakrabarti, R., 2018. Large Ca stable isotopic (δ44/40Ca) variation in a hand-specimen sized spheroidally weathered diabase due to selective weathering of clinopyroxene and plagioclase. Chem. Geol. 483, 295–303. https://doi.org/10.1016/j.chemgeo.2018.02.031

Bessey, C., 2018. Calcium Isotope Fractionation in Coexisting Minerals. BSc Thesis, University of Waterloo.

1471 Bigeleisen, J., Mayer, M.G., 1947. Calculation of Equilibrium Constants for Isotopic Exchange
1472   Reactions. J. Chem. Phys. 15, 261–267. https://doi.org/10.1063/1.1746492

1473 Blättler, C.L., Higgins, J.A., 2017. Testing Urey's carbonate–silicate cycle using the calcium isotopic
1474   composition of sedimentary carbonates. Earth Planet. Sci. Lett. 479, 241–251.
1475   https://doi.org/10.1016/j.epsl.2017.09.033

1476 Blichert-Toft, J., 1999. Hf Isotope Evidence for Pelagic Sediments in the Source of Hawaiian Basalts.
1477   Science (80-.). 285, 879–882. https://doi.org/10.1126/science.285.5429.879

1478 Brey, G.P., Kohler, T., 1990. Geothermobarometry in 4-phase lherzolites .2. New thermobarometers, and
1479   practical assessment of existing thermobarometers. J. Petrol. 31, 1353–1378.

1480 Brown, S.T., Kennedy, B.M., DePaolo, D.J., Hurwitz, S., Evans, W.C., 2013. Ca, Sr, O and D isotope
1481   approach to defining the chemical evolution of hydrothermal fluids: Example from Long Valley,
1482   CA, USA. Geochim. Cosmochim. Acta 122, 209–225.

1483 Brown, S.T., Turchyn, A. V., Bickle, M.J., Davis, A.C., Alt, J.C., Bédard, J.H., Skulski, T., Bedard, J.H.,
1484   Skulski, T., DePaolo, D.J., 2020. High-temperature kinetic isotope fractionation of calcium in
1485   epidosites from modern and ancient seafloor hydrothermal systems. Earth Planet. Sci. Lett. 535.
1486   https://doi.org/10.1016/j.epsl.2020.116101

1487 Brugger, C.R., Hammer, J.E., 2010. Crystal size distribution analysis of plagioclase in experimentally
1488   decompressed hydrous rhyodacite magma. Earth Planet. Sci. Lett. 300, 246–254.
1489   https://doi.org/10.1016/j.epsl.2010.09.046

1490 Caro, G., Papanastassiou, D. a., Wasserburg, G.J., 2010. 40K-40Ca isotopic constraints on the oceanic
1491   calcium cycle. Earth Planet. Sci. Lett. 296, 124–132. https://doi.org/10.1016/j.epsl.2010.05.001

1492 Castillo, P.R., MacIsaac, C., Perry, S., Veizer, J., 2018. Marine Carbonates in the Mantle Source of
1493   Oceanic Basalts: Pb Isotopic Constraints. Sci. Rep. 8, 14932. https://doi.org/10.1038/s41598-018-
1494   33178-4

1495 Chacko, T., Cole, D.R., Horita, J., 2001. Equilibrium Oxygen, Hydrogen and Carbon Isotope
1496   Fractionation Factors Applicable to Geologic Systems. Rev. Mineral. Geochemistry 43, 1–81.
1497   https://doi.org/10.2138/gsrmg.43.1.1

1498 Chakrabarti, R., Acharya, S.S., Mondal, S., 2018. Large stable Ca isotopic (δ44/40 Ca) variation in open
1499   ocean samples from the Bay of Bengal, in: Goldschmidt 2018.

1500 Chen, C., Ciazela, J., Li, W., Dai, W., Wang, Z., Foley, S.F., Li, M., Hu, Z., Liu, Y., 2019a. Calcium
1501   isotopic compositions of oceanic crust at various spreading rates. Geochim. Cosmochim. Acta.
1502   https://doi.org/10.1016/j.gca.2019.07.008

1503 Chen, C., Dai, W., Wang, Z., Liu, Y., Li, M., Becker, H., Foley, S.F., 2019b. Calcium isotope
1504   fractionation during magmatic processes in the upper mantle. Geochim. Cosmochim. Acta 249,
1505   121–137. https://doi.org/10.1016/j.gca.2019.01.031

1506 Chen, C., Liu, Y., Feng, L., Foley, S.F., Zhou, L., Ducea, M.N., Hu, Z., 2018. Calcium isotope evidence
1507   for subduction-enriched lithospheric mantle under the northern North China Craton. Geochim.
1508   Cosmochim. Acta 238, 55–67. https://doi.org/10.1016/j.gca.2018.06.038

1509 Clayton, R.N., 1959. Oxygen Isotope Fractionation in the System Calcium Carbonate-Water. J. Chem.
1510   Phys. 30, 1246–1250. https://doi.org/10.1063/1.1730165

1511 Colla, C.A., Wimpenny, J., Yin, Q.Z., Rustad, J.R., Casey, W.H., 2013. Calcium-isotope fractionation
1512   between solution and solids with six, seven or eight oxygens bound to Ca(II). Geochim.
1513   Cosmochim. Acta 121, 363–373. https://doi.org/10.1016/j.gca.2013.07.041

1514 Cooper, K.M., 2019. Time scales and temperatures of crystal storage in magma reservoirs: implications
1515   for magma reservoir dynamics. Philos. Trans. R. Soc. A Math. Phys. Eng. Sci. 377, 20180009.
1516   https://doi.org/10.1098/rsta.2018.0009

1517 Cooper, K.M., Kent, A.J.R., 2014. Rapid remobilization of magmatic crystals kept in cold storage. Nature
1518   506, 480–483. https://doi.org/10.1038/nature12991

1519 Coplen, T.B., 2011. Guidelines and recommended terms for expression of stable-isotope-ratio and gas-
1520   ratio measurement results. Rapid Commun. Mass Spectrom. 25, 2538–2560.
1521   https://doi.org/10.1002/rcm.5129

1522 Dai, W., Wang, Z., Liu, Y., Chen, C., Zong, K., Zhou, L., Zhang, G., Li, M., Moynier, F., Hu, Z., 2020.
1523   Calcium isotope compositions of mantle pyroxenites. Geochim. Cosmochim. Acta 270, 144–159.
1524   https://doi.org/10.1016/j.gca.2019.11.024

1525 Dasgupta, R., Hirschmann, M.M., Withers, A.C., 2004. Deep global cycling of carbon constrained by the
1526   solidus of anhydrous, carbonated eclogite under upper mantle conditions. Earth Planet. Sci. Lett.
1527   227, 73–85. https://doi.org/10.1016/j.epsl.2004.08.004

1528 Dauphas, N., Roskosz, M., Alp, E.E., Golden, D.C., Sio, C.K., Tissot, F.L.H., Hu, M.Y., Zhao, J., Gao,
1529   L., Morris, R. V., 2012. A general moment NRIXS approach to the determination of equilibrium Fe
1530   isotopic fractionation factors: Application to goethite and jarosite. Geochim. Cosmochim. Acta 94,
1531   254–275. https://doi.org/10.1016/j.gca.2012.06.013

1532 De La Rocha, C.L., 2000. Isotopic Evidence for Variations in the Marine Calcium Cycle Over the
1533   Cenozoic. Science (80-.). 289, 1176–1178. https://doi.org/10.1126/science.289.5482.1176

1534 DePaolo, D.J., 2011. Surface kinetic model for isotopic and trace element fractionation during
1535   precipitation of calcite from aqueous solutions. Geochim. Cosmochim. Acta 75, 1039–1056.
1536   https://doi.org/10.1016/j.gca.2010.11.020

1537 DePaolo, D.J., 2004. Calcium Isotopic Variations Produced by Biological, Kinetic, Radiogenic and
1538   Nucleosynthetic Processes. Rev. Mineral. Geochemistry 55, 255–288.
1539   https://doi.org/10.2138/gsrmg.55.1.255

1540 DePaolo, D.J., 1981. Trace element and isotopic effects of combined wallrock assimilation and fractional
1541   crystallization. Earth Planet. Sci. Lett. 53, 189–202. https://doi.org/10.1016/0012-821X(81)90153-9

1542 DePaolo, D.J., Wasserburg, G.J., 1979. Sm-Nd age of the Stillwater complex and the mantle evolution
1543   curve for neodymium. Geochim. Cosmochim. Acta 43, 999–1008. https://doi.org/10.1016/0016-
1544   7037(79)90089-9

1545 Dohmen, R., Milke, R., 2010. Diffusion in Polycrystalline Materials: Grain Boundaries, Mathematical
1546   Models, and Experimental Data. Rev. Mineral. Geochemistry 72, 921–970.
1547   https://doi.org/10.2138/rmg.2010.72.21

1548 Dominguez, G., Wilkins, G., Thiemens, M.H., 2011. The Soret effect and isotopic fractionation in high-
1549   temperature silicate melts. Nature 473, 70–73. https://doi.org/10.1038/nature09911

1550 Ewing, T.A., Rubatto, D., Hermann, J., 2014. Hafnium isotopes and Zr/Hf of rutile and zircon from lower
1551   crustal metapelites (Ivrea-Verbano Zone, Italy): Implications for chemical differentiation of the
1552   crust. Earth Planet. Sci. Lett. 389, 106–118. https://doi.org/10.1016/j.epsl.2013.12.029

1553 Fantle, M.S., DePaolo, D.J., 2005. Variations in the marine Ca cycle over the past 20 million years. Earth
1554   Planet. Sci. Lett. 237, 102–117. https://doi.org/10.1016/j.epsl.2005.06.024

1555 Fantle, M.S., Tipper, E.T., 2014. Calcium isotopes in the global biogeochemical Ca cycle: Implications
1556   for development of a Ca isotope proxy. Earth-Science Rev. 129, 148–177.
1557   https://doi.org/10.1016/j.earscirev.2013.10.004

1558 Farkaš, J., Buhl, D., Blenkinsop, J., Veizer, J., 2007. Evolution of the oceanic calcium cycle during the
1559   late Mesozoic: Evidence from δ44/40Ca of marine skeletal carbonates. Earth Planet. Sci. Lett. 253,
1560   96–111. https://doi.org/10.1016/j.epsl.2006.10.015

1561 Farver, J.R., Yund, R.A., 1995. Grain-Boundary Diffusion of Oxygen, Potassium and Calcium in Natural
1562   and Hot-Pressed Feldspar Aggregates. Contrib. to Mineral. Petrol. 118, 340–355.
1563   https://doi.org/10.1007/s004100050019

1564 Feng, C., Qin, T., Huang, S., Wu, Z., Huang, F., 2014. First-principles investigations of equilibrium
1565   calcium isotope fractionation between clinopyroxene and Ca-doped orthopyroxene. Geochim.
1566   Cosmochim. Acta 143, 132–142. https://doi.org/10.1016/j.gca.2014.06.002

1567 Feng, L., Zhou, L., Yang, L., DePaolo, D.J., Tong, S.-Y., Liu, Y.-S., Owens, T.L., Gao, S., 2016. Calcium
1568   Isotopic Compositions of Sixteen USGS Reference Materials. Geostand. Geoanalytical Res. 41, 93–
1569   106. https://doi.org/10.1111/ggr.12131

1570 Feng, L., Zhou, L., Yang, L., Zhang, W., Wang, Q., Shuoyun, T., Hu, Z., 2018. A rapid and simple
1571   single-stage method for Ca separation from geological and biological samples for isotopic analysis
1572   by MC-ICP-MS. J. Anal. At. Spectrom. 33, 413–421. https://doi.org/10.1039/c7ja00370f

1573 Frey, F.., Garcia, M.., Roden, M.., 1994. Geochemical characteristics of Koolau Volcano: Implications of
1574   intershield geochemical differences among Hawaiian volcanoes. Geochim. Cosmochim. Acta 58,
1575   1441–1462. https://doi.org/10.1016/0016-7037(94)90548-7

1576 Giletti, B.J., 1994. Isotopic Equilibrium/Disequilibrium and Diffusion Kinetics in Feldspars, in: Parsons,
1577   I. (Ed.), Feldspars and Their Reactions. Springer Netherlands, Dordrecht, pp. 351–382.
1578   https://doi.org/10.1007/978-94-011-1106-5_9

1579 Griffith, E.M., Paytan, A., Caldeira, K., Bullen, T.D., Thomas, E., 2008a. A Dynamic Marine Calcium
1580   Cycle During the Past 28 Million Years. Science (80-.). 322, 1671–1674.
1581   https://doi.org/10.1126/science.1163614

1582 Griffith, E.M., Schauble, E.A., Bullen, T.D., Paytan, A., 2008b. Characterization of calcium isotopes in
1583   natural and synthetic barite. Geochim. Cosmochim. Acta 72, 5641–5658.
1584   https://doi.org/10.1016/j.gca.2008.08.010

1585 Hawkesworth, C.J., Van Calsteren, P.W.C., 1984. Radiogenic Isotopes – Some Geological Applications.
1586   pp. 375–421. https://doi.org/10.1016/B978-0-444-42148-7.50016-2

1587 He, Y., Wang, Y., Zhu, C., Huang, S., Li, S., 2017. Mass-Independent and Mass-Dependent Ca Isotopic
1588   Compositions of Thirteen Geological Reference Materials Measured by Thermal Ionisation Mass
1589   Spectrometry. Geostand. Geoanalytical Res. 41, 283–302. https://doi.org/10.1111/ggr.12153

1590 Heuser, A., Eisenhauer, A., Böhm, F., Wallmann, K., Gussone, N., Pearson, P.N., Nägler, T.F., Dullo,
1591   W.-C., 2005. Calcium isotope (δ 44/40 Ca) variations of Neogene planktonic foraminifera.
1592   Paleoceanography 20, n/a-n/a. https://doi.org/10.1029/2004PA001048

1593 Holmden, C., Bélanger, N., 2010. Ca isotope cycling in a forested ecosystem. Geochim. Cosmochim.
1594   Acta 74, 995–1015. https://doi.org/10.1016/j.gca.2009.10.020

1595 Holycross, M.E., Watson, E.B., Richter, F.M., Villeneuve, J., 2018. Diffusive fractionation of Li isotopes
1596   in wet, silicic melts. Geochemical Perspect. Lett. 39–42. https://doi.org/10.7185/geochemlet.1807

1597 Huang, F., Chakraborty, P., Lundstrom, C.C.C., Holmden, C.E., Glessner, J.J.G.J.G., Kieffer, S.W.,
1598   Lesher, C.E.E., 2010. Isotope fractionation in silicate melts by thermal diffusion. Nature 464, 396–
1599   400. https://doi.org/10.1038/nature08840

1600 Huang, F., Zhou, C., Wang, W., Kang, J., Wu, Z., 2019. First-principles calculations of equilibrium Ca
1601   isotope fractionation : Implications for oldhamite formation and evolution of lunar magma ocean.

1602   Earth Planet. Sci. Lett. 510, 153–160. https://doi.org/10.1016/j.epsl.2018.12.034

1603   Huang, S., Abouchami, W., Blichert-Toft, J., Clague, D.A., Cousens, B.L., Frey, F.A., Humayun, M.,
1604   2009. Ancient carbonate sedimentary signature in the Hawaiian plume: Evidence from Mahukona
1605   volcano, Hawaii. Geochemistry, Geophys. Geosystems 10, n/a-n/a.
1606   https://doi.org/10.1029/2009GC002418

1607   Huang, S., Farkaš, J., Jacobsen, S.B., 2011. Stable calcium isotopic compositions of Hawaiian shield
1608   lavas: Evidence for recycling of ancient marine carbonates into the mantle. Geochim. Cosmochim.
1609   Acta 75, 4987–4997. https://doi.org/10.1016/j.gca.2011.06.010

1610   Huang, S., Farkaš, J., Jacobsen, S.B., 2010. Calcium isotopic fractionation between clinopyroxene and
1611   orthopyroxene from mantle peridotites. Earth Planet. Sci. Lett. 292, 337–344.
1612   https://doi.org/10.1016/j.epsl.2010.01.042

1613   Huang, S., Frey, F.A., 2005. Recycled oceanic crust in the Hawaiian Plume: evidence from temporal
1614   geochemical variations within the Koolau Shield. Contrib. to Mineral. Petrol. 149, 556–575.
1615   https://doi.org/10.1007/s00410-005-0664-9

1616   Ionov, D.A., Qi, Y.-H., Kang, J.-T., Golovin, A. V., Oleinikov, O.B., Zheng, W., Anbar, A.D., Zhang, Z.-
1617   F., Huang, F., 2019. Calcium isotopic signatures of carbonatite and silicate metasomatism, melt
1618   percolation and crustal recycling in the lithospheric mantle. Geochim. Cosmochim. Acta 248, 1–13.
1619   https://doi.org/10.1016/j.gca.2018.12.023

1620   Jacobson, A.D., Grace Andrews, M., Lehn, G.O., Holmden, C., 2015. Silicate versus carbonate
1621   weathering in Iceland: New insights from Ca isotopes. Earth Planet. Sci. Lett. 416, 132–142.
1622   https://doi.org/10.1016/j.epsl.2015.01.030

1623   Jochum, K.P., Stoll, B., Herwig, K., Willbold, M., Hofmiann, A.W., Amini, M., Aarburg, S., Abouchami,
1624   W., Hellebrand, E., Mocek, B., Raczek, I., Stracke, A., Alard, O., Bouman, C., Becker, S., Dücking,
1625   M., Brätz, H., Klemd, R., De Bruin, D., Canil, D., Cornell, D., De Hoog, C.J., Dalpé, C.,
1626   Danyushevshy, L., Eisenhauer, A., Gao, Y., Snow, J.E., Groschopf, N., Günther, D., Latkoczy, C.,
1627   Guillong, M., Hauri, E.H., Höfer, H.E., Lahaye, Y., Horz, K., Jacob, D.E., Kasemann, S.A., Kent,
1628   A.J.R., Ludwig, T., Zack, T., Mason, P.R.D., Meixner, A., Rosner, M., Misawa, K., Nash, B.P.,
1629   Pfänder, J., Premo, W.R., Sun, W.D., Tiepolo, M., Vannucci, R., Vennemann, T., Wayne, D.,
1630   Woodhead, J.D., 2006. MPI-DING reference glasses for in situ microanalysis: New reference values
1631   for element concentrations and isotope ratios. Geochemistry, Geophys. Geosystems 7.
1632   https://doi.org/10.1029/2005GC001060

1633   John, T., Gussone, N., Podladchikov, Y.Y., Bebout, G.E., Dohmen, R., Halama, R., Klemd, R., Magna,
1634   T., Seitz, H.M., 2012. Volcanic arcs fed by rapid pulsed fluid flow through subducting slabs. Nat.
1635   Geosci. 5, 489–492. https://doi.org/10.1038/ngeo1482

1636   Kaercher, P., Militzer, B., Wenk, H.-R., 2014. Ab initio Calculations of Elastic Constants of Plagioclase
1637   feldspars. Am. Mineral. 99, 2344–2352. https://doi.org/10.2138/am-2014-4796

1638   Kang, J.-T.T., Ionov, D.A., Zhu, H.-L.L., Liu, F., Zhang, Z.-F.F., Liu, Z., Huang, F., 2019. Calcium
1639   isotope sources and fractionation during melt-rock interaction in the lithospheric mantle: Evidence
1640   from pyroxenites, wehrlites, and eclogites. Chem. Geol. 524, 272–282.
1641   https://doi.org/10.1016/j.chemgeo.2019.06.010

1642   Kang, J.T., Ionov, D.A., Liu, F., Zhang, C.L., Golovin, A. V., Qin, L.P., Zhang, Z.F., Huang, F., 2017.
1643   Calcium isotopic fractionation in mantle peridotites by melting and metasomatism and Ca isotope
1644   composition of the Bulk Silicate Earth. Earth Planet. Sci. Lett. 474, 128–137.
1645   https://doi.org/10.1016/j.epsl.2017.05.035

1646   Kang, J.T., Zhu, H.L., Liu, Y.F., Liu, F., Wu, F., Hao, Y.T., Zhi, X.C., Zhang, Z.F., Huang, F., 2016.

1647   Calcium isotopic composition of mantle xenoliths and minerals from Eastern China. Geochim.
1648   Cosmochim. Acta 174, 335–344. https://doi.org/10.1016/j.gca.2015.11.039

1649   Kasemann, S.A., Hawkesworth, C.J., Prave, A.R., Fallick, A.E., Pearson, P.N., 2005. Boron and calcium
1650   isotope composition in Neoproterozoic carbonate rocks from Namibia: evidence for extreme
1651   environmental change. Earth Planet. Sci. Lett. 231, 73–86.
1652   https://doi.org/10.1016/j.epsl.2004.12.006

1653   Keller, L.M., Wirth, R., Rhede, D., Kunze, K., Abart, R., 2008. Asymmetrically zoned reaction rims:
1654   Assessment of grain boundary diffusivities and growth rates related to natural diffusion-controlled
1655   mineral reactions. J. Metamorph. Geol. 26, 99–120. https://doi.org/10.1111/j.1525-
1656   1314.2007.00747.x

1657   Kueter, N., Lilley, M.D., Schmidt, M.W., Bernasconi, S.M., 2019. Experimental carbonatite/graphite
1658   carbon isotope fractionation and carbonate/graphite geothermometry. Geochim. Cosmochim. Acta
1659   253, 290–306. https://doi.org/10.1016/j.gca.2019.03.020

1660   Laan, S. Van Der, Zhang, Y., Kennedy, A.K., Wyllie, P.J., 1994. Comparison of element and isotope
1661   diffusion of K and Ca in multicomponent silicate melts. Earth Planet. Sci. Lett. 123, 155–166.

1662   Lassiter, J.C., Hauri, E.H., 1998. Osmium-isotope variations in Hawaiian lavas: evidence for recycled
1663   oceanic lithosphere in the Hawaiian plume. Earth Planet. Sci. Lett. 164, 483–496.
1664   https://doi.org/10.1016/S0012-821X(98)00240-4

1665   Lehn, G.O., Jacobson, A.D., 2015. Optimization of a 48Ca–43Ca double-spike MC-TIMS method for
1666   measuring Ca isotope ratios (δ44/40Ca and δ44/42Ca): limitations from filament reservoir mixing. J.
1667   Anal. At. Spectrom. 30, 1571–1581. https://doi.org/10.1039/C4JA00412D

1668   Lesher, C.E., 1994. Kinetics of Sr and Nd exchange in silicate liquids: theory, experiments, and
1669   applications to uphill diffusion, isotopic equilibration, and irreversible mixing of magmas. J.
1670   Geophys. Res. 99, 9585–9604. https://doi.org/10.1029/94JB00469

1671   Lesher, C.E., 1990. Decoupling of chemical and isotopic exchange during magma mixing. Nature.
1672   https://doi.org/10.1038/344235a0

1673   Liu, F., Li, X., Wang, G., Liu, Y., Zhu, H., Kang, J., Huang, F., Sun, W., Xia, X., Zhang, Z., 2017a.
1674   Marine Carbonate Component in the Mantle Beneath the Southeastern Tibetan Plateau: Evidence
1675   From Magnesium and Calcium Isotopes. J. Geophys. Res. Solid Earth 122, 9729–9744.
1676   https://doi.org/10.1002/2017JB014206

1677   Liu, F., Zhu, H.L., Li, X., Wang, G.Q., Zhang, Z.F., 2017b. Calcium Isotopic Fractionation and
1678   Compositions of Geochemical Reference Materials. Geostand. Geoanalytical Res. 41, 675–688.
1679   https://doi.org/10.1111/ggr.12172

1680   Lowenstein, T.K., Kendall, B., Anbar, a. D., 2013. The Geologic History of Seawater, 2nd ed, Treatise
1681   on Geochemistry: Second Edition. Elsevier Ltd. https://doi.org/10.1016/B978-0-08-095975-
1682   7.00621-5

1683   Lu, F., Anderson, A.T., Davis, A.M., 1995. Diffusional Gradients at the Crystal / Melt Interface and Their
1684   Effect on the Compositions of Melt Inclusions. J. Geol. 103, 591–597.

1685   Lu, W.-N., He, Y., Wang, Y., Ke, S., 2019. Behavior of calcium isotopes during continental subduction
1686   recorded in meta-basaltic rocks. Geochim. Cosmochim. Acta.
1687   https://doi.org/10.1016/j.gca.2019.09.027

1688   Magna, T., Gussone, N., Mezger, K., 2015. The calcium isotope systematics of Mars. Earth Planet. Sci.
1689   Lett. 430, 86–94. https://doi.org/10.1016/j.epsl.2015.08.016

1690   Marshall, B.D., DePaolo, D.J., 1989. Calcium isotopes in igneous rocks and the origin of granite.

1691   Geochim. Cosmochim. Acta 53, 917–922. https://doi.org/10.1016/0016-7037(89)90036-7

1692   Marshall, B.D., DePaolo, D.J., 1982. Precise age determinations and petrogenetic studies using the KCa
1693   method. Geochim. Cosmochim. Acta 46, 2537–2545. https://doi.org/10.1016/0016-7037(82)90376-
1694   3

1695   Matsuhisa, Y., Goldsmith, J.R., Clayton, R.N., 1978. Mechanisms of hydrothermal crystallization of
1696   quartz at 250°C and 15 kbar. Geochim. Cosmochim. Acta 42, 173–182.
1697   https://doi.org/10.1016/0016-7037(78)90130-8

1698   Matthews, A., 1976. Magnetite formation by the reduction of hematite with iron under hydrothermal
1699   conditions. Am. Mineral. 61, 927–932.

1700   McCarthy, A., Müntener, O., 2016. Comb layering monitors decompressing and fractionating hydrous
1701   mafic magmas in subvolcanic plumbing systems (Fisher Lake, Sierra Nevada, USA). J. Geophys.
1702   Res. Solid Earth 121, 8595–8621. https://doi.org/10.1002/2016JB013489

1703   McCoy-West, A.J., Fitton, J.G., Pons, M.L., Inglis, E.C., Williams, H.M., 2018. The Fe and Zn isotope
1704   composition of deep mantle source regions: Insights from Baffin Island picrites. Geochim.
1705   Cosmochim. Acta 238, 542–562. https://doi.org/10.1016/j.gca.2018.07.021

1706   Mills, R.D., Simon, J.I., DePaolo, D.J., 2018. Calcium and neodymium radiogenic isotopes of igneous
1707   rocks: Tracing crustal contributions in felsic magmas related to super-eruptions and continental
1708   rifting. Earth Planet. Sci. Lett. 495, 242–250. https://doi.org/10.1016/j.epsl.2018.05.017

1709   O'Neil, J.R., Taylor, H.P., 1969. Oxygen isotope equilibrium between muscovite and water. J. Geophys.
1710   Res. 74, 6012–6022. https://doi.org/10.1029/JB074i025p06012

1711   O'Neil, J.R., Taylor, H.P., 1967. The oxygen isotope and cation exchange chemistry of feldspars. Am.
1712   Mineral. 52, 1414–1437.

1713   Olsen, M.B., Schiller, M., Krot, A.N., Bizzarro, M., 2013. Magnesium isotope evidence for single stage
1714   formation of CB chondrules by colliding planetesimals. Astrophys. J. 776, L1.
1715   https://doi.org/10.1088/2041-8205/776/1/L1

1716   Peterson, B.T., 2013. Rates and Mechanisms of Magmatic Processes: Isotopic and Geochronological
1717   Evidence. University of California, Berkeley.

1718   Plank, T., Langmuir, C.H., 1998. The chemical composition of subducting sediment and its consequences
1719   for the crust and mantle. Chem. Geol. 145, 325–394. https://doi.org/10.1016/S0009-2541(97)00150-
1720   2

1721   Putirka, K.D., 2005. Mantle potential temperatures at Hawaii, Iceland, and the mid-ocean ridge system, as
1722   inferred from olivine phenocrysts: Evidence for thermally driven mantle plumes. Geochemistry,
1723   Geophys. Geosystems 6, n/a-n/a. https://doi.org/10.1029/2005GC000915

1724   Rappoport, D., Crawford, N.R.M., Furche, F., Burke, K., 2011. Approximate Density Functionals: Which
1725   Should I Choose? Encycl. Inorg. Bioinorg. Chem. https://doi.org/10.1002/9781119951438.eibc0380

1726   Richter, F.M., Davis, A.M., DePaolo, D.J., Watson, E.B., 2003. Isotope fractionation by chemical
1727   diffusion between molten basalt and rhyolite. Geochim. Cosmochim. Acta 67, 3905–3923.
1728   https://doi.org/10.1016/S0016-7037(03)00174-1

1729   Richter, F.M., Liang, Y., Davis, A.M., 1999. Isotope fractionation by diffusion in molten oxides.
1730   Geochim. Cosmochim. Acta 63, 2853–2861. https://doi.org/10.1016/S0016-7037(99)00164-7

1731   Richter, F.M., Watson, E.B., Mendybaev, R., Dauphas, N., Georg, B., Watkins, J., Valley, J., 2009.
1732   Isotopic fractionation of the major elements of molten basalt by chemical and thermal diffusion.
1733   Geochim. Cosmochim. Acta 73, 4250–4263. https://doi.org/10.1016/j.gca.2009.04.011

1734 Rudnick, R.L., Gao, S., 2014. Composition of the Continental Crust, in: Treatise on Geochemistry.
1735   Elsevier Ltd., pp. 1–64. https://doi.org/http://dx.doi.org/10.1016/B0-08-043751-6/03016-4

1736 Rudnick, R.L., McLennan, S.M., Taylor, S.R., 1985. Large ion lithophile elements in rocks from high-
1737   pressure granulite facies terrains. Geochim. Cosmochim. Acta 49, 1645–1655.
1738   https://doi.org/10.1016/0016-7037(85)90268-6

1739 Russell, W.A., Papanastassiou, D.A., Tombrello, T.A., 1978. Ca isotope fractionation on the Earth and
1740   other solar system materials. Geochim. Cosmochim. Acta 42, 1075–1090.
1741   https://doi.org/10.1016/0016-7037(78)90105-9

1742 Ryu, J.S., Jacobson, A.D., Holmden, C., Lundstrom, C., Zhang, Z., 2011. The major ion, d44/40Ca,
1743   d44/42Ca, and d26/24Mg geochemistry of granite weathering at pH=1 and T=25 C: Power-law
1744   processes and the relative reactivity of minerals. Geochim. Cosmochim. Acta 75, 6004–6026.
1745   https://doi.org/10.1016/j.gca.2011.07.025

1746 Salisbury, M.J., Bohrson, W.A., Clynne, M.A., Ramos, F.C., Hoskin, P., 2008. Multiple plagioclase
1747   crystal populations identified by crystal size distribution and in situ chemical data: Implications for
1748   timescales of magma chamber processes associated with the 1915 eruption of Lassen Peak, CA. J.
1749   Petrol. 49, 1755–1780. https://doi.org/10.1093/petrology/egn045

1750 Scheuermann, P.P., Syverson, D.D., Higgins, J.A., Pester, N.J., Seyfried, W.E., 2018. Calcium isotope
1751   systematics at hydrothermal conditions: Mid-ocean ridge vent fluids and experiments in the CaSO4-
1752   NaCl-H2O system. Geochim. Cosmochim. Acta 226, 18–35.
1753   https://doi.org/10.1016/j.gca.2018.01.028

1754 Schiller, M., Paton, C., Bizzarro, M., 2012. Calcium isotope measurement by combined HR-MC-ICPMS
1755   and TIMS. J. Anal. At. Spectrom. 27, 38–49. https://doi.org/10.1039/C1JA10272A

1756 Schmitt, A.D., Chabaux, F., Stille, P., 2003. The calcium riverine and hydrothermal isotopic fluxes and
1757   the oceanic calcium mass balance. Earth Planet. Sci. Lett. 213, 503–518.
1758   https://doi.org/10.1016/S0012-821X(03)00341-8

1759 Shahar, A., Young, E.D., Manning, C.E., 2008. Equilibrium high-temperature Fe isotope fractionation
1760   between fayalite and magnetite: An experimental calibration. Earth Planet. Sci. Lett. 268, 330–338.
1761   https://doi.org/10.1016/j.epsl.2008.01.026

1762 Shea, T., Hammer, J.E., 2013. Kinetics of cooling- and decompression-induced crystallization in hydrous
1763   mafic-intermediate magmas. J. Volcanol. Geotherm. Res. 260, 127–145.
1764   https://doi.org/10.1016/j.jvolgeores.2013.04.018

1765 Simon, J.I., 2019. Potential of MC-ICP-CC-MS in cosmochemistry and geochronology J, in: Goldschmidt
1766   2019.

1767 Simon, J.I., 2017. Utilizing Stable Isotopes and Isotopic Anomalies to Study Early Solar System
1768   Formation Processes, in: Accretion: Building New Worlds Conference 2017. Houston, p. 2pp.
1769   https://doi.org/10.12681/er.9602

1770 Simon, J.I., DePaolo, D.J., 2010. Stable calcium isotopic composition of meteorites and rocky planets.
1771   Earth Planet. Sci. Lett. 289, 457–466. https://doi.org/10.1016/j.epsl.2009.11.035

1772 Simon, J.I., DePaolo, D.J., Moynier, F., 2009. Calcium Isotope Composition of Meteorites, Earth, and
1773   Mars. Astrophys. J. 702, 707–715. https://doi.org/10.1088/0004-637X/702/1/707

1774 Simon, J.I., Jordan, M.K., Tappa, M.J., Schauble, E.A., Kohl, I.E., Young, E.D., 2017. Calcium and
1775   titanium isotope fractionation in refractory inclusions : Tracers of condensation and inheritance in
1776   the early solar protoplanetary disk. Earth Planet. Sci. Lett. 472, 277–288.
1777   https://doi.org/10.1016/j.epsl.2017.05.002

1778 Skulan, J., DePaolo, D.J., Owens, T.L., 1997. Biological control of calcium isotopic abundances in the
1779   global calcium cycle. Geochim. Cosmochim. Acta 61, 2505–2510. https://doi.org/10.1016/S0016-
1780   7037(97)00047-1

1781 Song, Y., Li, Y., Wang, W., Wu, Z., 2019. First-principles investigation of the concentration effect on
1782   equilibrium fractionation of Ca isotopes in forsterite. Acta Geochim. https://doi.org/10.1007/s11631-
1783   019-00346-w

1784 Staudigel, H., 2003. Hydrothermal alteration processes in the oceanic crust. Treatise on geochemistry
1785   511–535.

1786 Stepanov, A.S., Hermann, J., Korsakov, A. V., Rubatto, D., 2014. Geochemistry of ultrahigh-pressure
1787   anatexis: Fractionation of elements in the Kokchetav gneisses during melting at diamond-facies
1788   conditions. Contrib. to Mineral. Petrol. 167, 1–25. https://doi.org/10.1007/s00410-014-1002-x

1789 Syverson, D.D., Scheuermann, P., Higgins, J.A., Pester, N.J., Seyfried, W.E., 2018. Experimental
1790   partitioning of Ca isotopes and Sr into anhydrite: Consequences for the cycling of Ca and Sr in
1791   subseafloor mid-ocean ridge hydrothermal systems. Geochim. Cosmochim. Acta.
1792   https://doi.org/10.1016/j.gca.2018.03.018

1793 Turchyn, A. V., Alt, J.C., Brown, S.T., DePaolo, D.J., Coggon, R.M., Chi, G., Bédard, J.H., Skulski, T.,
1794   2013. Reconstructing the oxygen isotope composition of late Cambrian and Cretaceous
1795   hydrothermal vent fluid. Geochim. Cosmochim. Acta 123, 440–458.
1796   https://doi.org/10.1016/j.gca.2013.08.015

1797 Turchyn, A. V., DePaolo, D.J., 2019. Seawater Chemistry Through Phanerozoic Time. Annu. Rev. Earth
1798   Planet. Sci. 47, 197–224. https://doi.org/10.1146/annurev-earth-082517-010305

1799 Urey, H.C., 1947. The thermodynamic properties of isotopic substances. J. Chem. Soc. 562.
1800   https://doi.org/10.1039/jr9470000562

1801 Valdes, M.C., Debaille, V., Berger, J., Armytage, R.M.G., 2019. The effects of high-temperature
1802   fractional crystallization on calcium isotopic composition. Chem. Geol. #pagerange#.
1803   https://doi.org/10.1016/J.CHEMGEO.2019.01.012

1804 Valdes, M.C., Moreira, M., Foriel, J., Moynier, F., 2014. The nature of Earth's building blocks as
1805   revealed by calcium isotopes. Earth Planet. Sci. Lett. 394, 135–145.
1806   https://doi.org/10.1016/j.epsl.2014.02.052

1807 Vielzeuf, D., Baronnet, A., Perchuk, A.L., Laporte, D., Baker, M.B., 2007. Calcium diffusivity in
1808   alumino-silicate garnets: An experimental and ATEM study. Contrib. to Mineral. Petrol. 154, 153–
1809   170. https://doi.org/10.1007/s00410-007-0184-x

1810 von Damm, K.L., 2000. Chemistry of hydrothermal vent fluids from
1811   9{\textdegree}{\textendash}10{\textdegree}N, East Pacific Rise: {\textquotedblleft}Time
1812   zero,{\textquotedblright} the immediate posteruptive period. J. Geophys. Res. Solid Earth 105,
1813   11203–11222.

1814 Wang, W., Qin, T., Zhou, C., Huang, S., Wu, Z., Huang, F., 2017a. Concentration effect on equilibrium
1815   fractionation of Mg-Ca isotopes in carbonate minerals: Insights from first-principles calculations.
1816   Geochim. Cosmochim. Acta 208, 185–197. https://doi.org/10.1016/j.gca.2017.03.023

1817 Wang, W., Zhou, C., Qin, T., Kang, J.T., Huang, S., Wu, Z., Huang, F., 2017b. Effect of Ca content on
1818   equilibrium Ca isotope fractionation between orthopyroxene and clinopyroxene. Geochim.
1819   Cosmochim. Acta 219, 44–56. https://doi.org/10.1016/j.gca.2017.09.022

1820 Wang, Y., He, Y., Wu, H., Zhu, C., Huang, S., Huang, J., 2019. Calcium isotope fractionation during
1821   crustal melting and magma differentiation: Granitoid and mineral-pair perspectives. Geochim.

1822   Cosmochim. Acta 259, 37–52. https://doi.org/10.1016/j.gca.2019.05.030

1823   Watkins, J.M., DePaolo, D.J., Huber, C., Ryerson, F.J., 2009. Liquid composition-dependence of calcium
1824   isotope fractionation during diffusion in molten silicates. Geochim. Cosmochim. Acta 73, 7341–
1825   7359. https://doi.org/10.1016/j.gca.2009.09.004

1826   Watkins, J.M., DePaolo, D.J., Ryerson, F.J., Peterson, B.T., 2011. Influence of liquid structure on
1827   diffusive isotope separation in molten silicates and aqueous solutions. Geochim. Cosmochim. Acta
1828   75, 3103–3118. https://doi.org/10.1016/j.gca.2011.03.002

1829   Watkins, J.M., DePaolo, D.J., Watson, E.B., 2017. Kinetic Fractionation of Non-Traditional Stable
1830   Isotopes by Diffusion and Crystal Growth Reactions. Rev. Mineral. Geochemistry 82, 85–125.
1831   https://doi.org/10.2138/rmg.2017.82.4

1832   Watkins, J.M., Liang, Y., Richter, F., Ryerson, F.J., DePaolo, D.J., 2014. Diffusion of multi-isotopic
1833   chemical species in molten silicates. Geochim. Cosmochim. Acta 139, 313–326.
1834   https://doi.org/10.1016/j.gca.2014.04.039

1835   Watson, E.B., Müller, T., 2009. Non-equilibrium isotopic and elemental fractionation during diffusion-
1836   controlled crystal growth under static and dynamic conditions. Chem. Geol. 267, 111–124.
1837   https://doi.org/10.1016/j.chemgeo.2008.10.036

1838   Widanagamage, I.H., Schauble, E.A., Scher, H.D., Griffith, E.M., 2014. Stable strontium isotope
1839   fractionation in synthetic barite. Geochim. Cosmochim. Acta 147, 58–75.
1840   https://doi.org/10.1016/j.gca.2014.10.004

1841   Wiegand, B. a, Brehme, M., Kamah, Y., Sauter, M., 2015. Distribution of Sr and Ca Isotopes in Fluids of
1842   Lahendong Geothermal Field, in: World Geothermal Congress 2015. pp. 1–6.

1843   Wombacher, F., Eisenhauer, A., Heuser, A., Weyer, S., 2009. Separation of Mg, Ca and Fe from
1844   geological reference materials for stable isotope ratio analyses by MC-ICP-MS and double-spike
1845   TIMS. J. Anal. At. Spectrom. 24, 627. https://doi.org/10.1039/b820154d

1846   Yakymchuk, C., Brown, M., 2014. Consequences of open-system melting in tectonics. J. Geol. Soc.
1847   London. 171, 21–40. https://doi.org/10.1144/jgs2013-039

1848   Yokoyama, T., Misawa, K., Okano, O., Shih, C.Y., Nyquist, L.E., Simon, J.I., Tappa, M.J., Yoneda, S.,
1849   2017. Extreme early solar system chemical fractionation recorded by alkali-rich clasts contained in
1850   ordinary chondrite breccias. Earth Planet. Sci. Lett. 458, 233–240.
1851   https://doi.org/10.1016/j.epsl.2016.10.037

1852   Young, E.D., Galy, A., 2004. The Isotope Geochemistry and Cosmochemistry of Magnesium. Rev.
1853   Mineral. Geochemistry 55, 197–230. https://doi.org/10.2138/gsrmg.55.1.197

1854   Young, E.D., Galy, A., Nagahara, H., 2002. Kinetic and equilibrium mass-dependant isotope fractionation
1855   laws in nature and their geochemical and cosmochemical significance. Geochim. Cosmochim. Acta
1856   66, 1095–1104. https://doi.org/10.1016/S0016-7037(01)00832-8

1857   Zhang, H., Wang, Y., He, Y., Teng, F.-Z., Jacobsen, S.B., Helz, R.T., Marsh, B.D., Huang, S., 2018. No
1858   measurable calcium isotopic fractionation during crystallization of Kilauea Iki lava lake.
1859   Geochemistry, Geophys. Geosystems. https://doi.org/10.1029/2018GC007506

1860   Zhao, X., Zhang, Z., Huang, S., Liu, Y., Li, X., Zhang, H., 2017. Coupled extremely light Ca and Fe
1861   isotopes in peridotites. Geochim. Cosmochim. Acta 208, 368–380.
1862   https://doi.org/10.1016/j.gca.2017.03.024

1863   Zhao, Y., Simon, J.I., 2019. Calcium isotope determination with the Nu Sapphire Dual-Path MC-ICP-MS.
1864   Goldschmidt 2019 2019.

1865   Zhu, H., Du, L., Li, X., Zhang, Z., Sun, W., 2020. Calcium isotopic fractionation during plate subduction:
1866   Constraints from back-arc basin basalts. Geochim. Cosmochim. Acta 270, 379–393.
1867   https://doi.org/10.1016/j.gca.2019.12.004

1868   Zhu, H., Liu, F., Li, X., Wang, G., Zhang, Z., Sun, W., 2018. Calcium Isotopic Compositions of Normal
1869   Mid-Ocean Ridge Basalts From the Southern Juan de Fuca Ridge. J. Geophys. Res. Solid Earth 123,
1870   1303–1313. https://doi.org/10.1002/2017JB014699

1871   Zhu, P., Macdougall, D.J., 1998. Calcium isotopes in the marine environment and the oceanic calcium
1872   cycle. Geochim. Cosmochim. Acta 62, 1691–1698. https://doi.org/10.1016/S0016-7037(98)00110-0

1873